Inter- and intraconfigurational luminescence of $LiYF_4:Er^{3+}$ under selective VUV excitation

DISSERTATION

zur Erlangung des Doktorgrades

des Fachbereichs Physik

der Universität Hamburg

vorgelegt von

Evgueni Negodine

aus Sverdlovsk

Hamburg

2003

Gutachter der Dissertation:	Prof. Dr. G. Zimmerer
	Prof. Dr. G. Huber
Gutachter der Disputation:	Prof. Dr. G. Zimmerer
	Prof. Dr. D. Heitmann
Datum der Disputation:	08.07.2003
Vorsitzender des Prüfungsausschusses:	Dr. K. Petermann
Dekan des Fachbereichs Physik und Vorsitzender des Promotionsausschusses:	Prof. Dr. F.W. Büßer

Kurzfassung

Eine systematische spektroskopische Charakterisierung von Er^{3+}-dotiertem $LiYF_4$ wurde mittels energie- und zeitaufgelöster Lumineszenzspektroskopie durchgeführt, mit dem Ziel, die elektronische Relaxation in diesem System zu analysieren. Die Untersuchungen konzentrieren sich auf diejenigen Energietransferprozesse innerhalb der Er^{3+}-Ionen, die zu optischen Übergängen führen. Der Einfluss verschiedener Parameter wie Temperatur, Dotierungskonzentration und Ausgangszustand der Anregung wurde berücksichtigt, um möglichst vollständige Informationen über die elektronische Relaxation zu erhalten.

Die Lumineszenz von $LiYF_4:Er^{3+}$ wurde in einem weiten Spektralbereich von 150 nm bis hin zu 1100 nm untersucht. Die VUV-Emissionen haben ihren Ursprung in interkonfiguralen $4f^{11}5d$-$4f^{11}$-Übergängen in Er^{3+}. Die erstmalig durchgeführten zeitaufgelösten Lumineszenzmessungen ermöglichen die Unterscheidung und Zuordnung einer Reihe von *d-f* –Übergängen. Relaxationen innerhalb der *f*-Niveaus wurden ebenfalls betrachtet. Anregungsspektren der intensivsten Emissionsbänder wurden aufgenommen und ausgewertet.

Die Er^{3+}-Dotierungskonzentration wurde zwischen 1 % und 30 % variiert. Die qualitativen Änderungen in der Lumineszenz in Abhängigkeit von der Er^{3+}-Konzentration wurde untersucht und eine Analyse der Konzentrationsabhängigkeit der Er^{3+}-*5d-4f*-Emission durchgeführt. Zusätzlich wurden die Abklingcharakteristiken der Spin-erlaubten und der Spin-verbotenen Lumineszenz in Abhängigkeit von der Dotierungskonzentration gemessen. Die Kombination dieser zwei unabhängigen Datensätze (d. h. Lumineszenzintensität und Abklingkurven) ermöglicht die Bestimmung einer Reihe von wichtigen Parametern, die die elektronische Relaxation im gegebenen System beschreiben.

Die beobachteten Änderungen der Lumineszenzeigenschaften innerhalb eines großen Temperaturbereichs zwischen 6 K und etwa 900 K unterstreichen den Einfluss der Temperatur auf die elektronische Relaxationsprozesse. Die zusätzliche Untersuchung von nominell reinem $LiYF_4$ gab Auskunft über die elektronischen Zustände des Wirtsgitters.

Desweiteren werden experimentelle Ergebnisse diskutiert, die die $LiYF_4:Er^{3+}$-Lumineszenz nach Innerschalenanregungen betreffen, mit dem Ziel, die Relaxationsprozesse in diesem System nach Anregungen mit Energien weit oberhalb der Bandlücke zu verfolgen.

Abstract

A systematic spectroscopic characterization of $LiYF_4$ doped with Er^{3+} with an attempt to analyse the electronic relaxation was performed using energy- and time-resolved luminescence spectroscopy. The examinations is focused on the energy transfer processes within the Er^{3+} ions leading to the optical transitions. The influence of the different parameters such as temperature, doping concentration and initial excited state was treated to provide complementary information concerning the electronic relaxation.

The luminescence of $LiYF_4$:Er^{3+} system was investigated in a wide spectral range from 150 nm up to 1100 nm. The VUV emission originates from the inter-configurational $4f^{10}5d$-$4f^{11}$ transitions of Er^{3+}. For the first time, careful time-resolved luminescence measurements allow to distinguish and assign a number of *d-f* transitions. The relaxations within the *f*-manifold were analysed as well. Excitation spectra of the most intense emission bands were recorded and compared.

The Er^{3+} doping concentration was varied from 1% to 30%. The qualitative alterations of the luminescence following changes of the Er^{3+} concentration were studied and an analysis of the concentration dependency of the Er^{3+} *5d–4f* emission has been performed. In addition, the decay kinetics of the spin-allowed and spin-forbidden luminescence as a functions of doping concentration were measured. The combination of these independently obtained data sets (*i.e.* luminescence intensity and decay kinetics measurements) yields a number of important parameters describing electronic relaxation in the given system.

The observed change in the luminescence properties over a wide temperature range from 6 to ~ 900 K highlight the role of the temperature in the electronic relaxation processes. The additional investigation of the nominally pure $LiYF_4$ gave information about the electronic states of the host matrix.

Some experimental results concerning $LiYF_4$:Er system under inner-shell excitation were discussed with an attempt to trace the relaxation processes in this system after excitation with energies much higher than the band-gap.

Contents

1 Introduction 1

2 Experiment 5

2.1 Beamline. 5

2.2 Monochromators at SUPERLUMI 7

2.2.1 Primary monochromator. 7

2.2.2 1/2-m Pouey monochromator 9

2.2.3 Czerny-Turner-type monochromator 9

2.3 Detectors and electronics at SUPERLUMI 10

2.3.1 Photomultipliers 10

2.3.2 Microsphere plate detector. 11

2.3.3 CCD detector 13

2.3.4 Experimental electronics 17

2.4 Experimental method 19

2.4.1 Data registration 20

2.4.2 Data processing 22

2.5 Samples 25

3 Theoretical overview

3.1 Host materials 27

3.2 Single rare-earth ion 30

3.2.1 Energy levels of free ions 31

3.2.2 Rare-earth ions in the crystal field 33

3.3 Intra-ionic relaxation processes 36

3.3.1 Radiative relaxation. 36

3.3.2 Non-radiative relaxation 38

3.3.3 Selection rules for radiative transitions 40

3.4 Interionic processes 42

3.4.1 Radiative interionic processes 42

3.4.2 Non-radiative interionic processes 42

3.5 Luminescence decay 45
3.6 Intraconfigurational $4f^n$ -$4f^n$ transitions 50
3.7 Interconfigurational $4f^n$ -$4f^{n-1}5d$ transitions. 51
3.8 Interconfigurational charge transfer transitions 53

4 Experimental results and discussion

4.1 Luminescence of Er^{3+} in $LiYF_4$ crystal 55
4.1.1 *d-f* luminescence 57
4.1.1.1 Soft X-ray excitation 63
4.1.1.2 High temperature experiments 65
4.1.2 Visible and infrared luminescence 69
4.2 Excitation spectra 71
4.2.1 Excitation of the *d-f* luminescence via host absorption 74
4.2.2 Excitation of *f-f* luminescence, intrinsic and extrinsic host emission 76
4.2.2.1 Investigation of the undoped $LiYF_4$ system 77
4.2.2.2 Charge transfer excitation and autoionization processes. 79
4.2.3 Soft X-ray excitation 81
4.3 Branching of absorbed energy 83
4.3.1 Initial excited state 83
4.3.2 Doping concentration 83
4.3.3 Temperature 94
4.4 Decay analysis 97
4.4.1 Simple model 97
4.4.2 Inokuti-Hirayama model 98
4.4.3 Introduction of the donor-donor transfer 101
4.4.4 Discussion 107
4.4.5 Cross-relaxation 113
4.5 The model of electronic relaxation in $LiYF_4$:Er^{3+} 117
4.5.1 Excitation of the lowest HS- and LS-states. 117

4.5.2 Higher excitation energies within the transparency range of the host 123
4.5.3 Host excitation below threshold of inelastic electron scattering 124
4.5.4 Host excitation at higher photon energies. 125

5 Summary 127

Appendixes

A Software used at the experiment 131

B BW3 experiment 125

C Energy levels of the Er^{3+} in $LiYF_4$ 139

List of figures 145

List of Tables 151

Bibliography. 153

Chapter 1

Introduction

Luminescent materials are applied in our days in many important devices. In some of the applications the search on the phosphors has yielded materials with excellent properties, which cannot be improved further for fundamental reasons. In other applications this situation has not yet been attained. The question arises whether further improvement is possible or not. Thus there are situations in which phosphor research is directed towards new materials, which are preferred, for example, because of the cost reduction or environmental arguments. New technologies are now emerging where rare earth activators are applied in the UV and VUV excitation energy range concerning lighting with the development of new Hg-free fluorescent lamps and color plasma display panels, where VUV light from a Penning mixture of xenon and neon excites phosphors deposited on special glass screens. As far as the medical imaging is concerned, there is still a strong request for the development of new inorganic scintillators, which should meet the basic requirements of high light emission yield and fast response. The search for such new promising phosphors for excitation by UV and VUV radiation will certainly progress with a better quantitative understanding of the luminescence excitation mechanisms. With full knowledge of the processes occurring in rare earth activated inorganic hosts within the special energy excitation range considered, the behavior of new luminescent materials can be predicted and optimized for applications.

The broad range of applications requires (i) search and synthesis of new combinations of wide band-gap hosts with optically active ions, (ii) spectroscopic

characterization, and (iii) an analysis of the electronic relaxation including host-guest energy transfer and inter- as well as intraionic electronic relaxation within the $4f^{n-1}4f^*$ and the $4f^{n-1}5d$ manifold of rare earth (RE) ions. The first experiments with the main emphasis on the role of d-levels dates back to the seventies. In the pioneering papers by Elias et al. [Eli73], and Heaps et al. [Hea76], VUV excitation spectra of visible *f-f* emission, covering typical *4f-5d* excitations of RE^{3+}-ions in a LnF_3 host, were already established. The *d-f* luminescence of RE-ions in the ultraviolet spectral range is under investigation since a long time. A systematic collection and analysis of data was recently published by Dorenbos [Dor^{1}00, Dor^{2}00, Dor^{3}00]. The investigation of *d-f* emissions of rare earth ions in the VUV spectral range also started long ago [Yan76]. But only since a few years, the VUV *d-f* emissions really attract attention. Only a few groups went into this field because of the difficulties involved in VUV luminescence spectroscopy. Measurements on the weak (parity forbidden) intraconfigurational $4f^n$–$4f^n$ transitions require special setups for luminescence spectroscopy in the VUV, and calculations including levels above 50000 cm^{-1} require larger matrices. Most results up to now have been obtained with synchrotron radiation as an excitation source.

The aim of the present work is a systematic spectroscopic characterization of a simple model system with an attempt to analyse the electronic relaxation. As a model system, $LiYF_4$ doped with Er^{3+} was chosen, in spite of the fact that already a certain number of investigations on this system have been performed [Weg98, Bec98, Mak00, Pie01]. The reasons are, (i) this system emits all kind of emissions (spin-allowed and spin-forbidden *d-f* bands, various *f-f* lines), (ii) there exists only one type of center, and (iii) no charge compensation is necessary.

The complete analysis of electronic relaxation of Er^{3+} doped in the host matrice includes

- time-resolved and time-integrated luminescence spectroscopy from the VUV to the IR spectral range following selective excitation with VUV radiation;
- time-resolved luminescence excitation spectroscopy;
- analysis of decay curves of spectrally selected luminescence lines following primary selective excitation.

In the first experiments of this work on $LiYF_4$:Er^{3+}, the main emphasis was put on time-resolved *d-f* luminescence measurements. This allowed to identify fast and slow components, which, however, were incorrectly assigned until Wegh *et al.*

[Weg98] ascribed them to spin-allowed and spin-forbidden transitions. In the meantime, additionally to the VUV emission bands, the *f-f* lines following selective VUV and *f-f* excitation were investigated as well.

Different parameters, such as doping concentration, temperature and initial excited state, were varied to study how their influence on the energy relaxation in the given system.

Decay kinetic analysis of the spin-allowed *d-f* luminescence was performed quantitatively, giving additional information about energy transfer processes following VUV excitation.

The present work is divided into the following chapters. Chapter 2 contains information about the experimental set-up. The optical and electronic components as well as the applied spectroscopic methods are described. Before the experimental data will be presented and discussed, it is necessary to present some fundamentals for an understanding of the processes which take place in fluoride crystals doped with Er ions. In Chapter 3, a general description of the investigated crystal host, the energy level scheme of Er^{3+} ions in this host, and the intraionic and interionic physical processes responsible for the population dynamic of the Er^{3+} energy levels are presented. Along with relaxation mechanisms within a single ion, various theoretical models describing energy transfer processes are considered. The model of electronic relaxation in $LiYF_4:Er^{3+}$ based on results of time-resolved luminescence spectroscopy is proposed and discussed in Chapter 4. The main conclusions are resumed in the summary.

Some additional information about software created in the frame of this work and description of additional experimental set-up, where part of data was obtained, is given in the Appendices.

Chapter 2

Experiment

The main part of the experimental work was carried out at the SUPERLUMI experimental station, which is located in HASYLAB (*Hamburger Synchrotronstrahlungslabor*) at DESY (*Deutsche Elektronen-Synchrotron*). This station provides excellent opportunities for time- and energy-resolved vacuum ultraviolet (VUV) luminescence spectroscopy. Photons with an energy from 3.7 to 40 eV can be used for the excitation. Three different secondary monochromators are available for the analysis of the emission, giving in combination with different detectors the possibility to analyse luminescence from 1.2 eV to 25 eV. Simultaneously with excitation spectra, reflectivity curves from the sample at the angle of incidence 17.5° can be recorded. The experimental chamber, as well as the light path from the source to it, *i.e*. the beamline, is evacuated to UHV conditions to avoid absorption losses in the VUV spectral region. The SUPERLUMI set-up offers also the possibility to work at a wide temperature range starting from helium temperatures (a flow type helium cryostat) up to 1000 K (high temperature sample holder). For rare gas solids experiments, SUPERLUMI is provided with a gas inlet system and *in situ* crystal growing system.

2.1 Beamline

The SUPERLUMI set-up is located above the DORIS III storage ring plane at the beamline I. The circumference of the storage ring is 289.2 m. Normally DORIS is

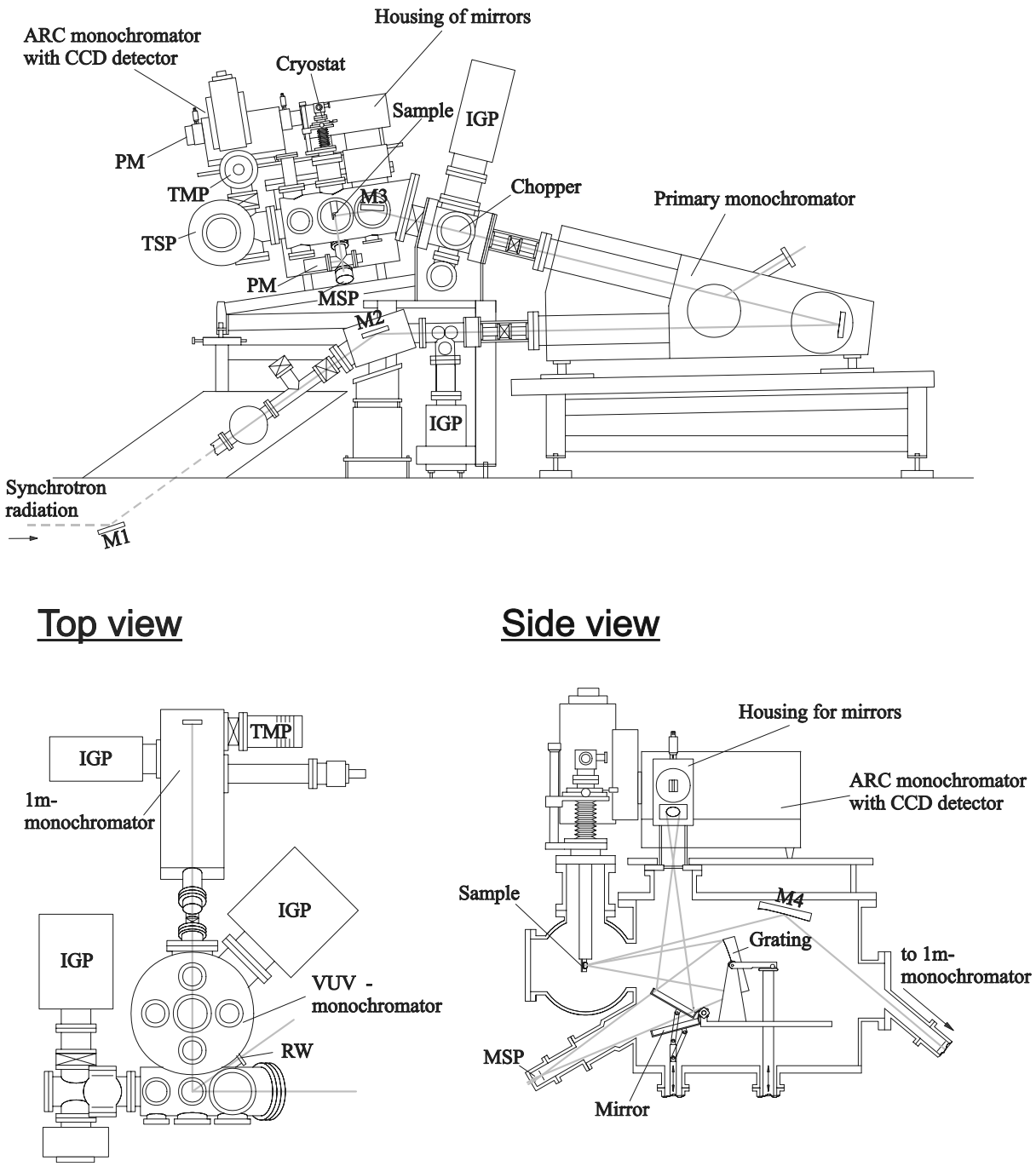

Figure 2.1: *SUPERLUMI set-up. TMP – turbomolecular pump; TSP – titanium sublimation pump; MSP- Microsphere plate detector; PM – photomultiplier; IGP – ion getter pump; RW – reflection window; M1, M2, M3 – mirrors; VUV – high flux secondary monochromator; ARC - secondary Czerny-Turner-type monochromator.*

filled with 5 bunches, each of them having a FWHM of 130 ps. The interval between the first and the fifth bunch is 196 ns and between all others is 192 ns. In the single bunch mode, which also takes place, the period of excitation pulses is conformably 964 ns.

To illuminate the entrance slit of the primary monochromator, two mirrors are used. The first cylindrical water-cooled mirror (M1, located in the plane of the storage ring) accepts 50 mrad of the horizontal and 2.2 mrad of the vertical divergence of the source. Mirror M1 focuses light horizontally to a 10 mm wide image at the entrance slit of the primary monochromator. The second, plane elliptic, mirror (M2, located 3.7 m above the storage ring plane, on the level of the entrance slit) focuses vertically to 0.1 mm at the entrance slit of the primary monochromator. Mirrors M1 and M2 transform the 6x2 mm^2 light source into the 10x0.1 mm^2 light spot on the entrance slit of the primary monochromator. The light is dispersed by the primary monochromator in the vertical direction. A third, rotational-elliptic, mirror (M3, located in the sample chamber) focuses the light onto the sample. Finally, the size of the light spot on the sample is 4x0.15 mm^2.

2.2 Monochromators at SUPERLUMI

The SUPERLUMI set-up is equipped with four monochromators: the primary one, dispersing synchrotron radiation, and three for analysis of luminescence. A description and comparison of the properties of monochromators used in this work will be given in the following sections.

2.2.1 Primary monochromator

The primary monochromator is a 2 m unit in 15^o McPherson mounting with linear dispersion 4 Å/mm (grating 1200 grooves per mm) [Wil83]. The fixed entrance slits have widths of 30 μm, 100 μm and 500 μm which corresponds to the best achievable resolution (FWHM) of 0.2 Å, 0.5 Å and 2.3 Å. The exit slit is continuously adjustable between 10 μm and 2 mm. All necessary alignments can be done from outside the vacuum with the evacuated instrument in the beam. The smallest available

resolution of the primary monochromator is not determined by the slits of the monochromator, but by the size of chopper slits, located after the exit slit and having a width of 925 µm.

Two different prealigned gratings are mounted on the grating holder and can be interchanged *in situ*. The MgF_2 coated aluminum grating has a working range 65 nm to 330 nm and the platinum grating has a working range 30 nm to 330 nm. For maximal intensity it is reasonable to use the aluminum grating for wavelengths longer than 80 nm and the platinum grating for shorter wavelengths. In order to avoid higher orders in excitation it is possible to use LiF and quartz filters.

Recent direct photon flux measurements, which have been done with a photodiode AXUV-100, are shown in Figure 2.2. After the diode current was measured and corrected for the typical diode's quantum efficiency, the amount of the incoming photons can be determined. The number of exciting photons as a function of photon energy is depicted for the platinum grating and for the aluminum grating with quartz and LiF filters.

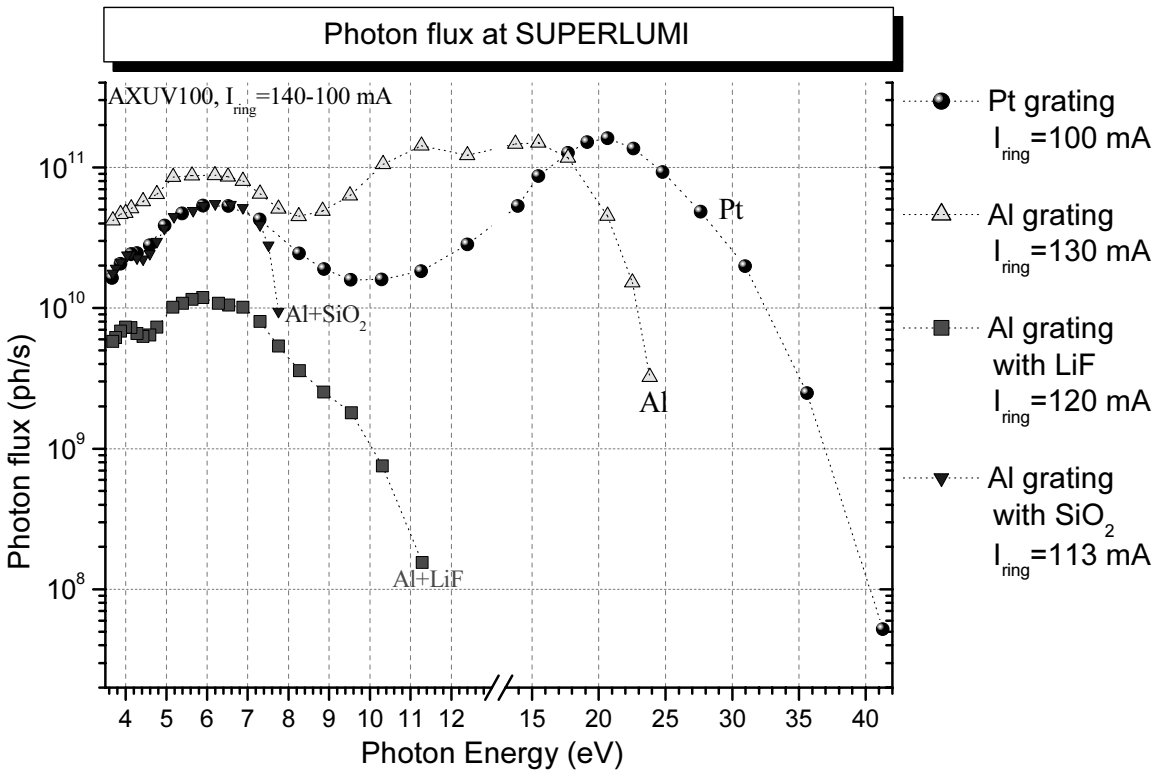

Figure 2.2: *The incident photon flux on the sample for different grating-filter combinations at the SUPERLUMI set-up measured in February, 2002.*

With the time the spectral properties of the gratings of the primary monochromator degrade. Under intensive synchrotron radiation, different photochemical reactions take place and therefore molecules and atoms of the residual gas are chemically active. Mainly carbon compounds that are deposited onto the grating surface, are responsible for the degradation of reflectivity. Radiation damage of MgF_2 coating of the aluminum grating and of filters (especially of those, that are illuminated with hard radiation, i.e. before primary monochromator) also takes place.

2.2.2 ½-m Pouey monochromator

The 1/2-m Pouey monochromator has its own vacuum chamber separated from the sample chamber with an UHV valve. The exit arm of the monochromator is equipped with two detectors. An open microsphere plate (MSP) or a solar-blind photomultiplier can be chosen via a removable mirror.

The VUV-monochromator is a high-flux instrument (modified Pouey mounting) without entrance slit. It is designed with different arm lengths: the exit arm (652 mm) is longer than the entrance arm (391 mm). A small f-number is achieved by a specially designed 130x130 mm^2 large toroidal grating with a non-uniform groove distribution (mean value n=1650 l/mm). The highest spectral resolution is limited mainly by the size of the exciting light spot on the sample. The working range of the Pouey monochromator is 500 to 3000 Å. The best achieved resolution with an optimized spot size is 0.5 nm (FWHM) [Gue83].

2.2.3 Czerny-Turner-type monochromator

For the detection of the ultraviolet, visible and infrared luminescence the SUPERLUMI set-up is equipped also with a 30 cm monochromator-spectrograph in Czerny-Turner mounting with aspheric mirrors ARC SpectraPro-308.

The monochromator has two exit ports, one of them serving a conventionlimial photomultiplier, the other one a LN_2-cooled two-dimensional CCD-camera. *In-situ*, three gratings can be interchanged (300 l/mm, 600 l/mm, 1200 l/mm). SpectraPro-308 includes an imaging optical system, a 32-bit microprocessor controlled scanning, built-in RS232 interface and a motorized mirror for computer controlled exit port selection. The working range of the monochromator extends from 185 nm to 1150 nm and is

limited by the available gratings and detectors. The best achievable resolution (1200 l/mm grating) is 0.16 nm.

Monochromator	Primary	VUV	SpectraPro-308
Mounting	Mc Pherson 15°	Pouey 28°	Czerny-Turner
Aperture	f:20	f:2.8	f:4
Focal length (mm)	2000	500	300
Grating size* (mm)	Ø100	130×130	68×84
Grooves (l/mm)	1200	1650**	300/600/1200
Linear dispersion (nm/mm)	0.4	1	2.7***
Coating	Al+MgF_2 / Pt	Al+MgF_2	Al+UV coating
Working range (nm)	65 - 330 30 - 330	50 - 300	185 - 1400
Blaze (nm)	100 (Al)/ Pt†	250	300

Table 2.1: *Technical data of the monochromators at SUPERLUMI.*
Horizontal×vertical or diameter. ** Mean value. * Specifications for 1200-gr/mm grating. †Platinum grating is laminar type.*

2.3 Detectors and electronics at SUPERLUMI

In the following chapter a description of the photon detectors, which are in operation at the SUPERLUMI set-up, will be given.

2.3.1 Photomultipliers

For the VUV range, a so-called *solar blind* photomultiplier (*Hamamatsu R6836*) was used. The working range of this detector covers 115-320 nm range. The short wavelength edge of sensitivity is restricted by transmission of the MgF_2 window of the photomultiplier. Unfortunately, the *solar blind* has a relatively bad time-

resolution. The advantage of this detector is in the quite convenient working range covering the VUV and UV region.

For the measurements in the UV-visible range, a *Hamamatsu R6358P* photomultiplier was used. This is a side-on photomultiplier tube for photon counting with a small rectangular photocathode of 13x4 mm. Therefore, the dark current is low and no cooling is needed.

In case of reflectivity measurements (*Valvo XP2230B*), VUV light reflected from the sample is converted into fast broadband emission peaking at 420 nm using a thin semitransparent sodium salicylate layer. Because the light intensity is always measured at the same wavelength, the spectral characteristics of the photomultiplier are not especially important. In order to decrease the dark current, the detector is cooled with Peltier elements. The technical data for the photomultiplier are shown in Table 2.2.

Producer Type	***Hamamatsu R6836***	***Hamamatsu R6358P***	***Valvo XP2230B***
Working range (nm)	115-320	185-830	250-650
Photocathode	Ce-Te	LMA*	SbKCs
Window	MgF_2	UV glass	borosilicate
Amplifier gain (at voltage)	1×10^6 (-1.5 kV)	3.5×10^6 (-840 V)	3×10^7 (-2.2 kV)
Rise time (ns)	4	1.4	0.7
Dark pulses (cps)	3-5 (not cooled)	20 (not cooled)	50 (-15 °C)
Max. quantum efficiency (%)	15	23	48
At wavelength (nm)	240	530	400
Typical voltage (V)	-1500	-840	-2200

Table 2.2: *Technical data of conventional photomultipliers at the SUPERLUMI set-up. *LMA – Low dark current multialkali*

2.3.2 Microsphere plate detector

A MicroSphere Plate (MSP) attached to the VUV monochromator was used for decay measurements and time resolved excitation spectra in the vacuum ultraviolet spectral region [Koe97]. The MSP is a compact electron multiplier. It consists of 50 µm glass beads sintered to form a thin porous plate. Incoming photons hit the MSP producing electrons. These electrons are accelerated by the electric field through the porous plate and collide with the beads' walls. In each collision more secondary electrons are generated. Finally, a large number of electrons emerge from the output side of the MSP. Secondary electrons generated at the front surface are directed by the electric field into the MSP. Due to this "funneling effect", nearly the entire MSP front surface is active.

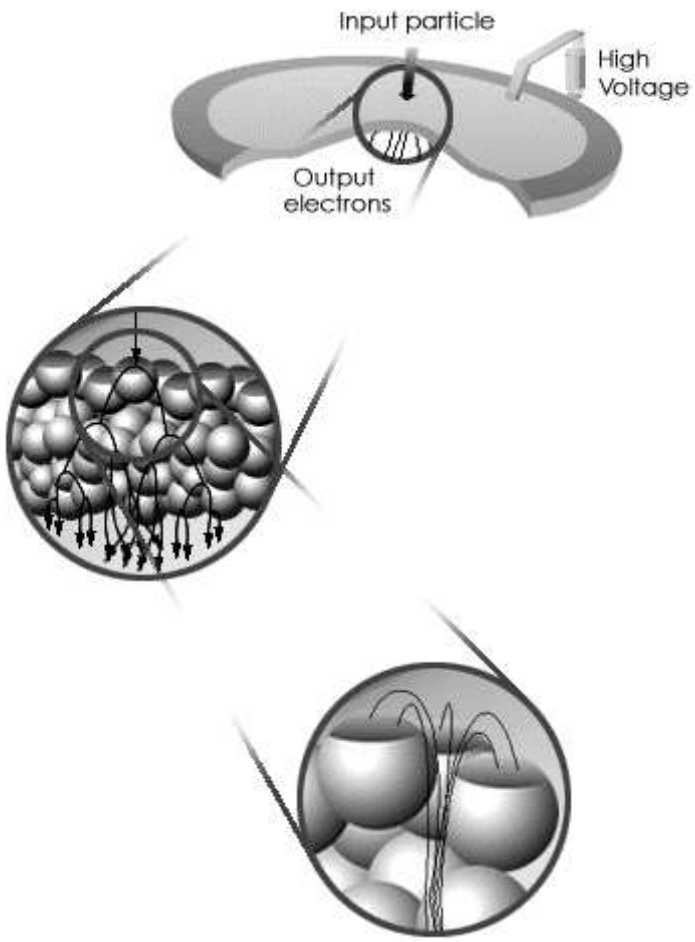

Figure 2.3: *Schematic representation of the function of the MSP*

In contrast to microchannel plates, which operate in the same way, the MSP has irregular channels. Due to this fact the acceleration of the residual gas ions in a MSP is strongly suppressed. To increase the sensitivity of the detector in the long wavelength range, the cathode of the MSP is coated with a 1 µm thick CsI layer.

A high voltage up to 3.5 kV can be applied to the MSP used at the SUPER-LUMI set-up. But the maximum value will decrease the time resolution and also

cause a decrease of the lifetime of the detector. Because of this reason most of the experiments were performed with an intermediate voltage value of 3.2 kV.

Producer Type	El Mul E033DTA1F
Working range (nm)	≤180
Diameter (mm)	32.8
Cathode effective diameter (mm)	27.0
Thickness (mm)	1.41
Cathode coating	CsI (1μm)
Amplifier gain (at voltage)	$5*10^6$ (-3.5 kV)
Integral dark pulse rate (cps)	5…10
Max. operating pressure (Torr)	10^{-5}…10^{-4}
Operating voltage (kV)	-3.0…-3.5

Table 2.3: *Technical data of the microsphere plate (MSP).*

2.3.3 CCD detector

CCDs (Charge Coupled Devices) for scientific applications with a large dynamic range and high sensitivity exist since the end of the 80s. They have found wide use in spectroscopy and for imaging application.

The basic device consists of a closely spaced array of MOS (metal-oxide-silicon) diodes on a continuous insulator (oxide) layer that covers a semiconductor substrate [Sze81].

The fundamental process that occurs in CCD imaging is the conversion of photonic input to the electronic output. Atoms in a silicon crystal have electrons arranged in discrete energy bands. Most of the electrons occupy the valence band but can be excited into the conduction band by heating or by the absorption of a photon. Once in this conduction band, the electron is free to move about in the lattice of the

silicon crystal. It leaves behind a 'hole' in the valence band. In the absence of an external electric field the hole and electron will quickly recombine and be lost. In a CCD an electric field is introduced to sweep these charge carriers apart and prevent recombination. Thermally generated electrons are indistinguishable from photo-generated electrons. They constitute a noise source known as '*Dark Current'* and it is important that CCDs are kept cold to reduce the number of thermal electrons.

After photons incident on the CCD are converted to electron-hole pairs, the electrons will be captured under the gate electrodes of the CCD (Fig. 2.4a). These electrons are then transferred in a "bucket brigade" (Fig. 2.4b) fashion to the output amplifier where the charge is converted to a voltage output signal. An analog processing chain further amplifies this signal and finally it is digitized before being transferred to a host computer for display, image processing, and/or storage. The transfer function between the incident photonic signal and the final digitized output should vary linearly with the amount of the incident light on the CCD.

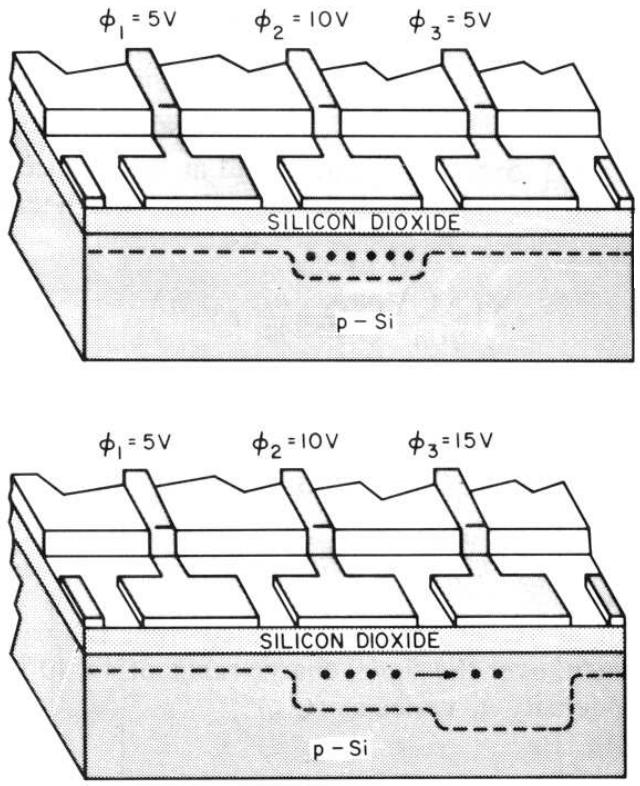

Figure 2.4: *Cross section of charge-coupled device. (a) Higher voltage on Φ_2. (b) Φ_3 is pulsed for higher voltage for charge transfer [Sze81].*

Among the most important measurable characteristics associated with charge-coupled devices (CCDs) is quantum efficiency. Quantum efficiency (QE), often expressed as a percentage, indicates the effectiveness of an imaging to produce electronic charge from incident photons. The greater the QE at a given wavelength, the more efficient the imager at that wavelength.

The majority of commercially available CCDs are frontside-illuminated devices made from silicon. In a frontside-illuminated CCD, light passes through the polysilicon gates that define a charge well at each pixel (see Figure 2.5). While the gates transmit a number of the incident photons to the CCDs photoconversion layer, they will also reflect and absorb a fraction of photons, thereby preventing some light from reaching the pixel's photosensitive region. For gates made from the polysilicon, the transmission starts to drop at wavelengths shorter than 540 nm and is essentially zero below 400 nm. Therefore, frontside-illuminated sensors have a particularly low QE in the blue/green region of the spectrum.

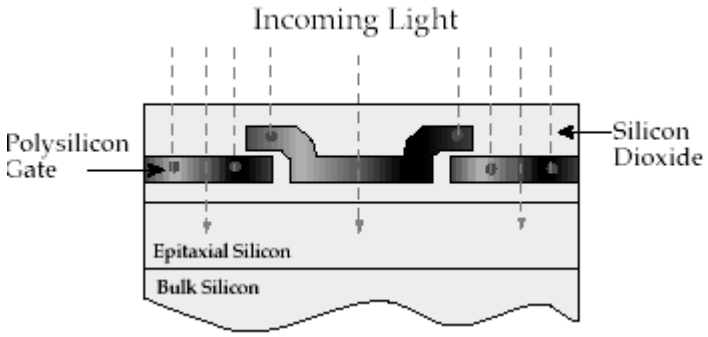

Figure 2.5: *Light passes through the polysilicon gates of a standard frontside-illuminated CCD in order to reach the device's photoconversion layer.*

Another approach to solve the blue/green sensitivity issue is to use a thinned, backside-illuminated CCD instead of a frontside-illuminated device (see Figure 2.6). Employing acid-etching techniques, it is possible to uniformly thin a CCD to a thickness of approximately 10 µm and focus an image on the backside of the CCD register, where there is no gate structure. These CCDs have more than twice the quantum efficiency (light-detection ability) of their front-illuminated counterparts.

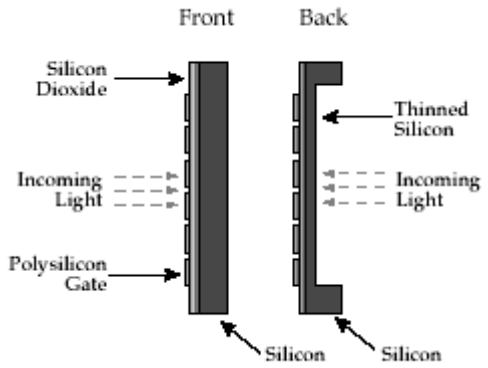

Figure 2.6: *Comparison of front-illuminated and back-illuminated CCD.*

To achieve UV response (190 to 400 nm), the CCD surface must be coated with a very thin layer of converter, which absorbs UV radiation and re-emits at wavelength in the visible region.

Most of the CCD cameras are cooled for optimal performance. Cooled operation results in CCD read noise that is 2-5 times lower. The CCD dark current decreases by cooling up to eight orders of magnitude compared to room temperature operation. Two methods of cooling are available: thermoelectric (Peltier device) or liquid nitrogen cooling (Fig 2.7). Because of the low operating temperatures, these cameras should only be operated under vacuum.

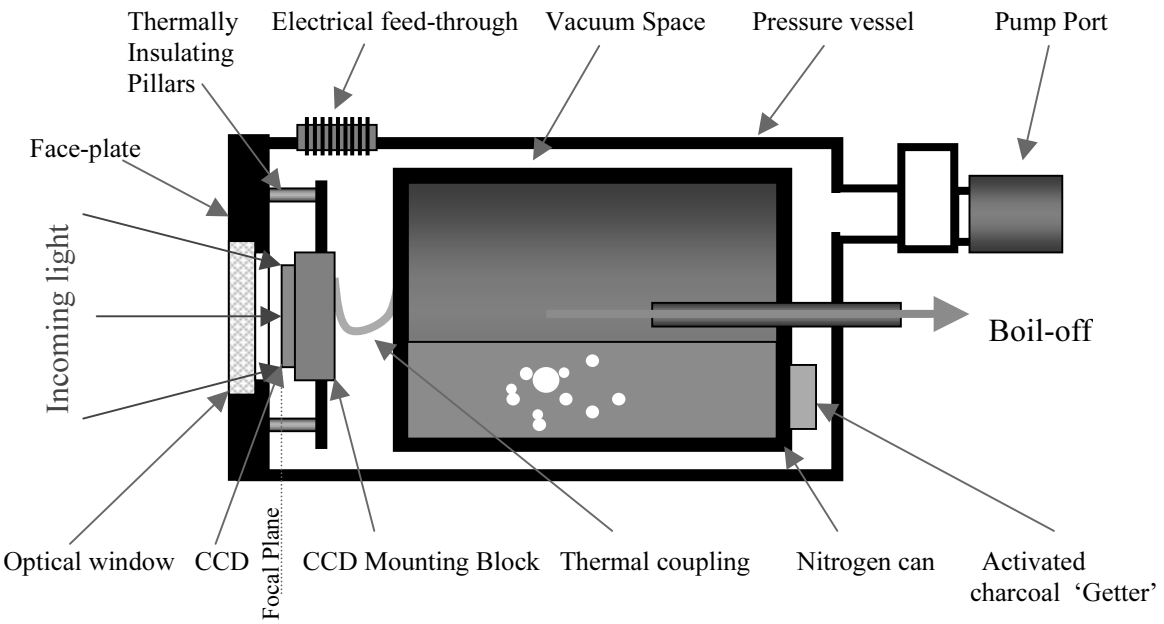

Figure 2.7: *CCD mounting diagram. The CCD is mounted onto a copper cold block that is distanced from the removable end plate by thermally insulating pillars. A flexible copper braid connects this block to the LN_2 can. The thickness of the braid is adjusted so that the equilibrium temperature of the CCD is about 10 degrees below the optimum operating temperature. The mounting block also contains a heater resistor and Platinum resistance sensors that are used to regulate the CCD temperature. To prevent condensation it is necessary to blow dry air across the outside. On the back of the LN_2 can is a small container filled with activated charcoal known as a 'Getter'. This acts as a sponge for any residual gases in the camera vacuum.*

Most of the experiments in the UV-visible region presented in this thesis were carried out with a Princeton Instruments LN/CCD detector system which includes a cryogenically cooled camera head PI Scientific Grade 1 1100x300 pixel format, thinned back illuminated CCD 24x24 μm pixel, side-looking 1.5 liters liquid nitrogen dewar, large 40 mm focal shutter, controller ST-133, computer interface board, and software.

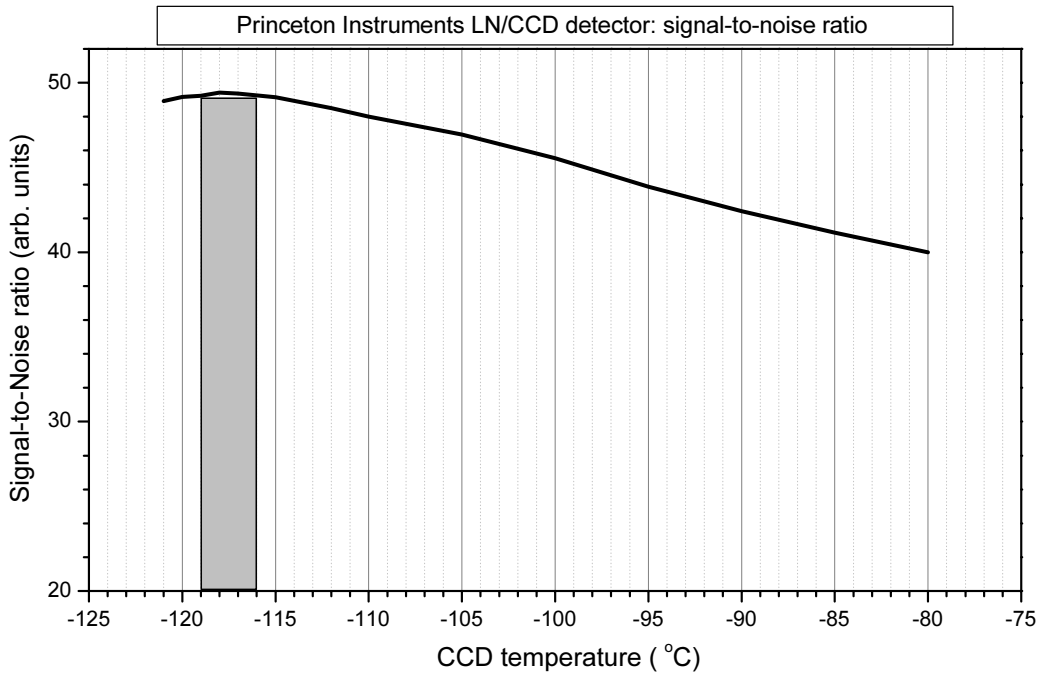

Figure 2.8: *Temperature dependence of the Signal-to-Noise ratio Princeton Instruments LN/CCD detector*

This CCD camera, in connection with the spectrometer SpectraPro-308, has been tested 'on the workbench' before being mounted at the SUPERLUMI set-up. Using a Hg calibration lamp, the best achievable resolution* and signal-to-noise (actually signal-to-background) ratio were measured. The optimal working temperature for the CCD was ascertained from the signal-to-noise ratio curve (see Fig 2.8) and lies in the range between –119 and –116 °C. Typical exposure time are 200-

* *In particular, the resolution of 0.1 nm was achieved under 'workbench' conditions. The best achievable resolution in situ at SUPERLUMI experiment is less (0.16 nm) due to the scarce light intensity restricted by the minimal slit size.*

400 s depending on the strength of luminescence originating from the particular sample.

2.3.4 Experimental electronics

In the following section, a short overview of the electronic devices at the SUPERLUMI set-up is given.

For the measurements of time-resolved spectra or decay kinetics, the data were collected using a single-photon-counting method [OCo84]. A single photon causes a signal pulse from the detector and afterwards each pulse is processed separately. Weak detector signals are amplified by a preamplifier and processed by a constant-fraction discriminator according to the widely used NIM (*Nuclear Instruments Method*) standard. Due to independency of timing of the output signal from the amplitude of the detector signal the constant-fraction principle offers good time-stability. An integrated preamplifier-constant-fraction discriminator *Ortec 9327* or fast preamplifier *Ortec VT120* together with a constant-fraction discriminator *Canberra 2126* are used at the SUPERLUMI set-up.

A time-to-amplitude converter (TAC) Canberra 2145 or 2146 was used in the time-resolved measurements. As inputs, the TAC requires start and stop signals (NIM). The TAC gives an output pulse with an amplitude (voltage in the range 0-10 V) proportional to the time interval between the start and posterior stop pulse. At the SUPERLUMI set-up the detector signal is used as a start pulse and a *raster* signal from the *bunch clock* of DORIS is used as stop signal. The *bunch clock allows* to trigger the chosen bunch with an accuracy of 300 ps [Ste00].

Time windows, which are necessary for the time-resolved measurements, can be realized with the aid of a single-channel analyzer (SCA). The TAC together with a multi-channel analyzer (*Canberra3501*) is used for the recording of decay curves as well. In the “pulse height” mode of the MCA the input pulses are sorted by their voltage amplitude (*i.e.* time) to a histogram. This histogram represents the frequency of occurrence for the emitted photons in the selected time interval.

The intensity of synchrotron radiation is not constant but decreases proportionally with time due to various loss processes. Therefore it is necessary to increase the counting time conformably for every experimental point. This is realized

in the following way. The DORIS control room provides every experiment with a voltage proportional to the storage ring current. Using a voltage-to-frequency converter this voltage is converted to pulses (~ 50 000 counts per second at 100 mA). The dual counter (*Canberra 1776*) integrates such pulses and gives a stop signal for any other device after a preselected number of reference pulses.

2.4 Experimental method

For the investigation of the electronic relaxation of selectively excited $LiYF_4:Er^{3+}$ crystals, different experimental methods were used:

- An **emission** or luminescence spectrum represents luminescence intensity as a function of the emitted photon energy. The excitation energy is fixed in these measurements. The curves obtained in this way give the information about radiative channels of relaxation in the crystal. It is also possible to measure time-resolved emission spectra.
- During the **excitation** spectrum measurements, the emitted photon energy is kept constant and corresponding curves display luminescence intensity as a function of exciting photon energy. No principal difference exists for luminescence emission and excitation measurements. Only the monochromator to be scanned is different. An excitation spectrum shows different population channels for a given luminescence band. To separate emissions with different lifetimes, time-resolution techniques can be used as well.
- A **reflectivity** spectrum displays the intensity of the light reflected from the crystal, depending on photon energy of excitation.
- A **decay** curve reflects the time dependence of radiative relaxation for a certain transition.

2.4.1 Data registration

Emission spectra

As was already mentioned, the Princeton Instruments LN/CCD detector system was used for collecting luminescence data. The system was controlled by an additional computer with WinSpec program operating under Microsoft Windows system. WinSpec is a high performance software package written specially for acquisition and analysis of images using Princeton Instruments cooled digital CCD cameras. Additional information about the software is given in Appendix A.

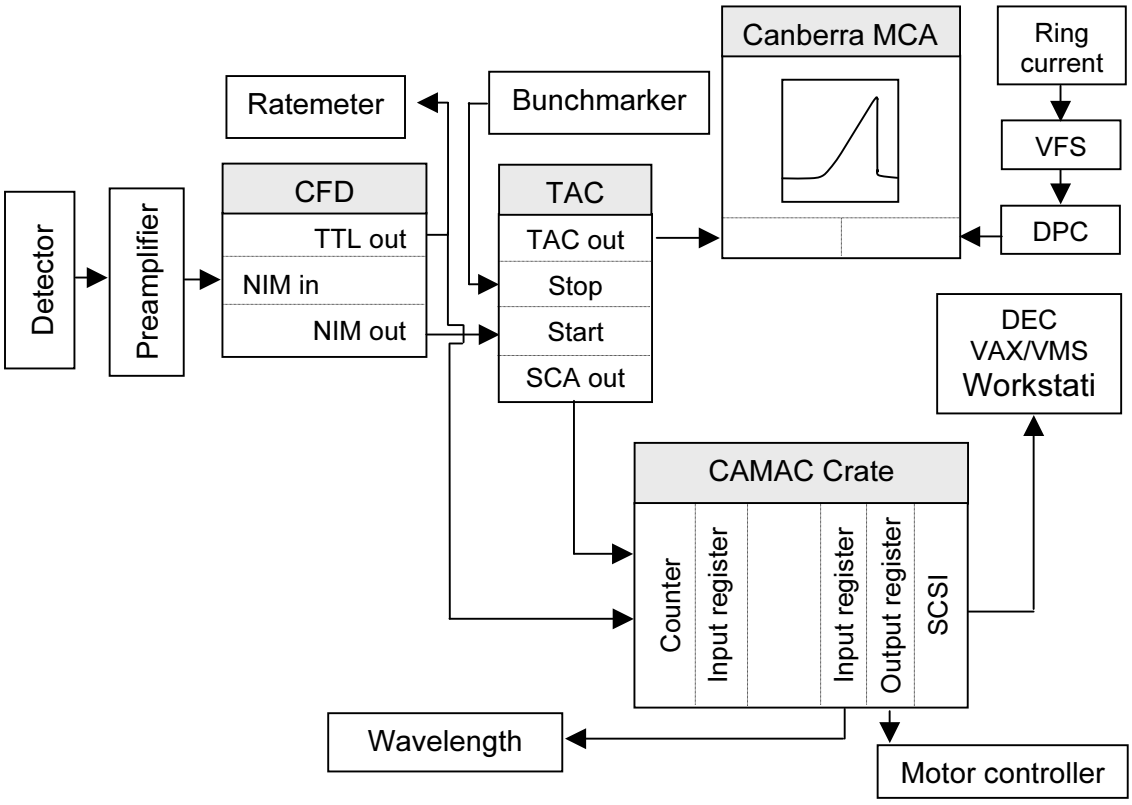

Figure 2.9: *Principal scheme for time-resolved luminescence and excitation measurements. The primary monochromator is scanned in case of excitation spectra measurements and the secondary one for emission spectra measurements. TAC: time-to-amplitude converter, CFD: constant fraction discriminator, VFS: voltage-to-frequency converter, DPC: dual preset counter, TTL: transistor-to-transistor logic, NIM: "nuclear instruments method", CAMAC: "computer automated measurements and control".*

Time-resolved emission spectra

Time-resolved emission spectra in the present work were measured with the VUV monochromator in combination with the MSP detector or solar blind photomultiplier, and with the ARC monochromator in combination with the side-on photomultiplier tube *Hamamatsu R6358P.*

The photon energy of excitation is selected for each measurement and the luminescence intensity is measured as a function of the emitted photon energy. Detailed information about the electronic devices shown in Figure 2.9 was given in section 2.3.4.

To take advantages of the computer control provided in SpectraPro-308, an additional program SpectraX was developed during my Ph.D. work for Windows PCs to allow the measurements of time resolved luminescence spectra. For the development of SpectraX the graphical programming language LabVIEW was used. More detailed information about SpectraX is given in Appendix A.

Excitation spectra

In case of excitation spectra, the photon energy of luminescence is kept constant and the intensity of the given luminescence is measured as a function of photon energy of excitation. Fig. 2.9 depicts the principal scheme for time-resolved excitation measurements.

Reflection spectra

In case of reflection measurements, the sodium salicylate luminescence, excited by the VUV light reflected from the sample is measured instead of direct reflection. The axes of the reflection channel and of the exciting beam are geometrically located under an angle of 35^{o}. The sample is adjusted in a way that the specular reflection from the sample surface is directed to the sodium salicylate coated window. “NaSal” is used here, like in case of grating spectra measurements (section 2.4.2.), due to constant quantum yield of its broad band emission (maximum at 420 nm) under UV-VUV excitation. The intensity of the luminescence is measured with a conventional UV-visible sensitive photomultiplier (see section 2.3.1). To select

emission of sodium salicylate, the filter (WG360) is also applied. Time-integrated as well as time-resolved reflection and excitation spectra can be recorded simultaneously at the SUPERLUMI set-up.

Decay curves

For the measurements of the decay curves, the TAC output is connected to the ADC input of the MCA, which operates in the "pulse height" mode. The MCA sorts every pulse to the respective time interval and forms a resulting histogram of the number of pulses per channel versus time, i.e. the decay curve. The time range for the time-resolved measurements is determined by the time interval between synchrotron bunches. It equals 192 ns when DORIS is operated in a five bunch mode or 480 ns in the case of two bunch mode. The maximum decay time range reached 964 ns in a single bunch mode. For the longer time range, SUPERLUMI offers additionally the unique possibility to work with a chopper, running under UHV condition [Run97].

2.4.2 Data processing

The light source and the transmission of the beamline and the primary monochromator cause the energy dependence of the excitation intensity. Therefore the excitation and reflection spectra have to be corrected to the incident photon flux. Therefore, it is necessary to measure the intensity as a function of the excitation energy using the luminescence of sodium salicylate. Typical spectra for the incident photon flux for the aluminium and platinum grating are shown in Figure 2.10. One can see that the platinum grating is well suited for wavelengths shorter ~80 nm and aluminium grating is better in the range starting from ~80 nm. A quartz and LiF filter are available to remove higher orders of excitation, inevitable satellites of diffraction gratings.

Due to the fact that the incident flux spectrum strongly depends on the optimisation of the mirrors of the beamline, the positions of the mirrors need to be adjusted in the beginning of each beam time period. In accordance with it, the incident flux spectrum was measured and the positions of the first mirrors were kept constant during experiments. Since the light source and the transmission of the beamline and

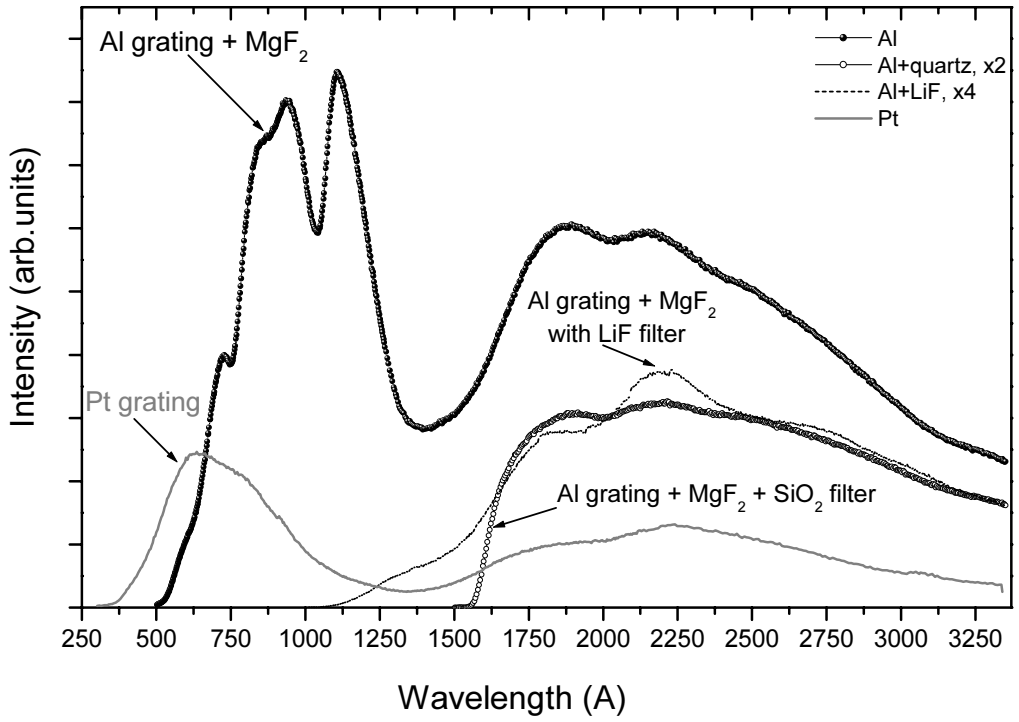

Figure 2.10: *The incident photon flux on the sample for different grating-filter combination at the SUPERLUMI set-up measured with Na-Sal.*

primary monochromator cause the energy dependence of the excitation intensity, it is necessary to correct the excitation and reflection spectra to the incident photon flux. All reflection and excitation spectra in this work are normalized.

Luminescence spectra are also influenced by the transmission function of the secondary monochromator and the detector sensitivity. Apparatus functions for the secondary monochromator ARC SpectraPro-308 in connection with a CCD detector or with a photomultiplier Hamamatsu R6358P were measured by Dr. M. Kirm using tungsten calibration lamp (black body radiation) and are shown in Figure 2.11. Transmission curves were recorded for two different gratings: 300/300* (curves 1 and 3) and 300/500 (curves 2 and 4). Due to the fact that in agreement with the well known Plank equation the spectral density of the black body radiation strongly decreases below 400 nm (see inset in Figure 2.10), transmission curves do not cover low wavelength part of the monochromator-detector system working range. The

* *means that the grating has 300 grooves per mm and the quantum efficiency is maximal at 300 nm.*

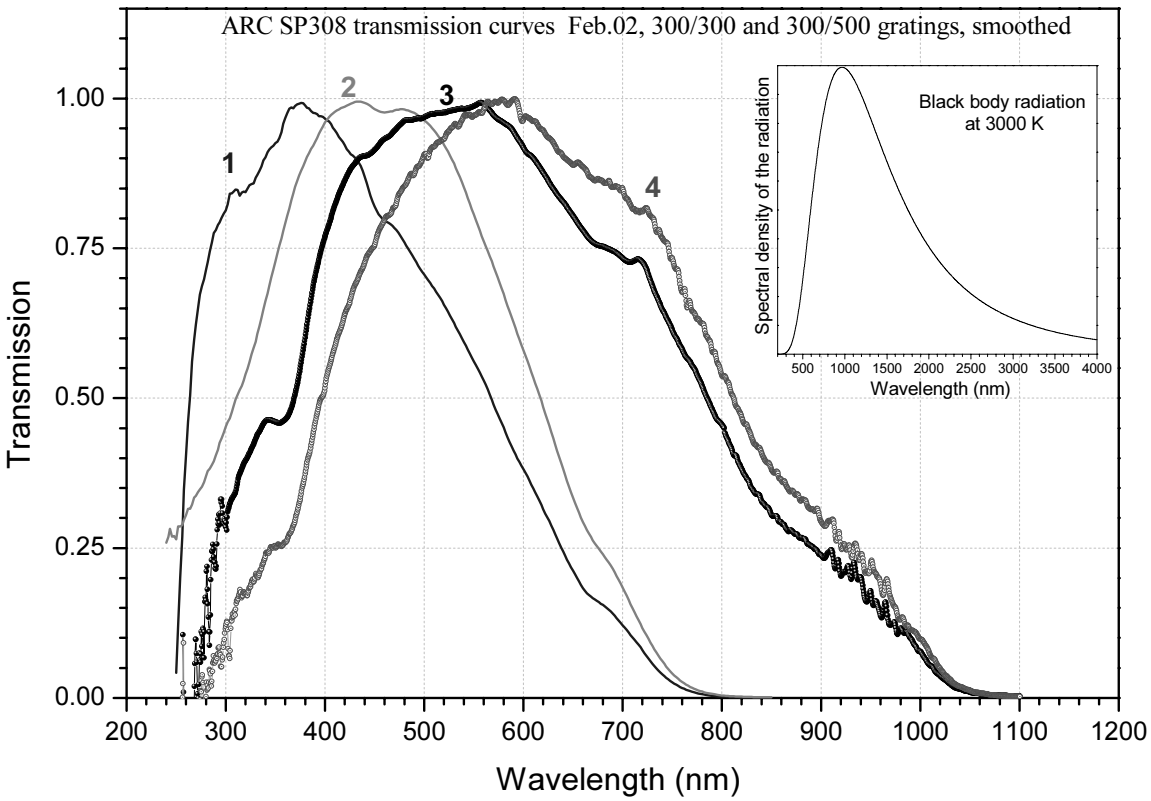

Figure 2.11: *Apparatus function for the secondary monochromator ARC SpectraPro-308 with different gratings in connection with a CCD detector or with a photomultiplier Hamamatsu R6358P measured by Dr. M. Kirm. Curve 1 – 300/300 grating plus PMT, curve 2 – 300/500 grating plus PMT, curve 3 – 300/300 grating plus CCD, and curve 4 – 300/500 grating plus CCD. Tungsten temperature was 3000 K. Upper inset mirrors spectral density of the black body radiation according to the Plank's equation.*

oscillations above 900 nm in curves 3 and 4 for CCD are connected with *etaloning effect*. Using a back-illuminated CCD in NIR region (700-1000 nm), the optical phenomenon, named *etaloning effect,* can appear, showing a random noise in data on the acquired spectrum. The cause of this phenomenon is interference induced by reflections of some wavelengths at the boundaries of the silicon layers. The result is oscillations superimposed on the CCD data with peak magnitudes and positions dependent on the layer thickness used in the production of the back illuminated chip. As this effect also depends on the direction of the incident optical beam, *etaloning* can be minimized by reducing the size of the image focused on to the detector or by

changing the central wavelength of acquisitions. However, this effect can not be totally suppressed.

In the present work some of the luminescence spectra are normalized (then it is mentioned apart) to reveal the relative intensities of the different emission bands. For the most part, nevertheless, it is not done because emission spectra do not cover a large range of photon energy and/or no quantitative conclusions are drawn for the relative intensities.

As all monochromators at SUPERLUMI set-up operate in wavelength units, an equality $E=hc/\lambda$ was used for transforming wavelength (λ) to the energy scale (E). Therefore, luminescence spectra, plotted in energy scale, are deformed because $\Delta\lambda=-(hc/E^2)\Delta E$ is not linear in energy.

2.5 Samples

All the samples investigated in this work are the single crystals and were grown by Czochralski technique. The Czochralski method, first applied by J. Czochralski in 1918 [Czo18] and initially used to pull metal and semiconductor single crystals is a well established procedure to grow single crystals from a congruent melt with a growth rate control. The crystals were grown in General Physics Institute of RAS in Moscow and in Institut für Laser-Physik Universität Hamburg. It also has to be mentioned that the crystals with doping concentration more than 1% contain admixture of Pr^{3+} resulting in intense emission bands in the UV and visible spectroscopic range.

The crystals were cleaved before being mounted on the sample holder and have random orientation.

Chapter 3

Theoretical overview

Before the experimental data will be presented and discussed, it is necessary to present some fundamentals for an understanding of the processes, which take place in fluoride crystals doped with Er ions. After a general description of the investigated crystal host and the energy level scheme of Er^{3+} ions in this host, the intraionic and interionic physical processes responsible for the population dynamic of the Er^{3+} energy levels are presented. Along with relaxation mechanisms within a single ion, various theoretical models describing energy transfer processes will be considered.

3.1 Host materials

There are different potential scintillator and solid-state laser materials suitable for rare-earth ion doping: glasses, fibres, semiconductors, and dielectric crystals. While rare-earth-doped semiconductors are in the early stage of investigation, crystals are advantageous over glasses and fibres because of the vast knowledge regarding the production and the properties of these materials gathered since the early 1960s. Crystals also benefit from their high thermal conductivity. Glasses and fibres are favourable if the size of the active material has to be large or if the dopant level has to be low [Ron95, Ron97, Ron98, Ron02].

The aim of the present work is a systematic spectroscopic characterisation of a simple model system with an attempt to analyse the electronic relaxation of the rare earth ion. As a model system, $LiYF_4$ crystal doped with Er^{3+} was chosen, due to the following reasons: (i) this system emits all kind of Er^{3+} emissions (spin-allowed and spin-forbidden $d \rightarrow f$ bands, various $f \rightarrow f$ lines), (ii) there exists only one type of center, and (iii) no charge compensation is necessary.

The uniaxial lithium yttrium fluoride crystal has the scheelite structure with a tetragonal lattice (space group $I4_1/a$). A tetragonal unit cell contains four stochiometric $LiYF_4$ units with eight cations and sixteen anions. The Er^{3+} ions substitute for the Y^{3+} ions that occupy the eightfold dodecahedrally coordinated lattice site. The Y^{3+} site has S_4 symmetry without inversion symmetry. The Li^+ ions occupy the fourfold tetrahedrally coordinated lattice site; the corresponding polyhedrons are distorted. A typical dopant level of 1% Er^{3+} in $LiYF_4$ is equivalent to a concentration of 1.38×10^{20} ions/cm^3. Figure 3.1 shows a schematic picture of the crystal structure. The crystal data and physical properties of $LiYF_4$ are summarised in Table 3.1.

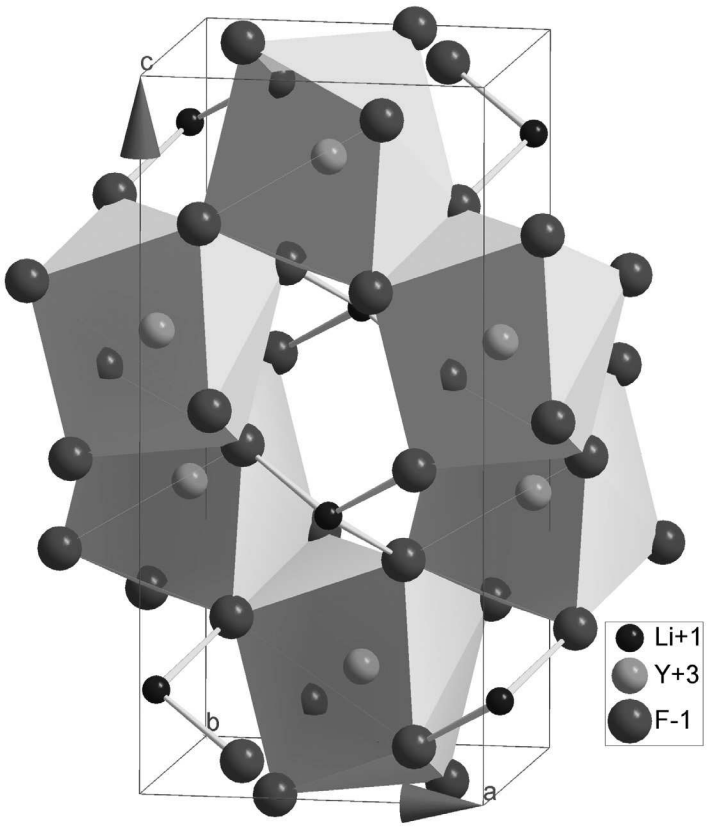

Figure 3.1: *The scheelite structure of $LiYF_4$ with the tetragonal lattice.*

	Li Y F4
Acronym	YLF
Density ρ	3.99 g/cm^3
Site symmetry	Dodecahedron site, S_4 Y^{3+} site
Coordination	8-fold
Crystal system	Tetragonal, scheelite structure
Space group	$I4_1/a$, Schönfliess C_{4h}^6
Unit cell volume V	287.4 Å^3
Density of Y^{3+} ions	1.38-1.39×10^{22} cm^{-3}
Minimal distance between Y^{3+} ions	3,73 Å
Radius of the Y^{3+} ions	1.16 Å
Lattice constant	a = 5.16 Å c = 10.75 Å
Refractive indices (at 639.5 nm)	n_o = 1.453 ($\|a$, σ) n_e = 1.475 ($\|c$, π)
Optical symmetry	uniaxial
Melting point T_M	≈840 °C
Mohs hardness	4-5
Effective phonon energy E_{eff}	442-460 cm^{-1}
Thermal conductivity	6 W/mK
Thermal expansion coefficient $\alpha = \frac{1}{l} \cdot \frac{dl}{dT}$	13×10^{-6} *1/K* $\|a$ 8×10^{-6} *1/K* $\|c$
Optical transparency range	0.12-8 µm
References	[Far63,Cry73, Chi01, Sen01]

Table 3.1: *Crystal data and physical properties of the $LiYF_4$ host.*

3.2 Single rare-earth ion

The electron configuration of lanthanides is $[Xe]^1(4f)^n(5d)^x(6s)^2$ with x=1 in the case of lanthanum (n=0), gadolinium (n=7), and lutetium (n=14) and x=0 and n=2 through n=14 for cerium through ytterbium. In ionic crystals the rare-earth ions are usually incorporated as stable trivalent ions. Divalent rare earth ions can appear in crystals with divalent lattice sites. They can also appear if local charge compensation is provided by crystal defects such as F-centers or by the presence of quadrivalent co-dopants in the crystal [Loh69].

The spectroscopic properties of the trivalent rare-earth ion are dominated by transition from *4f* states to *4f* and *5d* states. Due to the completely filled *5s* and *5p* shells the *4f*-states are well shielded from influence of the crystal field [Bur62, Ray63, Ste66]. This results in a low variation of the *4f*-states in different local environments and narrow transition line-widths compared to those observed in transition metals, divalent rare earth, and RE^{3+} *5d*-states [Hen89]. The strength of the shielding decreases with rising atomic numbers [Ste66, Erd72].

The radius of the *4f* wave function and the radius of the trivalent ion decrease throughout the lanthanide row due to the stronger attraction of the electrons by the nucleus [Fre62]. This lanthanide contraction has some effects when the ion is located in the crystal field. Smaller ions generally are less affected by the crystal field of a host material than lager ions in the same host due to the larger distance of the main part of *4f* wave function to the electrostatic field of the neighbouring ions [Blo66, Ste66, Erd72].

The *4f*-shielding and the lanthanide contraction influence the strength of the electron-phonon-coupling in the rare earth ions in the host. The strength of the electron-phonon-coupling has been determined by Ellens by measuring the line widths of electronic transition and the intensities of vibronic sidebands [Ell96, Ell97a, Ell97b]. It is stronger for the elements in the beginning and the end of the lanthanide row and weaker for those in the middle. Furthermore the effects of hydrostatic pressure decrease through the lanthanide row due to the lanthanide contraction.

3.2.1 Energy levels of free ions

The simplified Hamiltonian for an atom or ion containing a nucleus of charge *Ze* and *N* electrons is given by

$$H = \sum_{i=1}^{N}\left(-\frac{\hbar^2}{2m}\vec{\nabla}_{r_i}^2 - \frac{Ze^2}{(4\pi\varepsilon_0)r_i}\right) + \sum_{i<j=1}^{N}\frac{e^2}{(4\pi\varepsilon_0)r_{ij}} \tag{3.1}$$

where $\boldsymbol{r}_i$ denotes the relative coordinate of the electron *i* with respect to the nucleus and $\boldsymbol{r}_{ij} = |\boldsymbol{r}_i - \boldsymbol{r}_j|$ the distance between electron *i* and *j*. The last summation is over all pairs of electrons. The Hamiltonian includes the kinetic energy of electrons and their potential energy in the attractive Coulomb field of the nucleus and the electrostatic (Coulomb) repulsion between the electrons. The Schrödinger equation for the *N*-electron atom or ion then reads

$$H\psi(\vec{r}_1,\vec{r}_2,...\vec{r}_N) = E\psi(\vec{r}_1,\vec{r}_2,...\vec{r}_N) \tag{3.2}$$

where $\psi(\vec{r}_1,\vec{r}_2,...\vec{r}_N)$ is purely spatial wave function. This equation is not separable and hence no analytical solution is tractable because of the presence of the terms $1/r_{ij}$, which express the mutual repulsion of the electrons.

A starting point for all calculations on many-electron atoms (ions) is the central field approximation. The basic idea is that each of the atomic electrons moves in an effective spherically symmetric potential created by the nucleus and all the other electrons (based on the independent particle model). In this approximation the Hamiltonian is now written as

$$H = \sum_{i=1}^{N}\left(-\frac{\hbar^2}{2m}\vec{\nabla}_{r_i}^2 - V(r_i)\right) \tag{3.3}$$

where $V(r_i)$ represents the potential energy of the i^{th} electron in the field of the nucleus and all other electrons. The eigenvalue equation

$$H_0\psi_0 = E_0\psi_0 \tag{3.4}$$

is separable and the solution is the product of the eigenstates of the single-electron wave function

$$\psi_c = \prod_{i=1}^{N}\left|n_i l_i m_l m_s\right\rangle \tag{3.5}$$

The energy $\Sigma E n_i l_i$ of this eigenstate only depends on the set of $n_i l_i$ values and does not depend on m_l and m_s (energy degeneracy). The Pauli exclusion principle (no two

electrons in an atom can have the same set of four quantum numbers) requires that the total wave function is antisymmetric. This is satisfied by building up the total *N*-electron wave function as a Slater determinant out of single-electron spin orbitals.

The problem arises how to determine a self-consistent potential in such a manner that solutions of equation (3.4) yield wave functions, which recover the charge distribution of the originally assumed potential. Successive iterations are used to calculate an improved potential until the final results converge to the self-consistence potential *V(r)*. This method is commonly known as Hatree-Fock approach.

Two corrections must be applied to the central field approximation. The non-spherical (non-symmetric) part of the Coulomb repulsion interactions between the electrons

$$H_{ee} = \sum_{i<j=1}^{N} \frac{e^2}{(4\pi\varepsilon_0) r_{ij}} - \sum_{i=1}^{N} \left(\frac{Ze^2}{(4\pi\varepsilon_0) r_i} - V(r_i) \right) \tag{3.6}$$

and the magnetic interactions of the electronic spins with their orbital motion

$$H_{SO} = -\sum_{i=1}^{N} \frac{1}{2m^2 c_0^2} \cdot \frac{1}{r_i} \cdot \frac{dV(r_i)}{dr_i} \cdot (\vec{s}_i \vec{l}_i) \tag{3.7}$$

can be treated as perturbation to the effective potential of the central field approximation in a calculation following the perturbation theory [Hen89]. c_o is the velocity of the light in the vacuum.

The electrostatic interaction between the rare-earth *4f*-electrons splits the energy level of the $4f^n$ configuration into different *LS* terms. The resultant wave functions are characterized by the quantum numbers *L, S,* M_L, and M_S. The energy splitting of the ^{2S+1}L terms is typically $\Delta E = 10^4$ cm^{-1}, each level is *(2L+1)(2S+1)*-fold degenerate in M_L and M_S.

If the energy separation between different *LS* terms is large compared to the spin-orbit coupling energy, there is only little mixing of *LS* terms by the spin-orbit coupling operator. If this mixing is neglected, it is known as the Russel-Saunders approximation and the wave functions are characterized by the quantum numbers *L, S, J,* M_J. In this approximation, spin-orbit coupling causes a splitting of each *LS* term into a number of states $| L\ S\ J\ M_J >$, the *J*-multiplets, each with different values of *J* and M_J. Each *J*-level is *(2J+1)*-fold degenerate, these states being characterized by the value of M_J. The energy splitting of the $^{2S+1}L_J$ terms is typically some 1000 cm^{-1}. If

the term separation is not large, then the spin-orbit-coupling operator mixes states with the same JM_J value but with different LS value. The resulting intermediate coupling eigenstates $| L' S' J M_J >$ are labelled by specific set of $L' S'$ values. The lanthanides are characterized by intermediate coupling. It is common to denote the energy eigenstates of rare-earth ions following the Russel-Saunders approximation [Hen89].

3.2.2 Rare-earth ions in the crystal field

When an ion is incorporated into a crystal lattice, it is subject to the electrostatic field of the neighbouring ions, also called ligands. The crystal-field potential can be introduced as an additional perturbation term to the free-ion Hamiltonian. In the one-electron approximation the potential can be written as:

$$H_{cf} = \sum_{k,q} B_q^k \cdot C_q^{(k)}. \tag{3.8}$$

The $C_q^{(k)}$ are tensor operators, whose matrix elements can be calculated exactly, and the crystal-field parameters B_q^k are adjustable parameters [Hue78].

The crystal-field has two effects on the energy-level structure of the free-ion: It induces a red shift on the free-ion levels, which is called nephelauxetic effect and can be explained by a reduction of the free-ion parameters [Jor71]. The second effect of the crystal-field on the free-ion is the lifting of the M_J-degeneracy of the $^{2S+1}L_J$-manifolds. Actually the interaction of the *4f* electrons with the crystal field, i.e., the electrostatic field of the surrounding ligands, represented by Hamiltonian

$$H_{Stark} = -e\sum_{k=1}^{N} \vec{E}(\vec{r}_k) \cdot \vec{r}_k \ , \tag{3.9}$$

results in the Stark energy splitting of the free ion $^{2S+1}L_J$ terms. The contribution can be treated as a perturbation as described in section (3.2.1). The lower the symmetry of the crystal field, the lower is the expected degeneracy of the ionic ground state. The theorem of Kramers asserts that no matter how unsymmetric the crystal field is, an ion possessing an odd number of electrons must have a ground state (each Stark level, respectively) that is at least twofold degenerate. Kramers degeneracy is a consequence of time-reversal invariance thus resulting in a $(2J+1)/2$-fold energy splitting of $^{2S+1}L_J$ terms for ions with an odd number of electrons. Rare-earth ions with an even number

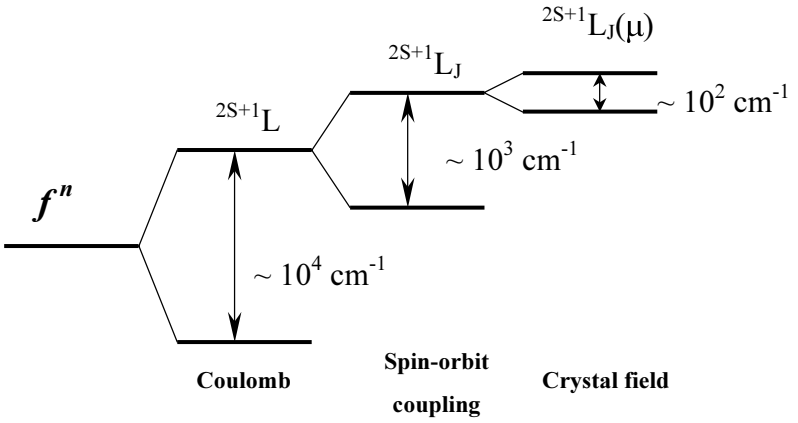

Figure 3.2: *Schematic representation of the rare-earth ion energy levels splitting.*

of electrons experience (*2J+1*)-fold Stark splitting which is typically some 100 cm^{-1} in energy (see Figure 3.2).

The ground state of the trivalent Er^{3+} ion with 11 electrons in the partially filled *4f* shell is, according to Hund's rules*, labelled by $^{2S+1}L_J = {}^4I_{15/2}$ (S = 3/2, $2S+1$ = 4, L = 0 + 1 + 2 + 3 = 6 ≡ *I*, J = 6 + 3/2 = 15/2). The ground state is (*2J+1*) = 16-fold degenerate in M_J corresponding to 8 Stark levels according to Kramer's theorem (see Figure 3.3).

The crystal-field parameters B_q^k include all the structural information of the local environment of an ion. The superposition model makes an attempt to separate intrinsic parameters from the geometrical factors. The one-electron crystal-field parameters are written as:

$$B_q^k = \sum_j \overline{B}_k(R_j) K_{kq}(\vartheta_j, \varphi_j)\,. \tag{3.10}$$

$\overline{B}_k$ is an intrinsic parameter and depends only on the distance R_j and the type of ligand located at $(R_j, \vartheta_j, \varphi_j)$. K_{kq} is a geometrical factor that includes the information about the loca1 environment. Usually only the first ligand shell is used for the calculations, while the influence of higher ligand shells is neglected. This model

* *S has its maximum value, L has its maximum value, and J = L + S for shells that are more than half filled (J = |L - S| for shells that are less than half filled) [Ash76].*

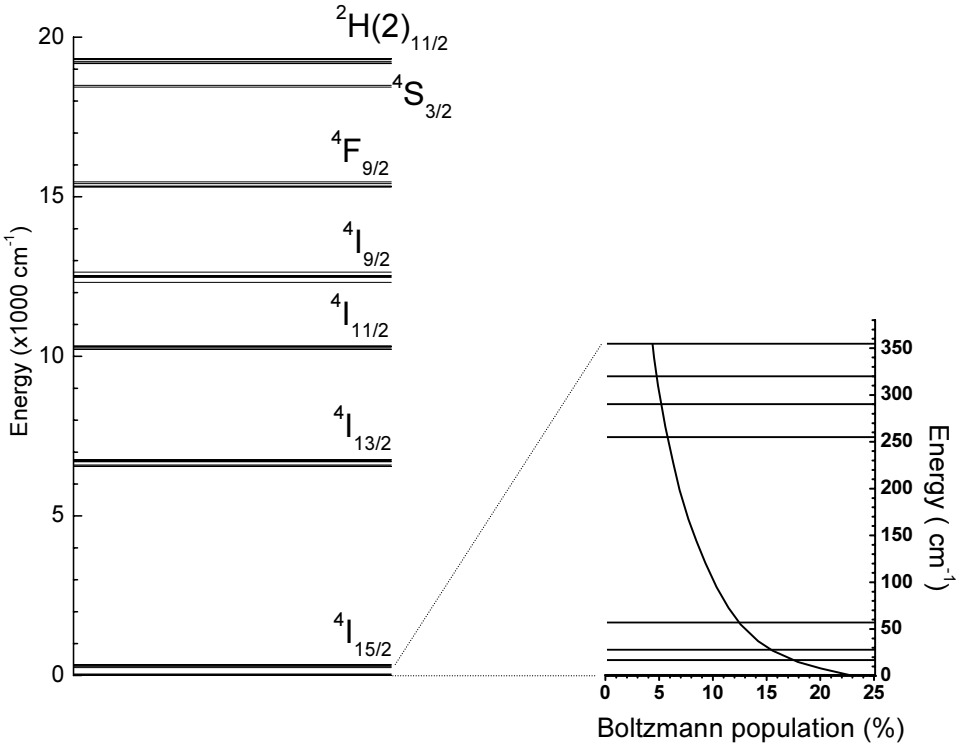

Figure 3.3*: Energy level splitting for $LiYF_4:Er^{3+}$ and thermal Boltzmann population of the ground state multiplet at room temperature according to equation (3.11).*

allows an analysis and easier comparison of the crystal-field in similar host materials or monotonously changing local environments.

The thermal population of a Stark level k (see Figure 3.3) within a multiplet according to the Boltzmann population statistics reads as

$$f_k = \frac{N_k}{N_{multi}} = \frac{g_k \cdot e^{-\frac{E_k - E_0}{k_B T}}}{Z_{multi}}. \qquad (3.11)$$

f_k is the Boltzmann factor, N_k and N_{multi} are the population densities of the Stark level k and the entire multiplet, respectively, g_k is the twofold Kramers degeneracy, E_k and E_o are the energies of the Stark level k and the lowest multiplet level, respectively, k_B is Boltzmann's constant, T the absolute temperature, and Z_{multi} the partition function of the multiplet defined by

$$Z_{multi} = \sum_k g_k e^{-\frac{E_k - E_0}{k_B T}}. \qquad (3.12)$$

3.3 Intraionic relaxation processes

The emission of light from a material originates from two types of mechanisms: thermal emission and luminescence. While in the thermal process all the atoms composing the solid participate in the light emission, in the luminescence process a very small number of atoms (impurities in most cases or crystal defects) are excited and take part in the emission of light. An impurity atom or a defect and its surrounding atoms form a luminescent or an emitting center. In most phosphors, the luminescent center is formed by intentionally incorporated impurity atoms called activators.

There are several possibilities for relaxation of an excited single ion in a solid. In the case when the absorption and emission processes occur in the same luminescent center, radiative and non-radiative intra-ionic relaxation may occur. Furthermore, transfer of the excitation energy of one ion to another (inter-ionic relaxation) is possible (see section 3.4).

3.3.1 Radiative relaxation

The elementary processes of ground-state absorption (GSA), stimulated emission, and spontaneous emission are essential for a comprehension of the interaction of radiation with matter. They were described by Einstein using the coefficients B_{ji} (absorption), B_{ij} (emission), and A_{ij} (spontaneous emission) [Ein16, Ein17]. In thermal equilibrium the population of the energy levels of a system follows the Boltzmann statistics:

$$N_j = N_i \cdot e^{-\frac{E_j - E_i}{kT}} \tag{3.13}$$

with the temperature T and population densities $N_{i,j}$ and the energies $E_{i,j}$ of the levels i and j. By comparing coefficients to Plank's radiation law:

$$E(\nu) = \frac{8\pi h \nu^3}{c^3} \frac{1}{e^{\frac{h\nu}{kT}} - 1} \tag{3.14}$$

the Einstein relations can be deduced:

$$B_{ij} = \frac{g_j}{g_i} B_{ji} \tag{3.15}$$

with the degeneracy level $g_{i/j}$ of the states and

$$\frac{A_{ij}}{B_{ij}} = \frac{8\pi h n^3 \nu^3}{c_0^3} \tag{3.16}$$

with the frequency

$$\nu = \frac{E_i - E_j}{h} \tag{3.17}$$

n is the refractive index of the material and $E_{i/j}$ is the energy of the state $| i/j >$, respectively. The transition rate for spontaneous emission of a photon in the dipole approximation is :

$$W_{ji} = \frac{4}{3\hbar c^3} \left(\frac{e^2}{4\pi\varepsilon_0} \right) \cdot \omega_{ij}^3 \left| \mu_{ij} \right|^2 \tag{3.18}$$

with the dipole matrix element μ_{ij} and the speed of light within the material c [Sve93].

The radiative lifetime τ_{rad} of an excited state $| i >$ is defined as the reciprocal of the sum of the spontaneous radiative transition rates to all energetically lower levels $| j >$:

$$\tau_{rad}(|i\rangle) = \frac{1}{\sum_j A_{ij}} . \tag{3.19}$$

The branching ratio β_{ij} determines the percentage, that one transition $| i > \rightarrow | j >$ takes up of the entire transition rate from a state $| i >$:

$$\beta_{ij} = \frac{A_{ij}}{\sum_k A_{ik}} . \tag{3.20}$$

Excited-State Absorption

Besides ground-state absorption (GSA), stimulated and spontaneous emission it is possible to have absorption from excited metastable levels in the scheme of energy levels of a rare-earth ion. These excited-state absorption (ESA) processes are of special interest for the erbium ion with its several partly resonant transitions.

If the ESA transition is resonant to the pump wavelength it is usually considered as loss mechanism since the pump efficiency into a specific energy level

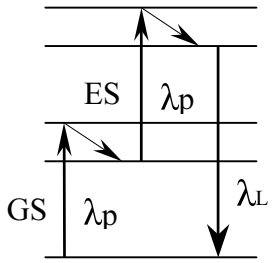

Figure 3.4: *Illustration of the excited-state absorption; (ESA) exploited to populate high lying energy levels*, λ_p *– pumping photon,* λ_L *- emitted photon.*

by GSA is reduced (see Figure 3.4). On the other hand it is possible to excite energy levels higher in energy than the single pump photon energy by means of ESA transitions.

3.3.2 Non-radiative relaxation

Multi-phonon-relaxation is the transition of an excited state into a lower one by interaction with one or more lattice phonons. The excitation energy is directly transformed into heat by this process. Multi-phonon relaxation into energetically close levels is very fast and can efficiently depopulate excited states. The temperature dependence of non-radiative transition rate W_{nr} is described by [Moo70]:

$$W_{nr}(T) = W_0 \cdot e^{-a\Delta E}\left[1 - e^{-\frac{\hbar\omega_{eff}}{kT}}\right]^{-p}. \qquad (3.21)$$

The empirical parameter W_0 depends on the host material, and a describes the electron-phonon coupling, which can be considered weak in the case of *4f* electrons. ΔE is the energy difference between the two states and $\hbar\omega_{eff}$ is the effective phonon energy of the host material. The number of phonons needed to bridge the energy gap is given by $p = \frac{\Delta E}{\hbar\omega_{eff}}$. Usually, at low temperature $\hbar\omega_{eff} > kT$ and the temperature dependence in Equation (3.21) can be neglected. In the phenomenological approach it is postulated [Moo70] that the ratio of the pth and $(p-1)$th processes will be given by some coupling constant:

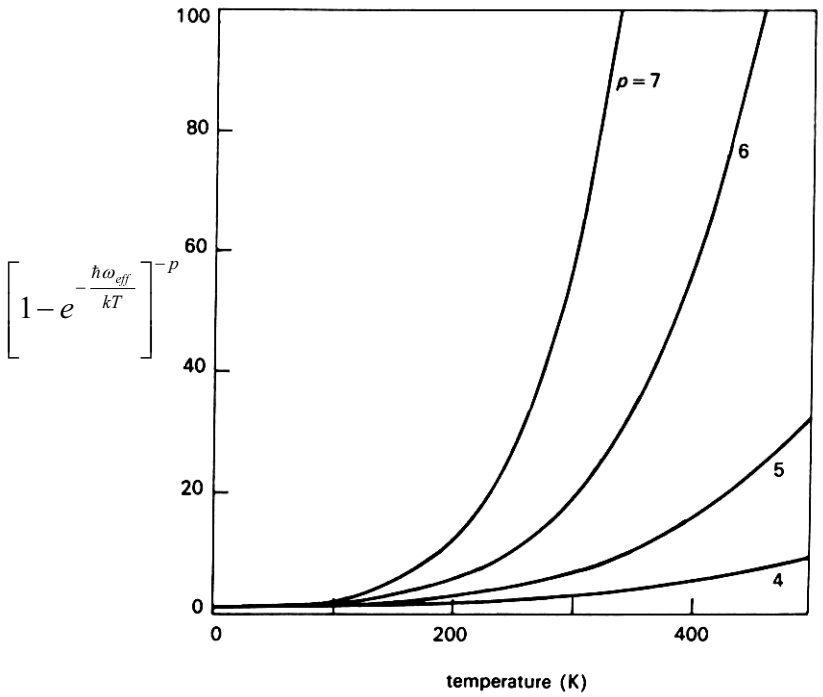

Figure 3.5: *A plot of* $\left[1-e^{-\frac{\hbar\omega_{eff}}{kT}}\right]^{-p}$ *for a process across a gap of 1200 cm*$^{-1}$ *using four different decay modes: four phonons each of 300 cm*$^{-1}$*, five phonons each of 240 cm*$^{-1}$*, six phonons each of 200 cm*$^{-1}$*, and seven phonons each of 171 cm*$^{-1}$ *[Hen89].*

$$\varepsilon = \frac{W_{nr}^{(p)}}{W_{nr}^{(p-1)}} \langle\langle 1 \tag{3.22}$$

characteristic of the host crystal but not the rare-earth ion electronic state. ε varies only slowly with p. For a given lattice at low temperature the spontaneous relaxation rate varies approximately as

$$W_{nr}^{(p)} = A \cdot \varepsilon^{p} \ . \tag{3.23}$$

Generally, the lowest order process dominates and $\hbar\omega_{eff} = \hbar\omega_{max}$. Hence, at low temperature

$$W_{nr} = W_o \cdot e^{\alpha \cdot \Delta E} \ . \tag{3.24}$$

Figure 3.5 shows a plot of $\left[1-e^{-\frac{\hbar\omega_{eff}}{kT}}\right]^{-p}$ for a process across a gap of 1200 cm^{-1} using four different processes: four phonons each of 300 cm^{-1}, five phonons each of 240 cm^{-1}, six phonons each of 200 cm^{-1}, and seven phonons each of 171 cm^{-1}. The

temperature dependences are quite distinct so that one should be able to infer from the observed temperature dependence of the number of phonons involved (p) and hence the energy of the effective phonons ($\Delta E/p$). In general, the variation with temperature of non-radiative transition in rare earth ions is accurately described by Equation (3.21). The calculation of the absolute value of W_{nr} is, however, a very difficult task [Hen89].

The non-radiative lifetime of an excited state is defined as

$$\tau_{nr} = \frac{1}{W_{nr}}. \tag{3.25}$$

The fluorescence lifetime can now be calculated from the radiative (Equation 3.19) and non-radiative lifetime:

$$\frac{1}{\tau} = \frac{1}{\tau_{rad}} + \frac{1}{\tau_{nr}}. \tag{3.26}$$

The fluorescence lifetime can be determined experimentally from the decay of the fluorescence intensity I, which is single exponential in the most simple case:

$$I(t) = I(0) \cdot e^{-\frac{t}{\tau}}. \tag{3.27}$$

3.3.3 Selection rules for radiative transitions

The optically active *4f* electrons of the rare-earth ions are shielded by the outer, though less energetic, *5s* and *5p* shells electrons. Therefore the interaction of the *4f* electrons with the crystal field is small, electron-phonon-coupling effects are weak and optical transitions between $4f^n$ states are characterized by sharp lines. Since these transitions occur between states of the same parity, magnetic dipole processes are expected for the free ion rather than electric dipole transitions (Laporte selection rule) [Hen89]. However, if the rare-earth ion occupies a crystal site without inversion symmetry, a mixing of opposite-parity states of the $4f^{(n-1)}5d$ (or another) configuration into the $4f^n$ states can occur. Even a small admixture of odd-parity states induces a small electric dipole component to the transition since the transition probability for magnetic dipole processes is some five orders of magnitude lower and

their amplitude is smaller than for electric dipole processes[*] by about the fine structure constant $\alpha \approx 1/137$. Higher order transitions such as electric or magnetic quadrupole processes can usually be neglected due to their minor transition probabilities. General selection rules for electric dipole transitions between rare-earth ion $4f^n$ states are:

- $\Delta J \leq 6$, $\Delta S = 0$, $\Delta L \leq 6$ (Russel-Saunders approximation)

- For a rare-earth ion with an even number of electrons:
  1. $J = 0 \leftrightarrow J' = 0$ is forbidden
  2. $J = 0 \leftrightarrow$ odd values are weak
  3. $J = 0 \leftrightarrow J' = 2, 4, 6$ should be strong

Electric dipole transitions between $4f^n$ states require an admixture of opposite-parity states (such as $4f^{(n-1)}5d$ states) by an odd-parity crystal field component. The effect of this mixing was investigated by Judd and Ofelt [Jud62, Ofe62]. By measuring the oscillator strength (which is defined as the square of the corresponding dipole matrix element μ_{ji} of a radiative transition between energy states j and i) of a number of ground-state transitions, the values for the so-called Judd-Ofelt intensity parameters Ω_l, which characterize the strength and nature of the odd-parity crystal field, can be determined. Once these parameters have been evaluated for a given rare-earth-doped crystal they can be used to calculate electric dipole transition strengths (absorption and emission) between any two levels of the system. With this result it is possible to deduce the general selection rules for electric dipole transitions.

---

[*] *The transition rate W_{ji} for an electric dipole transition between an initial state $|j\rangle$ and a final state $|i\rangle$ is given by Fermi's golden rule*

$$W_{ji} = \frac{2\pi}{\hbar}\left|\langle i|p|j\rangle\right|^2 \rho(E_i) = \frac{2\pi}{\hbar}\left|\mu_{ji}\right|^2 \rho(E_i)$$

where $\boldsymbol{p} = e\boldsymbol{x}$ is the dipole operator, $\rho(E_i)$ the energy density of final state, and μ_{ji} the corresponding dipole matrix element. The term $2\pi/\hbar$ is referred to as an amplitude and $|\mu_{ji}|^2$ denotes the transition probability or oscillator strength [Hen89].

3.4 Interionic relaxation processes

Interionic processes are energy transfer processes induced by electric or magnetic multipole interactions between two or more involved ions. Interionic interactions become prominent in crystals with high doping concentrations and for high pump radiation intensities. These processes can be important for the population dynamics of energy levels and are often the reason why fluorescence decays of rare-earth ions in solid-state materials show non-exponential characteristics.

3.4.1 Radiative interionic processes

Reabsorption

In case of reabsorption the energy is transferred from one ion to another through a real photon. In lifetime measurements, reabsorption can cause a lengthening of the fluorescence lifetime. The reabsorption losses per round trip in the crystal are given by

$$L_{reabs} = 2 \cdot (1 - e^{-\sigma_{reabs} N_j d}), \tag{3.28}$$

where σ_{reabs} denotes the effective reabsorption cross section (taken from the absorption spectrum), N_j the entire population density of the ground-state multiplet, and d the length of the crystal sample [Hen89].

3.4.2 Non-radiative interionic processes

Energy migration

Energy migration is the resonant energy transfer between two ions of the same type (Figure 3.6 (a)). This process allows the excitation energy to quickly spread out and therefore raises the probability of the other energy transfer processes. Energy migration is described by several models depending on the ratio of transfer rates between two donors C_{DD} and between donor and acceptor C_{DA}. Right after the excitation a fast migration of the excitation energy between donors occurs. After this first, fast migration to neighbouring ions, the further spreading of energy can be either

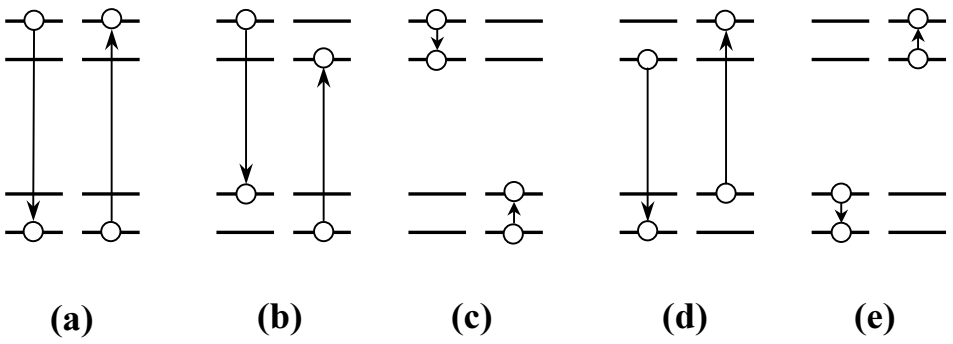

Figure 3.6: *Interionic processes: (a) energy migration, (b) and (c) cross relaxation, (d) and (e) upconversion.*

described by the diffusion-model in the case that C_{DD} is much smaller than C_{DA} [Yok67] or the hopping-model for C_{DD} larger than C_{DA} [Bur72].

Due to the strong dependence of the transition probabilities on the distance between donor and acceptor, the energy transfer processes become most important at high doping levels. This can be very useful if energy transfer is desired as in sensitised systems or can be harmful if the excitation energy is transferred away from the active ion to unwanted impurities. In the case of highly doped systems, energy transfer to such impurities can cause a nearly complete quenching of the excitation energy [Lac92].

Cross relaxation

Figure 3.6 (b) and (c) describe cross relaxation mechanisms. These are energy transfer processes in which the donor excitation energy is used to excite the acceptor ion. For the case of two different ions A and B, the mechanism is referred to as quenching if the donor ion is the laser ion and as sensitisation if the acceptor ion is the laser ion. In general, the excited level of the donor ion before the interaction is higher in energy than the terminating level of the acceptor ion after the interaction. Cross-relaxation is often used to sensitise ions with small absorption cross section by co-doping with ions with strong absorption, to achieve a more efficient excitation.

Upconversion

The reverse process of a cross relaxation is upconversion, shown schematically in Figure 3.6 (d) and (e). The terminating level of the acceptor ion is higher in energy than the excited level of the donor ion before the interaction. Upconversion processes can be exploited (just as excited-state absorption) as pump mechanism to populate high lying energy levels of a specific ion. By this it is possible to convert the low excitation energy of pump photons into high energy fluorescence or laser photons. Hence upconversion lasers are operating with an emission wavelength shorter than the pump wavelength. Unlike upconversion, excited-state absorption is an intraionic process. Upconversion mechanisms can be particularly helpful to depopulate a lower laser level, simultaneously feeding back the energy into the upper laser level. These processes become relevant for high doping concentrations and can be exploited to achieve laser operation, e.g., for the Er^{3+} 3-μm laser transition [Her90].

The probability for a dipole-dipole energy transfer process between a donor ion D and an acceptor ion A is given by

$$W_{DA} = \frac{3\hbar^4 c_0^4 Q_A}{4\pi n^4 R_{DA}^6 \tau_{rad,D}} \int \frac{f_D(E) F_A(E)}{E^4} dE \equiv \frac{C_{DA}}{R_{DA}^6} \tag{3.29}$$

where $Q_A = \int \sigma_A(E) dE$ denotes the integral over the acceptor absorption cross section, $\tau_{rad,D}$ is the radiative lifetime of the donor ion level, n is the refractive index, and c_o is the velocity of light [Foe48, Dex53]. The final term in equation (3.29) accounts for the overlap integral of the normalised emission and absorption line shape, $f_D(E)$ ($\int f_D(E) dE = 1$) and $F_A(E)$ ($\int F_A(E) dE = 1$), respectively. R_{DA} is the distance between the donor and acceptor ion. The $1/R_{DA}^6$ dependence is characteristic of the dipole-dipole interaction; higher multipole interactions are represented by higher-order powers of $1/R_{DA}$. The microparameter $C_{DA} = \frac{3\hbar^4 c_0^4 Q_A}{4\pi n^4 \tau_{rad,D}} \int \frac{f_D(E) F_A(E)}{E^4} dE$ is a measure of the transfer efficiency. Interionic processes are possible between same and different kind of ions. The transfer rate increases with higher dopant concentrations of the involved ions.

3.5 Luminescence decay

Different models have been developed to analyse luminescence decays. Simplest case is single exponential decay described by equation :

$$I(t) = I_0 \cdot \exp(-\frac{t}{\tau}) . \tag{3.30}$$

Interionic processes such as energy migration or cross-relaxation can lead to a lengthening or to a shortening of the decay time accordingly. So, to take into account such energy transfer processes, Equation (3.30) has to be modified to:

$$I(t) = I_0 \cdot \exp\left(-\frac{t}{\tau} - t \cdot W(t) \right), \tag{3.31}$$

where *W(t)* is the rate of the energy transfer processes responsible for the depopulation of the excited state of the given ions. The energy transfer rate from donor *D* to acceptor *A* was first investigated by Förster [Foe48] and Dexter [Dex53] for dyes (see Equation 3.29). Later, this theory was extended for solids doped with rare-earth ions as well.

Starting from (3.31), Inokuti and Hirayama [Ino65] developed another model for the non-radiative energy transfer with following assumptions:

1. Donor and acceptor are statistically separated;
2. There exists only one channel for energy transfer;
3. There are no donor-donor-interaction or acceptor–donor-back-transfer processes.

The expression they obtained

$$I(t) = I_0 \cdot \exp\left(-\frac{t}{\tau_0} - \Gamma(1-\frac{3}{s}) \cdot \frac{n_A}{C_k} \cdot \left(\frac{t}{\tau_0} \right)^{3/s} \right) \tag{3.32}$$

describes the fluorescence decay and is a non-exponential function of time t. Γ is the gamma-function, n_A is the acceptor concentration, τ_o is the radiative lifetime of the donor. *s* denotes the multipole order and is equal to 6 for dipole-dipole transitions, to 8 for dipole-quadrupole and to 10 for quadrupole-quadrupole transitions. C_k represents a critical acceptor concentration and is defined in terms of a range parameter R_o:

$$C_k = \frac{1}{4/3 \cdot \pi R_0^3}, \tag{3.33}$$

where

$$\frac{1}{\tau_0} = \frac{C_{DA}^{(s)}}{R_0^s}, \tag{3.34}$$

and means that when the concentration of acceptor reach the critical value C_k, the Förster-Dexter transfer rate between a donor and an acceptor with the average donor-acceptor separation equals the radiative relaxation rate of a donor.

After substituting all parameters for dipole-dipole interaction, Equation (3.32) reads:

$$I(t) = I_0 \cdot \exp\left(-\frac{t}{\tau_0} - \gamma \cdot \sqrt{t}\right), \tag{3.35}$$

where

$$\gamma = \frac{4}{3}\pi^{3/2} n_A \cdot \sqrt{C_{DA}}\,. \tag{3.36}$$

The so-called microparameter C_{DA} is a characteristic constant of the given ion and host (see Equation (3.29)). Moreover C_{DA} is independent of the doping concentration.

One of the initial assumptions of the Inokuti-Hirayama model is the absence of the donor-donor-interactions. If the donor-donor transfer occurs in addition to the donor-acceptor transfer, this migration of the donor excitation can greatly add to the complexity of the problems [Hen89].

The starting point is the set of coupled equations [Hub79]:

$$\frac{dP_n(t)}{dt} = -\left(\frac{1}{\tau_o} + X_n + \sum_{n'} W_{nn'}\right) \cdot P_n(t) + \sum_{n'} W_{n'n} P_{n'}(t)\,, \tag{3.37}$$

where $P_n(t)$ is the probability that the nth donor ion is excited at time t. $W_{nn'}$ is the donor-donor transfer rate from the nth donor to the n'th donor, X_{nl} is the donor-acceptor transfer rate from the nth donor to the l'th acceptor, and $X_n = \Sigma X_{nl}$ where the summation is over all acceptors. τ_o is the intrinsic decay time of the excited donor ion. The value of X_n depends on the arrangement of acceptor ions in the vicinity of the nth donor ion. The number of excited donor ions is found by multiplying the total number of donor ions (N_D) with the configurational average of $P_n(t)$ over all arrangements of donors and acceptors. This configurational average is

$$\langle P(t)\rangle_c = \frac{1}{N_D}\sum_n P_n(t) \tag{3.38}$$

and the intensity of donor luminescence is proportional to $N_D \cdot \langle P(t)\rangle_c$.

Two limiting cases can take place: the so called *static* case when no donor-donor transfer occurs, and the case of very rapid donor-donor migration.

In the static case $W_{nn'} = W_{n'n} = 0$ and an exact solution of (3.37) was first derived by Inokuti and Hirayama [Ino65]:

$$\langle P(t)\rangle_c = \exp(-\frac{t}{\tau_0}) \cdot \prod_l \left(1 - C_A + C_A \exp(-X_{0l} \cdot t)\right), \tag{3.39}$$

where indices *0* and *l* refer to the sites in the lattice and X_{0l} is the transfer rate from a donor at the site *0* to an acceptor at the site *l*. C_A is the probability that a site is occupied by an acceptor. Using a continuum approximation, Inokuti and Hirayama [Ino65] derived Equation (3.32). The decay is in general non-exponential and the initial part varyies as

$$rate(t \to 0) = -\frac{1}{\tau_0} - C_A \cdot \sum_l X_{0l} \ . \tag{3.40}$$

The other limit applies to a situation where transfer between donors is extremely rapid in comparison with a donor-acceptor rate. In this case all donors have an equal probability of being excited for all times of interest. The excitation migrates between so many donor ions that it senses the average environment of acceptor ions. Exact solution of the rate equation (3.37) for this case was obtained by Huber [Hub79]:

$$\langle P(t)\rangle_c = \exp(-\frac{t}{\tau_0}) \cdot \exp\left(-\langle X\rangle_c \cdot t\right), \tag{3.41}$$

where $\langle X\rangle_C = C_A \sum_l X_{0l}$ denotes the configurational average of the donor-acceptor transfer rate.

Despite the qualitative differences in the two limits both equations (3.39) and (3.41), they both have the same initial slope $\frac{dP(t \to 0)}{dt} = -\frac{1}{\tau_0} - C_A \cdot \sum_l X_{0l}$, which is independent of the donor-donor transfer rate. Physically the situation is that immediately after the exciting pulse all donors have an equal probability of being

occupied and, as a result, the donor excitation senses the average acceptor environment [Hen89].

The intermediate regime between the static case without donor-donor transfer and the case of very rapid donor-donor migration is more difficult to treat. Two approximate approaches are employed. The first approach was derived by Yokota and Tanimoto [Yok67] and treats the migration of excitation among donors as a diffusion process. After replacement of $P_n(t)$ as the physical quantity of interest by $\rho(\vec{R},t)$ - the density of excited donors, the configurational average of $P_n(t)$ over all arrangements of donors and acceptors is replaced by analogous quantity $\phi(t) = \int \rho(\vec{R},t) d^3\vec{R}$. In this case equation (3.37) takes the form

$$\frac{\partial \rho(\vec{R},t)}{\partial t} = -\frac{1}{\tau_o}\rho(\vec{R},t) + D\nabla^2 \rho(\vec{R},t) - \sum_{l=1}^{N_A} W_{DA}(\vec{R}-\vec{R}_l)\rho(\vec{R},t)\,. \tag{3.42}$$

An approximate solution of equation (3.42) for the case of dipole-dipole donor-acceptor transfer has been given by Yokota and Tanimoto:

$$\phi(t) = \exp\left[-\frac{1}{\tau_o} - \frac{4}{3}\pi^{\frac{3}{2}} n_A (C_{DA}\cdot t)^{\frac{1}{2}} \left(\frac{1+10.87y+15.5y^2}{1+8.743y}\right)\right]^{\frac{3}{4}}, \tag{3.43}$$

where

$$y = \frac{D\cdot t^{\frac{2}{3}}}{(C_{DA})^{\frac{1}{3}}}\,. \tag{3.44}$$

D is the diffusion constant which characterizes the migration among donor ions and depends on both donor-donor transfer rate and on the density of donors. For the dipole-dipole transfer one has [Hub79]:

$$D = \frac{1}{2}\left(\frac{4}{3}\pi n_D\right)^{\frac{4}{3}} C_{DD}\,. \tag{3.45}$$

Here, n_D is donor concentration, and the characteristic constant C_{DD} is a measure of the donor-donor transfer efficiency for the given ion in the given host.

At sufficiently long times the decay becomes exponential and this asymptotic decay rate is (donor-accepter transfer is dipole-dipole process)

$$\frac{1}{\tau} = \frac{1}{\tau_o} + W_{DA}^{diff} = \frac{1}{\tau_o} + 8.5 n_A (C_{DA} D^3)^{\frac{1}{4}} . \qquad (3.46)$$

It has to be mentioned that in the case of no diffusion, the equation (3.43) obtained by Yokota and Tanimoto is reduced, as expected, to the form given by equation (3.35) in Inokuti-Hirayama model.

The second approach to the problem was discussed by Burshtein [Bur72] and treats the migration of excitation among donor ions as a random walk process. The decay function of the donors is given now by equation

$$\phi(t) = \langle P(t) \rangle_c \exp(-\frac{t}{\tau_D}) + \frac{1}{\tau_D} \int_0^t \phi(t-t') \langle P(t') \rangle_c \exp(-\frac{t'}{\tau_D}) dt' \qquad (3.47)$$

where $\langle P(t) \rangle_c$ is the decay function of the donors in the absence of the donor-donor transfer, i.e. Equation (3.39). τ_D is the averaged time that the excitation resides on a donor ion before hopping to another donor ion. The respective ratio for dipole-dipole transfer is given now by [Wat75]

$$\frac{1}{\tau_D} = \left(\frac{2\pi}{3} \right)^3 n_D^2 C_{DD} . \qquad (3.48)$$

The solution to equation (3.47) can be obtained by numerical methods. It is found that initially the decay function (3.47) is non-exponential but for large t values it becomes exponential [Hen89] with asymptotic decay rate

$$\frac{1}{\tau} = \frac{1}{\tau_D} + W_{DA}^{hopping} = \frac{1}{\tau_D} + C_A \cdot \sum_l \frac{X_{0l}}{1 + \tau_D X_{0l}} \quad . \qquad (3.49)$$

In case of very rapid hopping rate, $\tau_D \rightarrow 0$, the decay is exponential at all times with decay rate $\frac{1}{\tau_0} + C_A \cdot \sum_l X_{0l}$.

Finally, summarising all foregoing and taking into account subsequent analysis of the models [Heg81, DiB84, Bur85, Bla94, Lup01], expression for the luminescence decay in the general case takes the form:

$$I(t) = I_0 \cdot \exp\left(-\frac{t}{\tau_0} - \gamma \cdot \sqrt{t} - W_D \cdot t \right) \quad , \qquad (3.50)$$

where γ is given by equation (3.36), and W_D is an ensemble-averaged migration-assisted energy transfer rate between donors. τ_o is the lifetime of the emission at very low concentrations, when the energy transfer can be neglected. Both the diffusion model and the hopping model are approximate, but not equivalent, approaches to the general problem of donor-acceptor energy transfer in the presence of donor-donor migration. Huber [Hub79] has investigated the regions of validity of both models, and the general problem has been extensively reviewed by Burshtein [Bur85].

3.6 Intraconfigurational $4f^n$-$4f^n$ transitions

The intraconfigurational $4f^n$-$4f^n$ transition takes place when an electron of the RE^{3+} is promoted from the ground $4f^n$ state to the excited state of the $4f^n$ configuration. As it was already mentioned, due to the completely filled *5s* and *5p* shells the *4f*-states are well shielded from influence of the crystal field. As a result of small interaction of the $4f^n$ electrons with the crystal field and weak electron-phonon coupling, the optical transition between $4f^n$ states are characterized by sharp lines. Because of the fact that the electric-dipole moment of the optical $4f^n$ -$4f^n$ transitions is zero, these transitions are forbidden by parity selection rule and are expected to occur by the magnetic dipole process. This results in weak intensity transitions. On the other hand, if the rare-earth ion occupies a crystallographic site without inversion symmetry, a mixing of opposite-parity states of the $4f^{n-1}5d$ configuration into the $4f^n$ states occur, forced by the uneven components of the crystal field [Ash76, Hen89]. The admixture of even- and odd-parity states allows the electric dipole component to the transition. Since the electric dipole process is some five orders of magnitude stronger and their amplitude is larger than for magnetic dipole processes by about the fine structure constant $\alpha \approx 1/137$, even a small admixture of odd-parity states changes significantly the intensity of the intraconfigurational transition.

3.7 Interconfigurational $4f^n$- $4f^{n-1}5d$ transitions

Transition occurring between $4f^n$ configuration and $4f^{n-1}5d$ configuration of opposite parity are parity allowed. This gives rise to the strong absorption bands. Due to the large spatial extension of the *d*-orbital, the absorption bands of *f-d* transitions are broad and widely vibronic in character. Moreover, the influence of the surrounding in the position of the lowest energy *f-d* band is substantial. Due to the crystal field splitting and the *nephelauxetic* effect (means (electron)cloud expanding [Bla94]) , the position of the *5d* levels may change by tens of thousand cm^{-1} from compound to compound. The energetic position of the lowest *f-d* transition of all lanthanides in a certain host lattice are related: once the spectral position is known for one rare-earth ion in a certain lattice, the position of the lowest *f-d* band of the other rare-earth ions can be predicted [Dor[1]00, Dor[2]00, Dor[3]00]. The *f-d* transition for the trivalent lanthanide ions are mainly located in VUV (with the exception of Ce^{3+} and Tb^{3+}). For the heavy lanthanide ions ($4f^n$, n > 7) spin-forbidden excitation and emission bands have been observed in addition to the spin-allowed *f-d* bands. The occurrence of both spin-allowed and spin-forbidden *f-d* transition is explained in chapter 4.1 by the example of Er^{3+}. Spin-forbidden transitions as well as spin-allowed transitions are observed for all heavy lanthanides. The splitting between the low spin and high spin *fd* state decreases with increasing nuclear charge of the lanthanide ion. The radiative lifetime of the spin-allowed *f-d* transitions is in the range of nanoseconds, and of the spin-forbidden transitions in a microsecond range.

Recently, much progress in the calculation of the *fd* energy levels has been made. Calculation on the *fd* levels of Pr^{3+} [Lar00] and Ce^{3+}, Pr^{3+} and Nd^{3+} [Rie00] in $LiYF_4$ have been reported. An extensive overview of the *fd* excitation spectra of the lanthanides is given by van Pieterson [Pie01]. The structure in the *fd* excitation spectra of the lanthanides in phosphates and fluorides hosts was calculated using a theoretical model that extends established models for the $4f^n$ configuration by including crystal field and spin-orbit interactions for the *5d* electron and the Coulomb interaction between the *4f* and *5d* electrons [Pie02]. Calculations of the positions of the $4f^{n-1}5d$ energy levels were compared with the experimental data. A good agreement was obtained between experiment and theory using parameters for the splitting of the *5d* state (from the Ce^{3+} spectra), the $4f^{n-1}5d$ splitting (from the

literature) and the *f-d* Coulomb interaction (calculated for the free ion using Cowan's code). The *5d* crystal field parameters were slightly reduced to account for the slight reduction of the crystal field splitting for the heavier rare earth ions (~ 9% between Ce^{3+} and Tm^{3+}). The *f-d* interaction parameters were reduced to 67% of the free ion value for the fluorides and to 60% of the free ion value for the phosphates to correct for the nephelauxetic effect. The larger reduction of the *f-d* interaction parameters in the phosphates was explained by the larger covalency of the phosphate host lattice as compared to the fluoride lattice. The presence of both high spin and low spin *fd* states and the trend that the splitting between the high spin and low spin states decreases through the series is reproduced by the theory. In Figure 3.7 the excitation spectrum for $LiYF_4$ doped with 2% Er^{3+} obtained by van Pieterson [Pie01] is shown monitoring the $^4S_{3/2} \rightarrow ^4I_{15/2}$ emission at 550 nm at 10 K. A number of broad bands is observed, some of which show fine structure. Transition to higher *5d* crystal field components are observed at 140 nm (C) and 126 nm (F). The calculated spectra are presented as the dotted lines. The experimentally observed transition intensities at short wavelength (<125 nm) are much lower than the calculated ones. This fact was assigned to the effect of the host lattice absorption in the $LiYF_4$ [Pie01].

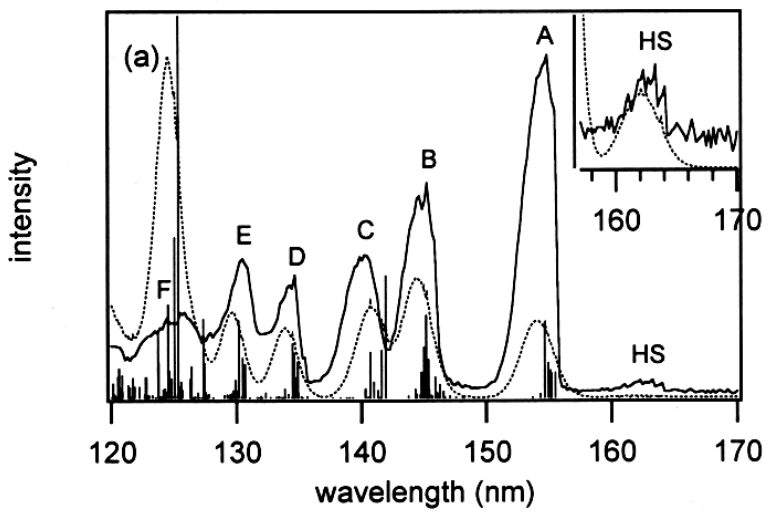

Figure 3.7: *Excitation spectrum for $LiYF_4$ doped with 2% Er^{3+} obtained by van Pieterson [Pie01] and monitoring the $^4S_{3/2} \rightarrow ^4I_{15/2}$ emission at 550 nm at 10 K. The solid line shows the excitation spectrum measured at DESY, the dotted line represents the calculated spectrum. Positions of the calculated electronic states are indicated by vertical lines.*

3.8 Interconfigurational charge transfer transitions

The charge transfer transitions are, just as $4f^n \rightarrow 4f^{n-1}5d$ transitions, inter-configurational transitions, and are parity allowed. A *ligand-to-metal charge transfer* (LMCT) transition is often described as the transfer of an electron from the ligands to the central metal ion ($M^{n+}L^{m-} \rightarrow M^{(n-1)+}L^{(m-1)-}$, here M is the central metal ion and L is a ligand) [Pie01, Kru95, Kru97]. The transfer of the electron causes a considerable reorganization of the charge density distribution around the metal ion which, is accompanied by a delocalisation of the electron clouds and by an expansion of metal-ligands bonds in the excited state. This results in a large transition dipole moment and a large oscillator strength.

The trivalent rare-earth ions that have a tendency to become divalent (Sm^{3+}, Eu^{3+}, Yb^{3+}) show charge transfer absorption bands in the ultraviolet. The trivalent rare-earth ions that have a tendency to become tetravalent (Ce^{3+}, Pr^{3+}, Tb^{3+}) show $4f^n \rightarrow 4f^{n-1}5d$ absorption bands in the ultraviolet [Bla94].

The energetic position of the charge transfer band depends strongly on the electronegativity of the ligand, electron affinity of the lanthanide ion and the ligand-metal distance. The energy change between f^n and f^{n+1} configurations during this type of charge transfer process is formulated in the spin-pairing energy theory of Jørgensen [Jor62, Jor71], which was developed first for the *d*-elements by Griffith [Gri61] and revisited by [Nug74] for the *f*-series.

Jørgensen's refined spin-pairing energy theory has been generally found effective for correlation and prediction of energy of charge transfer band in a variety of lanthanides complexes. The energy changes when an electron is added to a f^n configuration as follows:

$$E_{CT} = W - n(E - A) + \frac{9}{104}N(S)E^1 + M(L)E^3 + P(S,L,J)\zeta_{4f} \qquad (3.51)$$

where W would correspond to the energy transfer of an electron from the ligand (*2p MO*) to the *4f*-shell of Ln^{3+}. This model assumes that all electron shieldings are perfect and effects of the repulsion as well as the spin–orbit or relativistic interactions among the *f*-electrons are excluded. E-A in Equation (3.51) reflects the difference between stronger nuclear attraction E and increased interelectronic repulsion A across

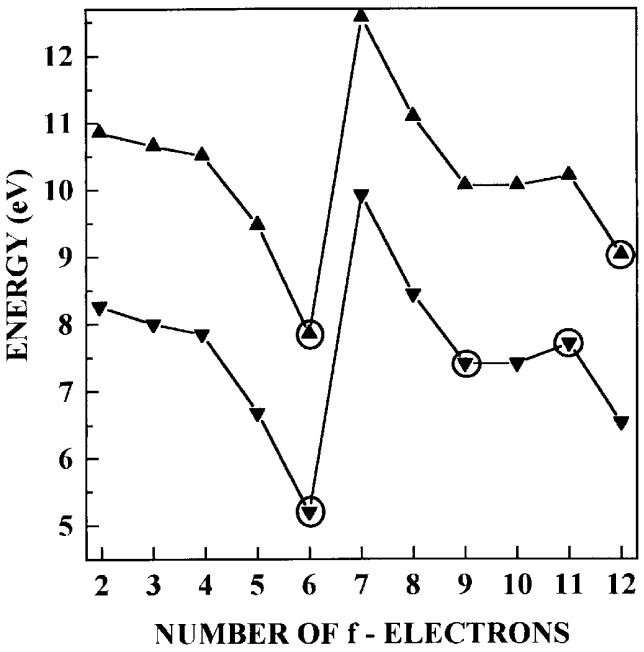

Figure 3.8: *Energy of the charge transfer band in fluorides (▲) and oxides (▼). Open circles are for experimental values. Data was obtained by Belsky and Krupa [Bel99].*

the *4f*-shell when the nuclear charge is increasing. $N(S)E^1$ is the difference in spin-pairing energy for the f^n and f^{n+1} configurations. The first-order Racah parameter E^1 of inter-f-electron repulsion is assumed to be the same for both the (III) and the (II) oxidation states. $M(L)E^3$ reflects the energy differences between terms with the maximal spin S_{max}; the function $M(L)$, where L is the total electron orbital angular momentum quantum number, represents the difference between the coefficients of the Racah inter-f-electron repulsion parameter E^3 in the ground electronic state of (III) and (II) oxidation state respectively. $P(S, L, J)\zeta_{4f}$ expresses the influence of the spin–orbit coupling [Bel99].

Belsky and Krupa [Bel99] have calculated the energies of charge transfer $F^- \rightarrow Ln^{3+}$ in fluoride systems using formula (3.51). Respective results are represented in Figure 3.8.

For most of the trivalent rare-earth ions, especially around the middle of lanthanide series charge transfer and *f-d* transitions are overlapping strongly and the structure of the observed excitation band can not be completely resolved [Kru97]. In order to observe charge transfer luminescence, the charge transfer states should be localized below the lowest energy excited $4f^{n-1}5d$ state. Furthermore, no $4f^n$ energy levels should be present at energies comparable to the charge transfer state, otherwise this will result in fast intersystem crossing to the low energy $4f^n$ states and $4f^n$-$4f^n$ emission.

Chapter 4

Experimental results and discussion

4.1 Luminescence of Er^{3+} in $LiYF_4$ crystal

The first experiments with main emphasis on the role of *d*-levels dates back to the seventies. In the pioneering papers by Elias et al. [Eli73, Hea76], and Heaps *et al*. [Hea76], VUV excitation spectra of visible *f-f* emission, covering typical *4f-5d* excitations of RE^{3+}-ions in a LnF_3 host, were already established. The *d-f* luminescence of *RE*-ions in the UV spectral range is under investigation for a long time. A systematic collection and analysis of data was recently published by Dorenbos [Dor[1]00, Dor[2]00, Dor[3]00]. The investigation of *d-f* emissions of rare earth ions in the VUV spectral range also started long ago [Yan76]. But only in the last few years, the VUV *d-f* emissions really attract attention. Due to the difficulties involved in VUV luminescence spectroscopy, only a few groups went into this field. Most results up to now have been obtained with synchrotron radiation as an excitation source.

In the first experiments on $LiYF_4:Er^{3+}$, the main emphasis was put on time-resolved *d-f* luminescence measurement. This enabled to identify fast and slow components which, however, were incorrectly assigned until Wegh et al. [Weg98] ascribed them to spin-allowed and spin-forbidden transitions. In the meantime, additionally to the VUV emission bands, the *f-f* luminescence following selective *f-d* and *f-f* excitation were investigated as well. In a recent comprehensive study experimentally observed $4f^n$-$4f^{n-1}5d$ transitions of all RE ions in the various hosts have been compared with the calculated spectra [Pie02].

Figure 4.1 shows an overview of time-integrated Er^{3+} luminescence in $LiYF_4:Er^{3+}$(1%) at T=10 K under primary excitation with $h\nu$=9.8 *eV* photons ($\Delta\lambda$=0.3

nm) corresponding to the transitions into the higher *d*-states. The intensities are given in arbitrary units.

The purpose of the Figure 4.1 is to compare the *d-f* and *f-f* emission occurring from VUV to IR. As in our experiment such a wide range cannot be covered by the combination of a single monochromator and detector, two monochromator-detector systems were used to record these spectra. In order to discuss the curves represented in Figure 4.1 some remarks concerning the sensitivity of the analysing systems has to be done.

In the UV-VUV spectral range, the sensitivity curve of the VUV monochromator-detector (solar blind PMT) system is rather flat between 150 and 250 nm. Above 250 nm the detector sensitivity rapidly decreases to approximately one third at 290 nm. Since the transmission curve of the VUV monochromator is not known the VUV emission spectrum in the range 150-280 nm was only corrected for the quantum efficiency of the detector.

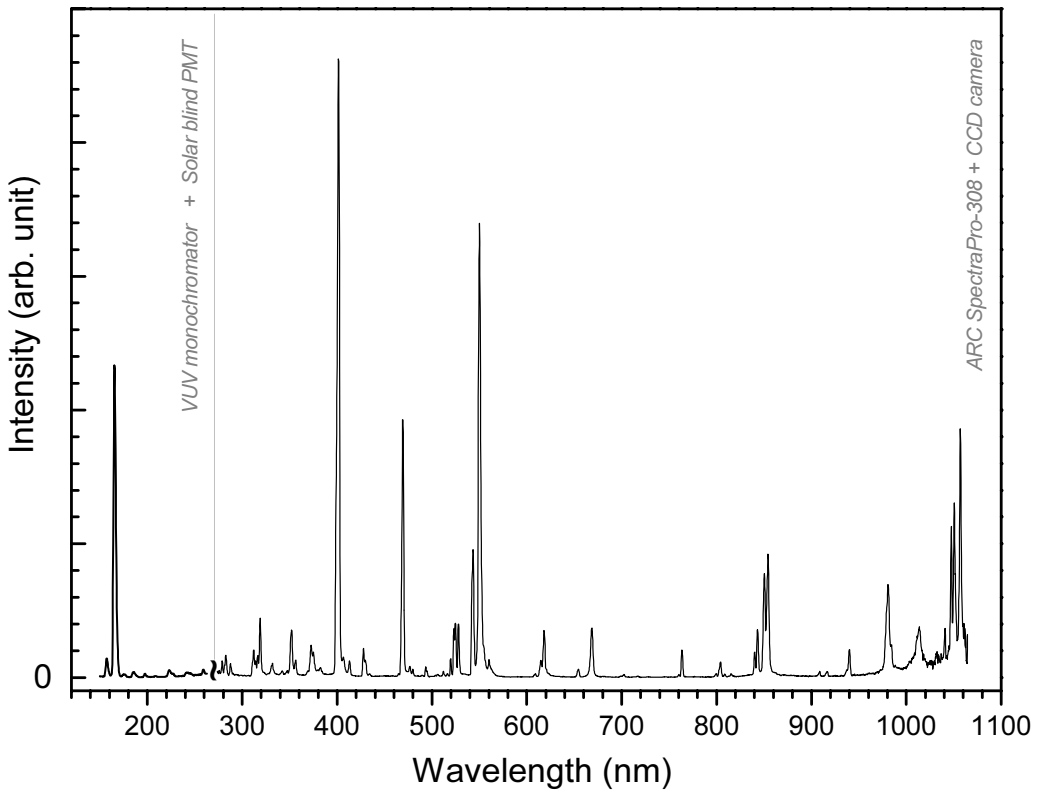

Figure 4.1: *Time-integrated luminescence spectrum of $LiYF_4:Er^{3+}$(1%) at T=10 K, excited with 9.8 eV photons.*

The UV-visible-IR part of the spectra was recorded using ARC SpectraPro-308 spectrometer equipped with the CCD camera. The sensitivity curve of the CCD camera in the range of the sharp *f-f* lines shows variations by approximately 30% between 290 nm and 700 nm, but then rapidly decreases towards the infrared part of the spectrum. At 1000 nm, the sensitivity is about a few per cent of the maximum at 450 nm (see section 2.4.2). The emission spectrum measured in the UV-visible-infrared range (actually, from 300 nm to 1100 nm) was corrected for the transmission curve of the corresponding monochromator-detector system. The break between two curves is situated at about 270 nm. After these correction for the apparatus function, the spectra were matched together according to the common bands in the UV range. The corrected curves illustrate the relative intensities of *d-f* transitions in the VUV and of *f-f* transitions covering a spectroscopic range from UV to infrared. However, one should be critical regarding the obtained results because there are several factors influencing the relative intensities of the peaks that were not taken into account.

Some information about ratio between *d-f* and *f-f* emission intensities can be also obtained from the spectra represented further in Figure 4.5.

4.1.1 *d-f* luminescence

The field of vacuum ultraviolet spectroscopy of lanthanide ions has become an important field of research. Mainly because of experimental difficulties, the VUV spectroscopy of lanthanide ions has remained a largely unexplored field until recently.

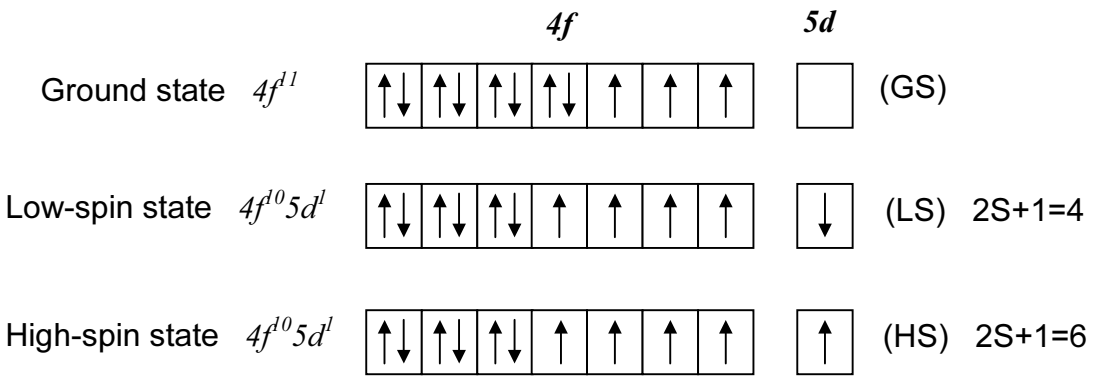

Figure 4.2: *Schematic electron configurations for the ground state (GS), the higher lying low-spin $4f^{10}5d$ state (LS), and the energetically lowest high-spin $4f^{10}5d$ state (HS) of the Er^{3+} ion.*

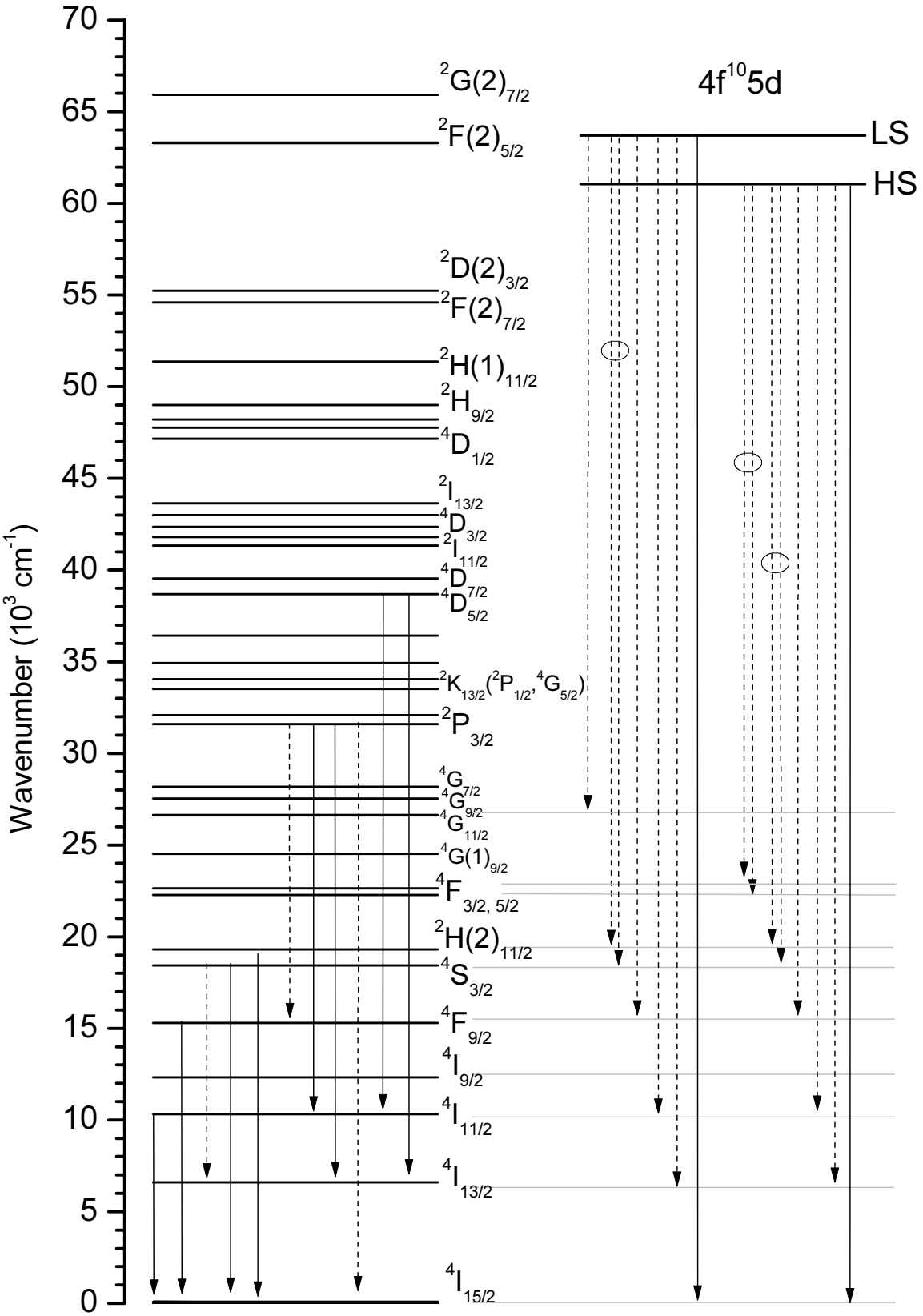

Figure 4.3: *Simplified energy level scheme of $LiYF_4:Er^{3+}$. The most intense lines and bands observed are indicated by full arrows. Weaker emissions are shown as dashed arrows. In few cases, the final states cannot be resolved in the spectra, therefore, the respective arrows are marked by an ellipse.*

Potential applications have now triggered a worldwide increase in activity in this area. The applications involving the VUV spectroscopy of lanthanides are scintillator materials and VUV lasers. In these applications $4f^{n-1}5d$-$4f^n$ transitions of lanthanides can be used. The VUV *f-d* emission can also be used to obtain tuneable solid-state lasers operating in the VUV according to the classical 3 level scheme, involving ground, low-spin and high-spin states.

The positions of *5d*-levels depend strongly on the crystalline environment; they may change by tens of thousand cm^{-1} from compound to compound [Dor²00]. This is in contrast to the energy of the electronic levels of the well shielded 4f electrons which remain constant within several hundreds cm^{-1}. As it was already mentioned, *f-d* transitions cause broad emission bands, generally in the UV and vacuum UV energy range. Wide emission and absorption bands are typical for the *5d-4f* transitions due to the coupling of the *5d* electrons with the lattice phonons. An additional effect is the Stark splitting of the $4f^n$ multiplets by the crystal field interaction. Usually, this Stark splitting of the $4f^n$ multiplets is not resolved in the *5d-4f* emission spectrum but it does add the broadening to the emission bands.

Before proceeding to the detailed consideration of the measured spectra, the following remarks concerning the energy level scheme of the Er^{3+} ion in $LiYF_4$ are necessary. The spin configurations for the ground state ($4f^{11}$) and the two possibilities of the spin configuration for the excited $4f^{10}5d$ state are depicted in Figure 4.2. In the ground state (GS), the total spin quantum number *S* is 3/2 (three unpaired spins), so the spin multiplicity $2S+1$ is 4 (quartet state). In the $4f^{10}5d$ configuration the spin for the electron in the *5d* orbital can be either antiparallel with four unpaired parallel spins in the $4f^{10}$ core, giving rise to a low-spin state (LS) with a total spin quantum number S=3/2 (quartet excited state). Or it can be parallel, giving a high-spin state (HS) with S=5/2 (sextet excited state). The latter state will be lower in energy (Hund's rule), but transitions from the ground state to this excited $4f^{10}5d$ state will be spin-forbidden. Because of the spin-forbidden character of the transition, this *f-d* emission of Er^{3+} has a decay time in the microsecond range ($\tau_{rad\ (HS)}$ = 2.4 μs). Transitions to the higher energetic quartet state are spin-allowed. In addition to the spin-forbidden emission, fast spin-allowed emission ($\tau_{rad\ (LS)}$ = 84 ns) from the higher energetic $4f^{10}5d$ state is also observed.

A simplified energy level scheme of $LiYF_4$:Er^{3+} is shown in Figure 4.3 (see also Appendix C, p. 144). The assignments of the dominant transitions are given in the

figure. They are deduced from [Jay89, Cou98, Weg99] ([Cou98] was basically used up to 43000 cm^{-1}, information about higher lying levels was obtained from [Weg99]). For the $4f^{10}5d$ levels, experimental values of the energetic positions obtained in the given work were taken (the position of the HS level was deduced from the zero-phonon line, observed in the excitation spectra and the position of the LS state corresponds to the position of the respective emission peak). The observed strong

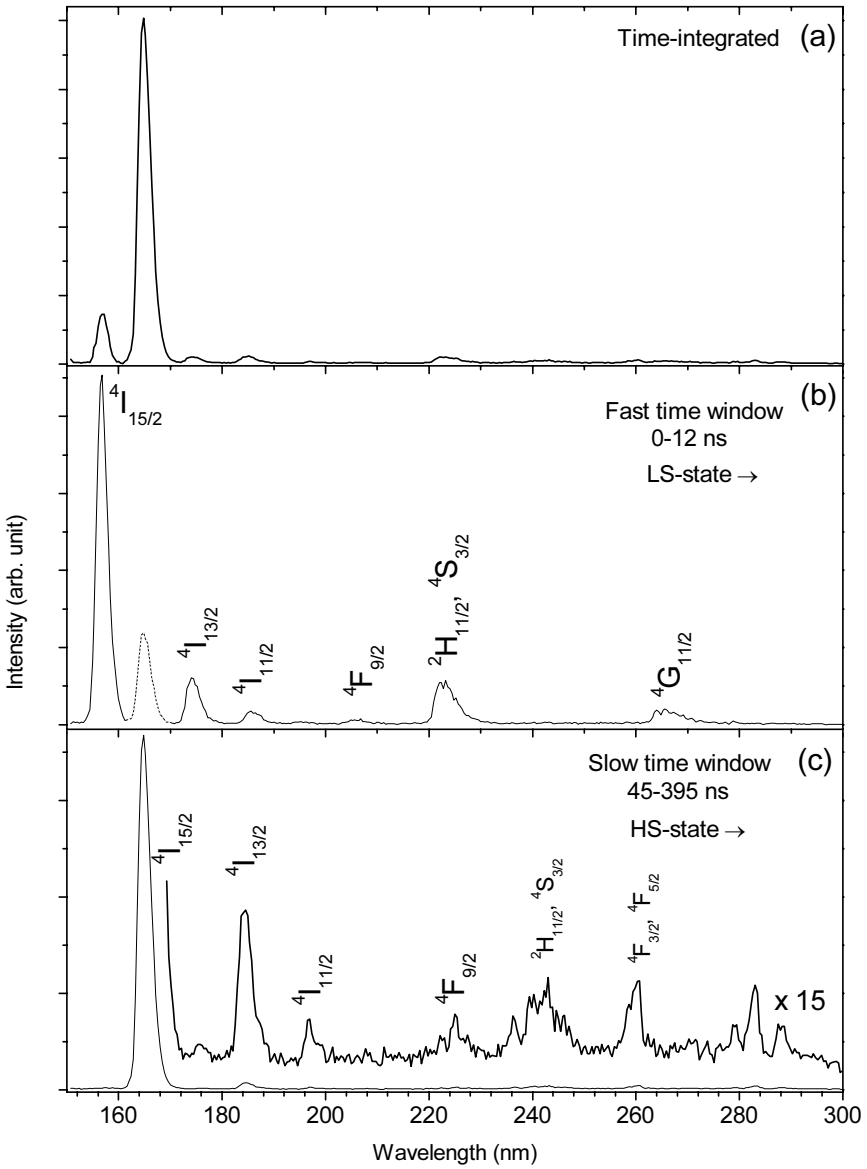

Figure 4.4: *Luminescence of $LiYF_4:Er^{3+}$(1%) at T = 10 K, excited with 10.8 eV photons. (a) time-integrated; (b) fast time window from 0 to 12 ns; (c) slow time window from 45 to 395 ns. The dominant peak of the curve named "slow" also contributes to the curve (b) due to the temporal overlap of both components (dotted part of the curve).*

transitions are indicated by full arrows, the weak transitions by dashed arrows. In a few cases, the final states cannot be resolved in the spectra, therefore, the respective arrows are marked by an ellipse. A detailed table of the energy levels of Er^{3+} ion in $LiYF_4$ host is given in Appendix C.

Figure 4.4a shows a time-integrated emission spectrum of $LiYF_4:Er^{3+}$ (1%) at T=10 K, excited with 10.8 eV photons. Upon excitation to the strong spin-allowed $4f^{10}5d$ bands, several *d-f* emission bands are observed. Most of the emission bands can be assigned to emission from the lowest energetic (sextet) $4f^{10}5d$ state to the different $4f^{11}$ states. The strongest *d-f* emission band at 166 nm corresponds to the transition to the $^4I_{15/2}$ ground state. At longer wavelengths, emission bands to the $^4I_{13/2}$ (185 nm), $^4I_{11/2}$ (197 nm), $^4I_{9/2}$ (206 nm), $^4F_{9/2}$ (224 nm), and $^4S_{3/2}$ (244 nm) states can be observed. Time-resolved measurements which are helpful to distinguish between fast and slow emission are shown as well (Fig. 4.4b, 4.4c). The curve named "fast" was measured within a time interval ("time window") from 0 to 12 ns (time zero is given by the arrival of the respective excitation pulse). The curve named "slow" represents the luminescence intensity in a time window in which the spin-allowed emission is practically negligible (45 to 395 ns, repetition rate of excitation: 2 MHz).

Therefore, it consists of spin-forbidden *d-f* emission originating from the lowest high-spin excited state. The dominant peak of the curve named "*slow*" also contributes to the curve named "*fast*" due to the temporal overlap of both components (dotted part of the curve in Fig. 4.4 b).

The spin-allowed emission includes not only the strong main band terminating at the ground state but also remarkably intense transitions to a variety of final states, whereas the spin-forbidden emission mainly terminates at the ground state. The transitions from energy levels of $4f^{10}5d$ configuration to energy levels of $4f^{11}$ configuration are electric-dipole transitions. The electric-dipole transition rate is proportional to the electric-dipole matrix element $|\mu_{ij}|^2$, and the frequency of the radiation ω_{ij}^3 (see Equation 3.18). The ω^3 dependence favours the transitions to the ground state. Nevertheless, in an enlarged scale, very weak sidebands are established as well. In other words, from the emitting low-spin state, *f* levels are efficiently populated via radiative transitions, whereas radiative energy transfer from the emitting high-spin *d*-level to *f*-levels above the ground state is weak. As will be shown below, similar results are also established for non-radiative intraconfigurational transitions starting from the HS and the LS states.

Time-integrated *d-f* emission spectra of $LiYF_4:Er^{3+}$ have already been measured before [Weg98, Pie01]. They are in good agreement with the present results. However, the time-resolved spectra presented in this work reveal more details than the time-integrated spectra given by Wegh et al. and L. van Pieterson et al. Only two fast bands were assigned in [Weg98, Pie01], and most of the weak emission bands at longer wavelengths were assigned to transitions starting from the HS state. The present time-resolved results clearly show that such side bands are only strong in spin allowed (fast) emission. The assignments deduced from the time-resolved spectra are given in Table 4.1. No line shape analysis has been performed. For the weak bands, the values are only accurate within ±300 cm^{-1}. The results are valid for T = 10 K. The weak peak at 57.000 cm^{-1} (175 nm) in the 'slow' spectrum could not be assigned. There is also a possibility that due to the rather poor resolution of the emission monochromator in the VUV and spectral overlap some sharp *f-f* emission bands are hidden in the broad *d-f* luminescence.

Initial state / Final state	Energetic position (cm^{-1})	
	HS-state→	LS-state→
$^4I_{15/2}$	60 600	63 800
$^4I_{13/2}$	54 100	57 500
$^4I_{11/2}$	50 700	53 900
$^4F_{9/2}$	44 500	47 700
$^2H_{11/2}$, $^4S_{3/2}$	41 400	44 900
$^4F_{3/2\,,\,5/2}$	38 400	—
$^4G_{11/2}$	—	37 600

Table 4.1: *Assignment of d→f emission bands starting from the lowest HS and LS state. The energy values of the centres of the emission bands are given.*

4.1.1.1 Soft X-ray excitation

A set of the measurements has been carried out also under excitation by soft X-rays photons at the BW3 station of HASYLAB (For more details see Appendix B). The exciting photon energy exceeds the band-gap of the host matrix by about an order of magnitude. Therefore the relaxation processes leading to the light emission can be different from that observed under lower energy excitations, namely in the transparency range of $LiYF_4$ crystal, where *d*-absorption bands are located.

An emission spectrum of $LiYF_4$:Er(5%) at 10 K under 150 eV excitation is shown in Figure 4.5. An additional broad band appears with the maximum at 260 nm which is not observed under the excitation in the transparency range of the crystal (see also the discussion of the intrinsic emission later). The decay kinetic of this luminescence band is slow compared to the *d-f* transition. These two facts allow also to assign broad band peaking at 260 nm in the doped crystal to the emission of the

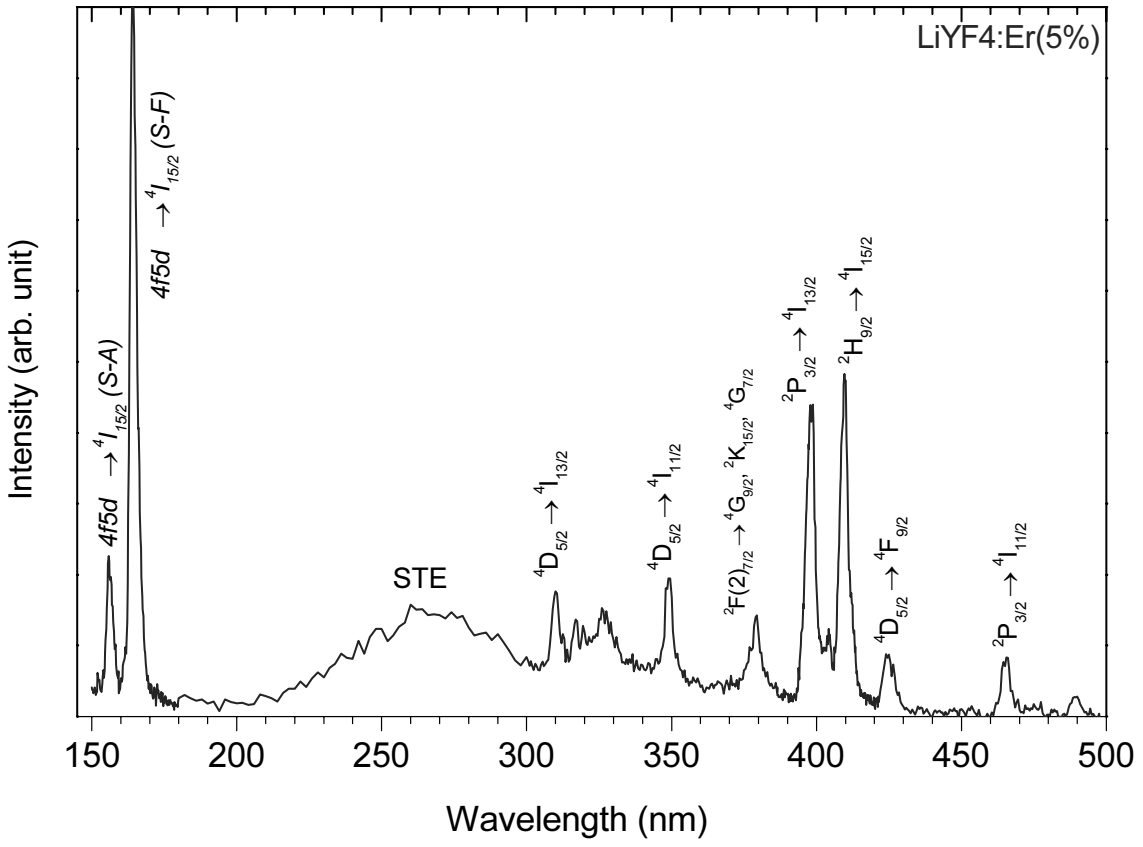

Figure 4.5: *Luminescence spectra of $LiYF_4$:Er(5%) crystal under excitation by the 150 eV at 10 K.*

self-trapped excitons (STE) as it has been identified in undoped $LiYF_4$ crystal [Hay80]. The inner shell excitation leads to the formation of electron-hole pairs, efficiently relaxing into STE states which decay radiatively. STE emission can also be reabsorbed by the overlapping *f-f* lines thereby transferring energy to the Er^{3+} ion.

It is interesting to note that strong *d-f* emission bands are present under inner shell excitation. As *d-f* emission is not efficiently excited in the host absorption region (≤ 22 eV) [Mak00], another excitation mechanism, which will be discussed later, is responsible for the excitation of *d*-bands.

The spectrum depicted in Figure 4.5 allows to discuss the relationship between *d-f* and *f-f* transitions. Again, additional remarks about spectral sensitivity of the analysing monochromator and detector system need to be made. The luminescence set-up consists of a Seya monochromator equipped with a MCP-PMT (*Hamamatsu R1645 U-09*). The monochromator is optimised for the VUV range but in combination with above-mentioned detector one can record the spectra up to 500 nm (determined by the mechanical range).

The *d-f* emission bands are the most intense peaks in the spectrum shown in Figure 4.5 (compare with the spectra shown in Figure 4.1). In spite of the fact that this emission spectrum was recorded using the same monochromator-detector system, unfortunately, it still does not reproduce a proper relationship between observable intensities of *d-f* and *f-f* transitions. The quantum efficiency of the detector (technical data sheet) is highest around 400 nm, but on the other hand the grating efficiency decreases strongly towards long wavelength (the transmission curve of the Seya monochromator is not available).

It is also not excluded that relaxation mechanism of the RE ions excited with soft X-rays can be different from that occurring under the direct excitation of *d*-levels. This question needs obviously further studies and the problem concerning intensity relationship between *d-f* and *f-f* luminescent transitions needs subsequent experimental efforts.

4.1.1.2 High temperature experiments

It is of special interest to learn more about the non-radiative decay processes and their influence on the *d-f* emission of the rare earth ions. For this purpose the luminescence originating from *d-f* transitions of Er^{3+} in $LiYF_4$ was investigated in a wide temperature range up to about 900 K until this emission becomes thermally quenched (see Figure 4.6). It is needs to be mentioned that emission spectra obtained for the temperature higher than 300 K were measured under different condition (measurements at high temperature require a special sample holder). Thus, absolute intensities for two sets of emission spectra (above and under 300 K) can not be compared.

As one can see from Figure 4.6 the fast S-A luminescence becomes negligible already at 470 K, as the probability of nonradiative transfer to the sextet state of the

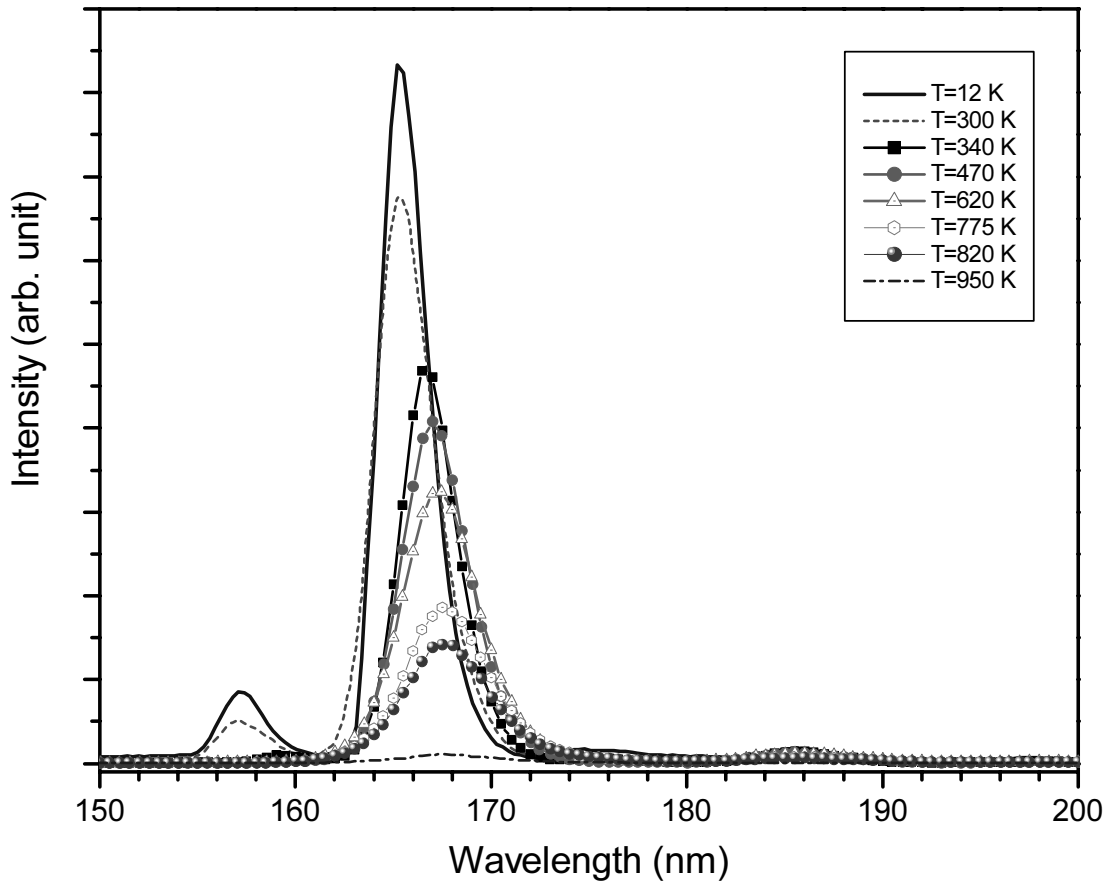

Figure 4.6: *Set of the emission spectra for $LiYF_4$:Er(5%) excited with 9 eV photons at different temperatures. See text more details.*

$4f^{10}5d$ configuration increases with temperature. As the temperature is raised, the emission bands broaden. The center of gravity of the band also shifts with temperature to longer wavelengths.

In case of Gaussian line shapes, the phonon broadening for local optical centers in the vibrating lattice is described by the following formula [Coo00]:

$$W(T) = \hbar\omega_{ph}\left[8 \cdot S \cdot \ln 2 \cdot \coth\left(\frac{\hbar\omega_{ph}}{2 \cdot kT}\right)\right]^{1/2} \qquad (4.1)$$

where S, the Huang–Rhys parameter, is the dimensionless measure of the impurity-ion-lattice coupling strength.ω_{ph} is the phonon frequency, and k is the Boltzmann constant. Figure 4.7 shows the temperature dependence of the of SF *d-f* luminescence band widths, $W(T)$, extracted from the Gaussian fits of the band. Statistical errors derived from the fitting procedure are smaller than the size of the plotted symbols. The solid line represents the best fit of the data to Equation 4.1 from which the values of ω_{ph} and S were extracted.

The value of the effective phonon energy $\hbar\omega_{ph}$ (one should take into account that at least several phonon frequencies take part in the interaction and hence ω_{ph} represents an averaged phonon frequency) resulting from the fit is equal to ~370 cm^{-1} (45.8 meV), which is less than the phonon cut-off frequency $\hbar\omega_{LO}$ (570 cm^{-1} [Mil70])

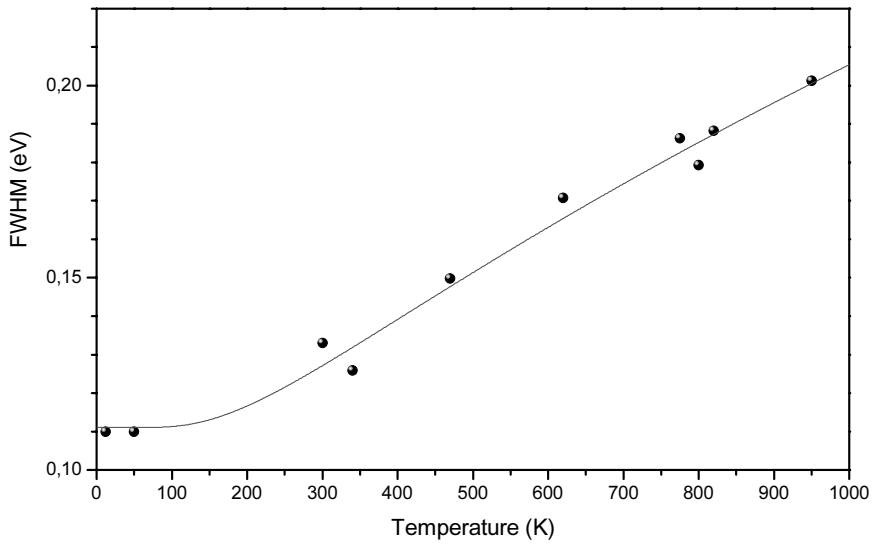

Figure 4.7: *Temperature dependence of the SF 5d–4f luminescence bandwidth of $LiYF_4$:Er(5%) (dots – experimental data; line – fit according to Equation 4.1).*

in $LiYF_4$. At the same time, this result is in a good agreement with that obtained by Renfro *et al.* [Ren80]. They studied temperature dependence of the $^4S_{3/2}$ emission lifetimes of Er^{3+} in $LiYF_4$ using the Huang-Rhys and Struck-Fonger treatments of multiphonon decay. The effective phonon energy in the $LiYF_4$:Er^{3+} system was found to be 331 cm^{-1}.

The Huang–Rhys parameter obtained in this work, S =1.01, indicates intermediate coupling between the impurity ion and the lattice and also implies a Stokes shift (i.e. doubled relaxation energy) of ~740 cm^{-1}, which nearly corresponds to the value obtained from the comparison of emission and excitation spectra (see next section). Moreover, the zero-phonon line can be observed in the spectra (see Chapter 4.2 this work or, for example, [Weg98]), which also indicates that in this systems the case of intermediate coupling is realized.

The temperature dependence of S-F *5d-4f* luminescence intensity was fitted by the Mott formula (see Figure 4.8a):

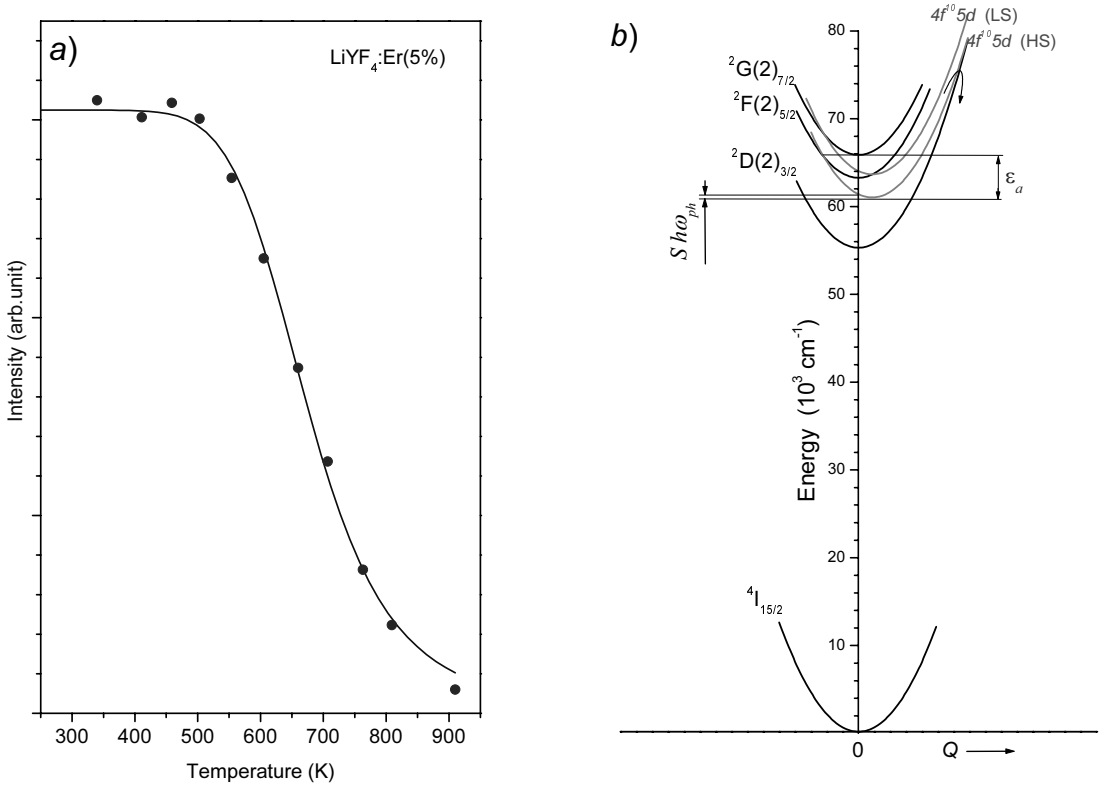

Figure 4.8: *a)Temperature dependence of the SF 5d–4f luminescence intensity of $LiYF_4$:Er(5%) (dots – experimental data; line – fit according to Equation 4.2). Excitation energy was 9 eV; b) Schematic configuration coordinate diagram of energy levels for Er^{3+} in $LiYF_4$. For the simplicity, only discussed levels are shown.*

$$I(T) = \frac{1}{1 + A \cdot e^{-\frac{\varepsilon_a}{kT}}} \tag{4.2}$$

which gives a value of the activation energy ε_a = 0.60 ± 0.03 eV for the thermal quenching of *5d-4f* luminescence in $LiYF_4$:Er. According to the present work, the respective energy difference between the lowest high-spin *d*-state and above lying $^2F(2)_{5/2}$, LS $4f^{10}5d$ and $^2G(2)_{7/2}$ states are 2250 cm^{-1} (0.28 eV), 2644 cm^{-1} (0.33 eV) and 4872 cm^{-1} (0.604 eV) respectively (see Appendix C). As it is shown in the configurational coordinate diagram (Figure 4.8b) the crossing of the states does not occur at their equilibrium. Thus the real energy differences discussed above are bigger than the calculated ones. The parabolas shown in Figure 4.8b are not calculated theoretically but are drawn in intelligent way for the qualitative discussion of the observed effect. The knowledge of the Huang-Rhys parameter and the effective phonon energy* lets estimate which process with the activation energy ε_a depopulates the lowest *d*-level. One of scenarios assumes that some of the higher lying levels mentioned above can be populated with subsequent cross-relaxation.

Another possibility is the thermally activated relaxation through the lower lying *f*-states as it was suggested in [Kha00]. The energy gap between the lowest high-spin *d*-state and $^2D(2)_{3/2}$, $^2F(2)_{7/2}$ (see Figure 4.3) is ~6000 cm^{-1}. The efficient nonradiative multiphonon relaxation occurs when the gap between levels is only four to five times larger than the cut-off phonon energy of the crystal [Mei99]. The nonradiative decay of the excited HS $4f^{10}5d$ state may occur in this case as a result of thermally activated relaxation over an energy barrier between crossing potential curves for the HS $4f^{10}5d$ state and $^2D(2)_{3/2}$, which is shown in the Figure 4.8b by the curved arrow [Kha00]. However, from the figure becomes evident that for the $LiYF_4:Er^{3+}$ this barrier is to high to be bridged with ε_a = 0.6 eV. At the same time the activation energy ε_a corresponds very well to the energy barrier between HS and above lying $^2F(2)_{5/2}$. Moreover, comparison of the potential curves for LS state and $^2F(2)_{5/2}$ state shows that these states are nearly degenerated and thermally activated population of the $^2F(2)_{5/2}$ leads to the population of the LS state, which has a much higher non-radiative decay probability (see expression (3.29) taking into account that the intrinsic

---

* *Within the linear coupling case all parabolas have the same shape (defined by the effective phonon) and only positions of parabolas are different. The displacement of parabolas, describing $4f^{10}5d$ levels, along Q-coordinate is defined by S and ω_{ph} (see Figure 4.8b).*

lifetime of state is several orders of magnitude shorted than that for *f*-states). So, most probable process responsible for the quenching of the spin-forbidden luminescence in $LiYF_4:Er^{3+}$ is thermally activated relaxation through the LS state.

4.1.2 Visible and infrared luminescence

Another application in which the VUV spectroscopy of lanthanides is involved are new luminescent materials (phosphors) for VUV excitation. They are required for plasma display panels and mercury-free fluorescent tubes, where the VUV emission from a noble gas discharge (e.g., xenon) is used to generate visible luminescence [Bla94]. For these applications, the intra-configurational *f-f* transitions of rare earth ions are important.

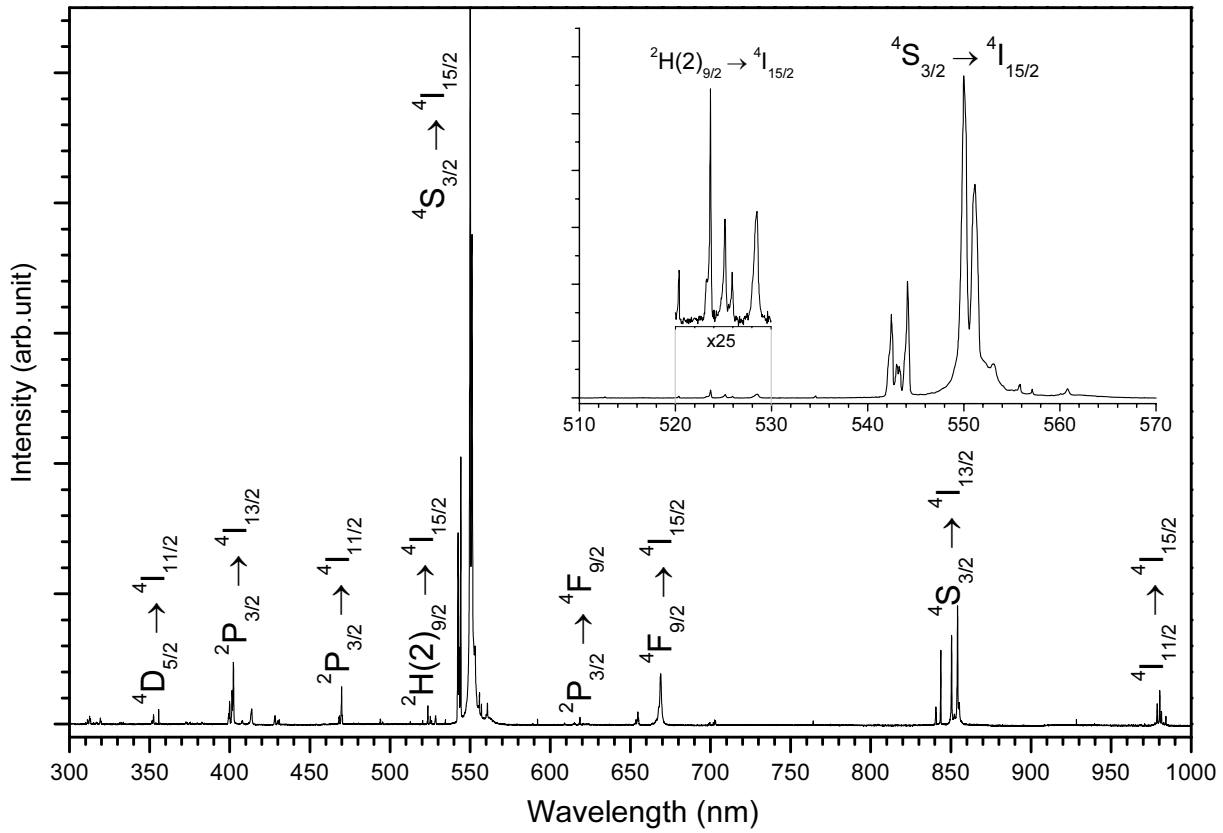

Figure 4.9: *Luminescence of $LiYF_4$:Er(5%) at T=10 K. Excitation was achieved with VUV photons (hν=10.8 eV). The assignments of the most intense lines are given in the figure.*

The energy levels of the trivalent Er ion arising from $4f^n$ configuration are also given in Figure 4.3. In a configurational coordinate diagram these levels appear as parallel parabolas, because the *4f* electrons are well shielded from the surroundings. Emission transitions yield, therefore, sharp lines in the spectra. One can clearly distinguish between the rather broad *d-f* emission and the narrow *f-f* emission lines. Since the parity does not change in such a transition, the life time of the excited state is long and situated in the microsecond range.

The *f-f* emission of Er^{3+} ion following selective *f-d* and *f-f* excitation was investigated in this work as well. The emission spectrum of $LiYF_4$:Er(5%) measured at 10 K under excitation with 10.8 eV photons is shown in Figure 4.9. The inset on the right shows the luminescence originating from the $^4S_{3/2}$ and the $^2H_{11/2}$ states to the $^4I_{15/2}$ ground state in more detail. One can easily distinguish the single Stark components of the emission originating from the crystal field splitting (see section 3.2.2). No assignments are given as it is not the aim of the given work and the inset is represented to demonstrate the improved spectral resolution ($\Delta\lambda$ = 0.5 nm), which can be obtained routinely. The assignments of the dominant *f-f* transitions are given in the figure. They are deduced from [Weg98, Cou98, Jay89]. The observed strong transitions are indicated on the energy level scheme in Figure 4.3. The dominant transitions originate from the $^2P_{3/2}$ state, terminating at $^4I_{13/2}$ (402 nm) and at $^4I_{11/2}$ (470 nm), and from the $^4S_{3/2}$ state terminating at the $^4I_{15/2}$ ground state (550 nm). The numbers given in the brackets correspond to the respective main peak values.

4.2 Excitation spectra of $d \rightarrow f$ and $f \rightarrow f$ luminescence of $LiYF_4:Er^{3+}$

Figure 4.10 shows excitation spectra of the most intense line of the $^4S_{3/2} \rightarrow {}^4I_{15/2}$ *f-f* emission at 550 nm (18181 cm^{-1}) and of the spin-forbidden *d-f* band at 165 nm (60600 cm^{-1}). For obvious reasons, the *d-f* emission can only be excited by *f-d* excitations whereas the *f-f* emission can also be excited via *f-f* excitations. The broad background in the excitation spectrum of the *f-f* emission below ~ 6 eV originates from the second order of exciting VUV radiation. In the excitation spectrum of the $^4S_{3/2} \rightarrow {}^4I_{15/2}$ emission, the lowest $4f^{n-1}5d$ HS state at 7.55 eV (energetic position of the zero-phonon line), which is well separated from the LS-state, can be clearly observed.

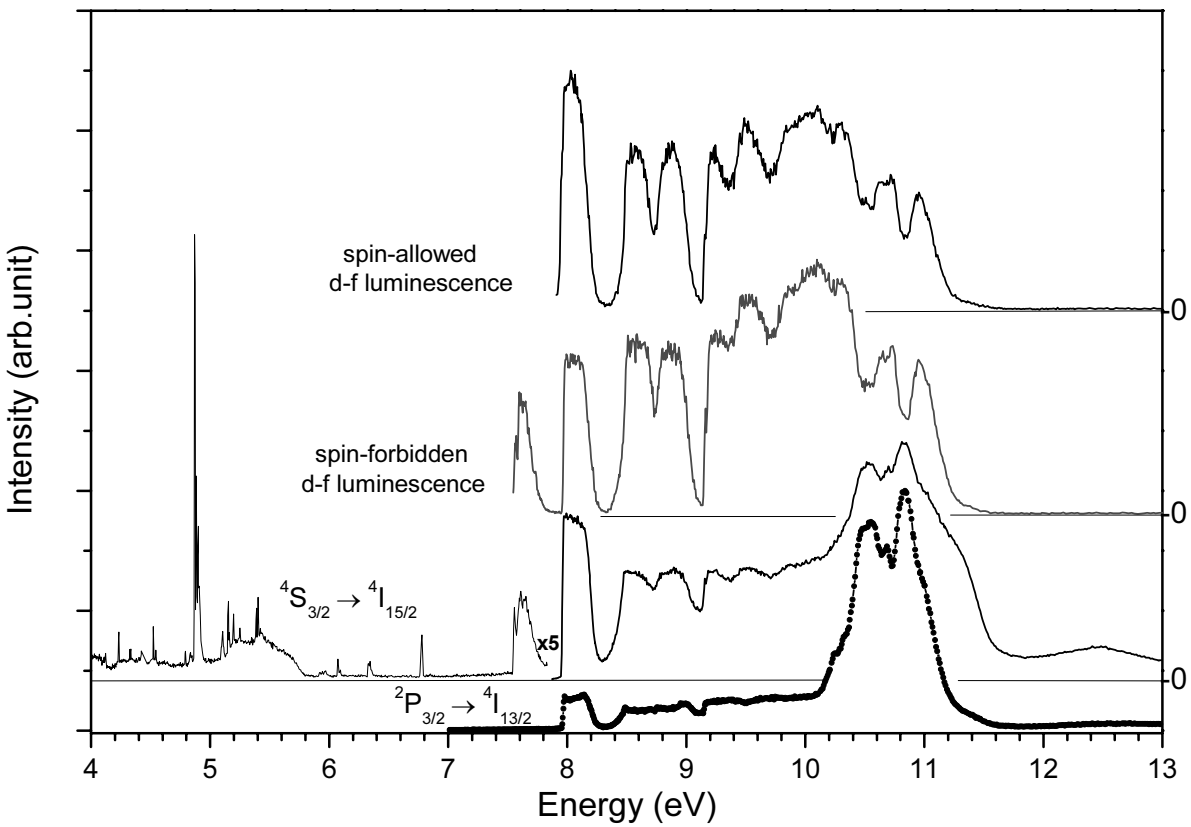

Figure 4.10: *Excitation spectra of selected luminescence bands of $LiYF_4:Er^{3+}$ (1%) measured at T=9 K. The assignments of the selected luminescence bands are given at the curves.*

The absorption of the SA *f-d* transitions to the LS-states is so strong that saturation effects show up [Mel94], resulting in a more or less rectangular shape of the bands. The zero-phonon line is also well defined in the excitation spectrum of the spin-forbidden *d-f* band at 165 nm. In the excitation spectrum of the spin-allowed luminescence (upper curve) the zero-phonon line is not resolved. It can also result from the distortion of the excitation spectra due to the saturation effect. The analogous spectra measured by Wegh et al. [Weg98] and by Pieterson et al. [Pie01] yield much more details.

For comparison purposes, the excitation spectrum of the $^2P_{3/2} \rightarrow {}^4I_{13/2}$ emission at 402 nm is included. There is a striking difference compared to the excitation spectrum of the $^4S_{3/2} \rightarrow {}^4I_{15/2}$ emission. Following selective excitation of the HS state around 7.6 eV, the $^4S_{3/2} \rightarrow {}^4I_{15/2}$ emission shows up, whereas the $^2P_{3/2} \rightarrow {}^4I_{13/2}$ emission is absent (only at room temperature, a slight signal is observed). Note, however, that this statement only holds for low temperatures and for the low Er concentration

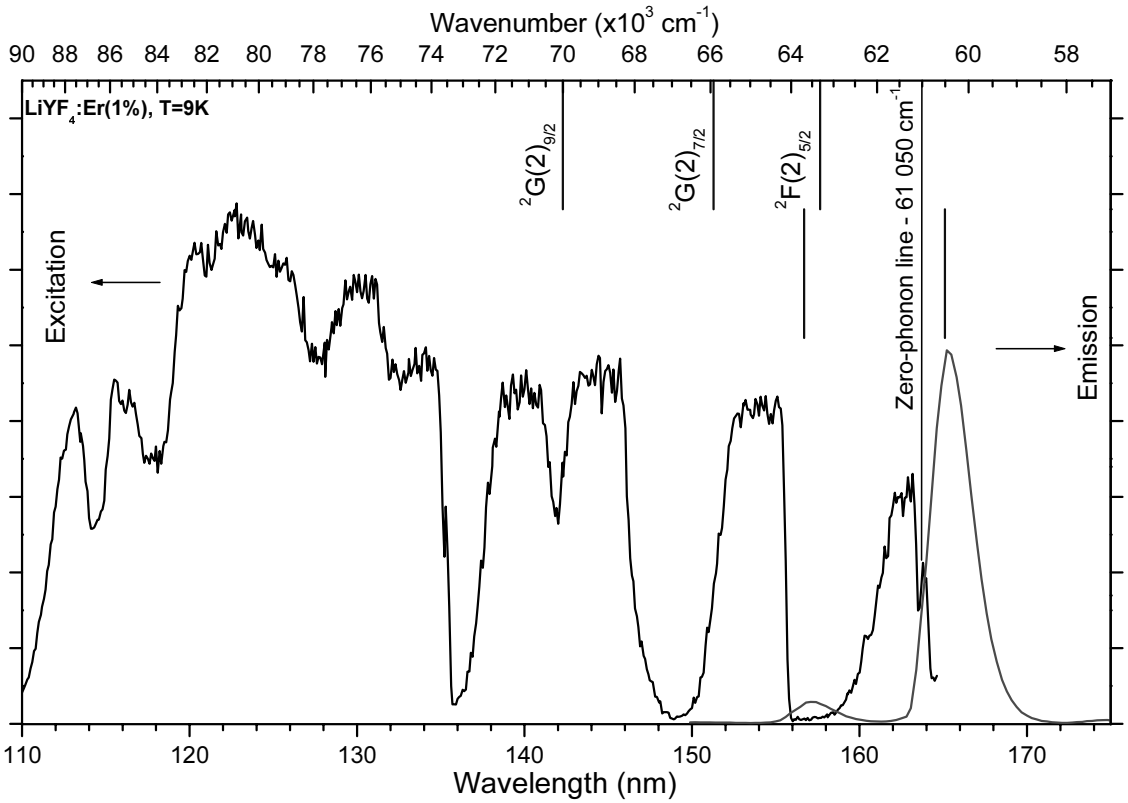

Figure 4.11: *Excitation (left) and emission (right) spectrum of the transition from the high-spin $4f^{10}5d$ state to the $4f^{11}$ground state $^4I_{15/2}$. On the upper part of the figure energy levels the given range is depicted.*

(detailed discussion of the relaxation processes following selective excitation of the HS state is given in section 4.5.1). Between 8 eV and 10 eV, all four excitation spectra shown in Figure 4.10 yield a similar behaviour. Above 10 eV, striking differences are also observed. Maxima in the *f-f* excitation spectra correspond to minima in the *d-f* excitation spectra and vice versa. Moreover, the $^2P_{3/2} \rightarrow {}^4I_{13/2}$ emission is strongly enhanced compared with the $^4S_{3/2} \rightarrow {}^4I_{15/2}$ emission. Above ~11.5 eV in the host absorption range, very different behaviour is observed as well. Both spin-allowed and spin-forbidden *d-f* emissions are practically zero, whereas the $^4S_{3/2} \rightarrow {}^4I_{15/2}$ emission has still considerable intensity.

A closer look to the excitation and emission spectra of the spin-forbidden *d-f* band in the region 140–180 nm is shown in Figure 4.11. It is an important observation that the 157-nm emission is located close to the quartet $4f^{10}5d$ excitation band, shifted

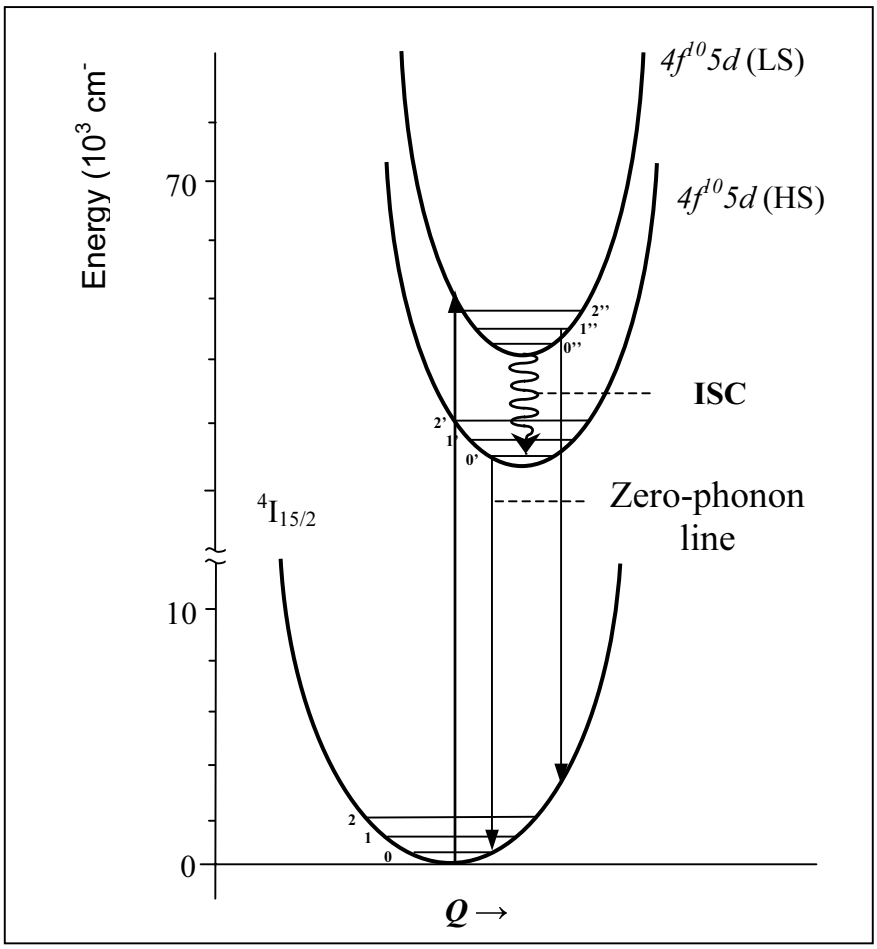

Figure 4.12: *Configurational coordinate diagram for Er^{3+} in $LiYF_4$ illustrating process of excitation and following spin-allowed and spin-forbidden (in this instance zero-phonon line) transitions.*

some 1000 cm^{-1} to lower energy. This Stokes shift is similar to the Stokes shift for the emission band at 165 nm. This fact confirms that the emission band peaking at 165 nm originates from the sextet (HS) $4f^{10}5d$ state. Moreover, the presence of the zero-phonon line (61050 cm^{-3}) in the excitation spectrum indicates intermediate electron-phonon coupling in the given system and the position of the zero-phonon line corresponds to the exact position of the $4f^{10}5d$ HS state. The zero-phonon line in the emission spectrum was not observed, probably because of the insufficient resolution of the VUV monochromator.

The above discussed situation is depicted in the configurational coordinate diagram in Figure 4.12. Upon the excitation to LS $4f^{10}5d$ state of Er^{3+} in $LiYF_4$, either fast spin-allowed emission from the quartet $4f^{10}5d$ state occurs or intersystem crossing (ISC) occurs, which populates the sextet $4f^{10}5d$ state. From this state slow spin-forbidden emission can be expected. Based on the relative intensities of the spin-allowed and spin-forbidden emission bands, the probability for intersystem crossing is estimated to be about ten times higher than the radiative decay from the quartet $4f^{10}5d$ state (see section 4.3.2).

4.2.1 Excitation of the *d-f* luminescence via host absorption

If the photon energy is high enough to be absorbed by the host crystal, the peculiarities in the excitation spectra of various emissions can be expected. It is known that the quantum yield of Er^{3+} *d-f* luminescence is extremely low in the region of fundamental absorption of the matrix ($h\nu > 12$ eV). The generation of the excitons and electron-hole pairs does not lead to the efficient excitation of the *d-f* luminescence. Moreover it has been shown by Makhov *et al.* [Mak00] that above the certain onset ($h\nu > 20.5$ eV) in the region of the fundamental absorption of $LiYF_4$, a considerable increase of the *d-f* emission occurs again. The threshold was ascribed to the excitation of Er^{3+} ion into *d*-states by photoelectrons with sufficiently high kinetic energy, $E_{th} \approx E_g+E_0$ (E_0: energy of the lowest Er^{3+} LS d-excitation). The obtained results show clearly (Figure 4.13) that the efficiency of the energy transfer from the matrix to Er^{3+} *d-f* luminescence in $LiYF_4:Er^{3+}$ is extremely low in the region of

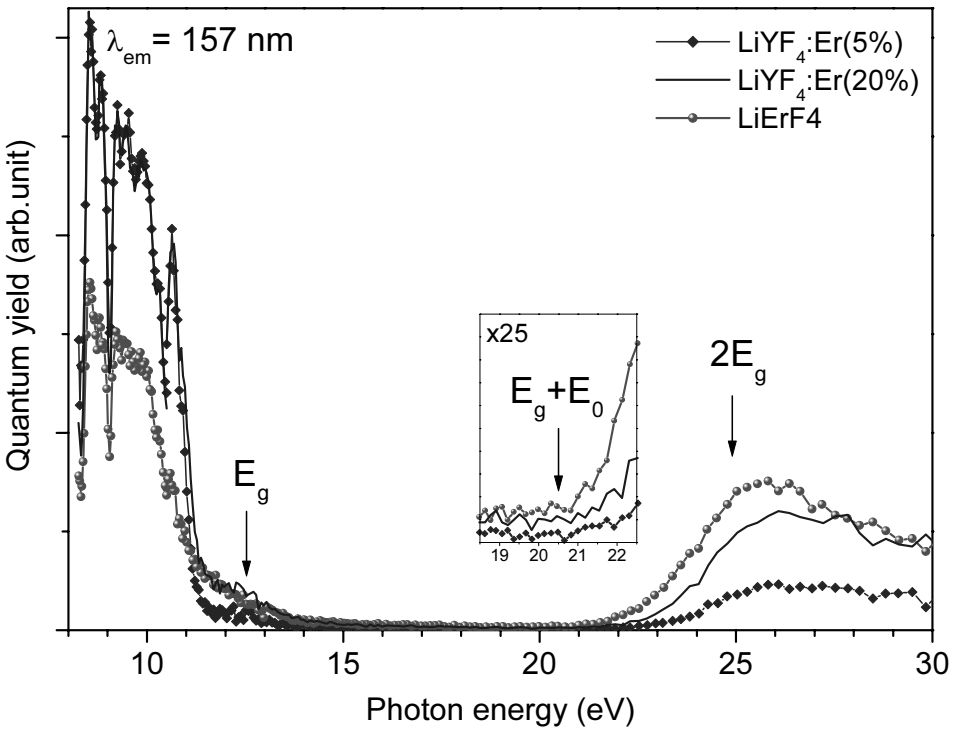

Figure 4.13: *Excitation spectra of the spin-allowed 5d-4f luminescence for $LiYF_4:Er^{3+}$(5%), $LiYF_4:Er^{3+}$(20%) and $LiErF_4$ at 300 K. E_g is the band-gap for $LiYF_4$; E_0 is the onset for the 4f-5d absorption of Er^{3+} in $LiYF_4$.*

fundamental absorption of the crystal until the excitation energy reaches the threshold for processes of multiplication of electronic excitations [Mak00]. The experimental value of the threshold is ~20.5 eV (see enlarged inset in Figure 4.13). From the threshold energy described above, subtracting the respective value for E_0 (E_0 ≈ 8.1 eV), an experimental estimate of the band-gap energy for $LiYF_4$ can be done resulting in $E_g \approx 12.4$ eV. As it is seen in Figure 4.13, this threshold lies in $LiYF_4:Er^{3+}$ crystals at photon energy less than $2E_g$, and the effect is much more pronounced at higher concentration of Er^{3+}. These features indicate that the excitation mechanism of the Er^{3+} *d-f* luminescence in $LiYF_4:Er^{3+}$ is so-called impact mechanism of multiplication of electronic excitations [Lus96, Kir96] when fast photoelectrons excite directly (by impact) emission centres (Er^{3+} ions) in the crystal. Since this mechanism is more efficient at higher concentrations of the emission centres, the impact excitation results in relatively high quantum yield and fast decay of Er^{3+} *d-f* luminescence in highly doped (in particular, in stoichiometric) crystals at high energy excitation (>20.5 eV) despite of the effect of concentration quenching reducing the

luminescence intensity. From view point of scintillator applications, such crystals can be considered as promising fast VUV scintillators with short wavelength edge of the spectrum at about 157 nm.

4.2.2 Excitation of *f-f* luminescence, intrinsic and extrinsic host emission

For an analysis of the data, the ratios of excitation spectra for different emission lines are useful. Such a procedure allows to see some peculiarities which are not obvious from the individual spectra. Figure 4.14 shows the ratio of the $^2P_{3/2} \rightarrow ^4I_{13/2}$ emission at 402 nm and the spin-allowed *d-f* band at 157 nm. In addition to

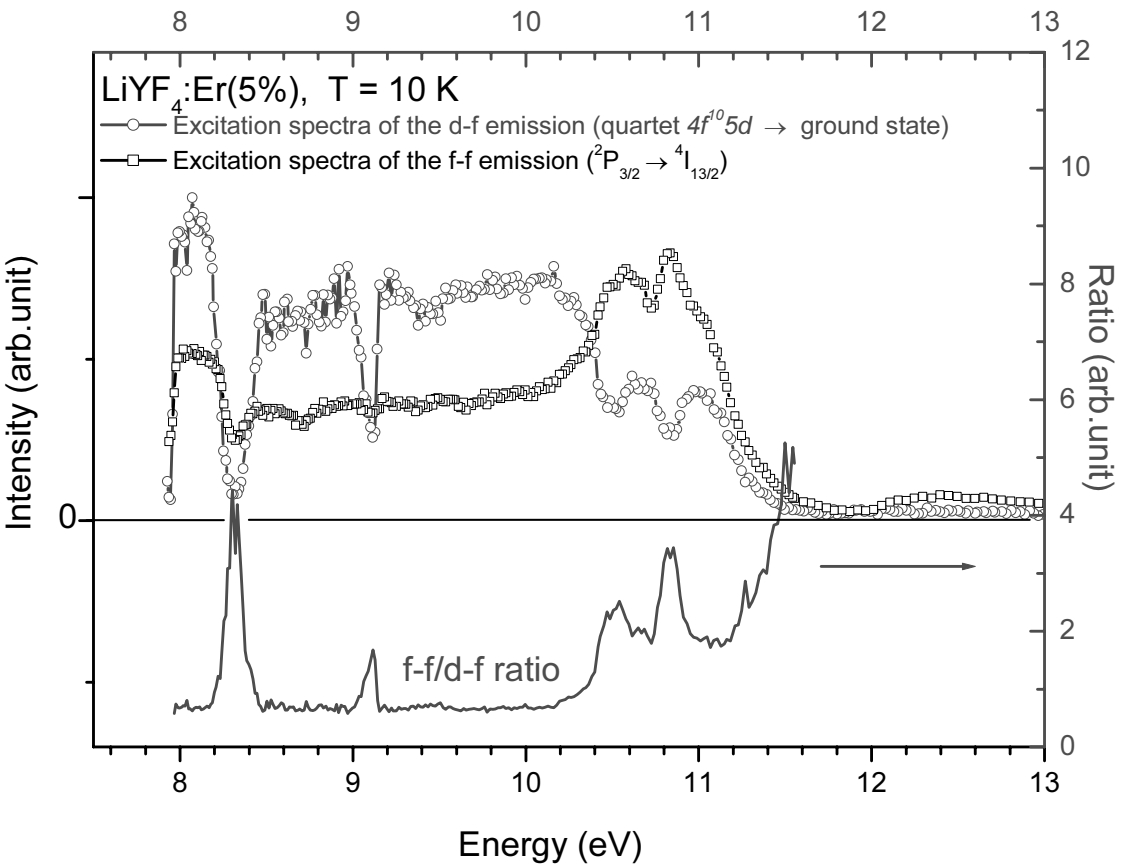

Figure 4.14: *Ratio between the excitation spectra of f-f luminescence, represented by the transition from the $^2P_{3/2}$ to $^4I_{13/2}$ state, and excitation spectra of d-f luminescence, represented by the transition from the quartet $4f^{10}5d$ state to the ground state for $LiYF_4:Er^{3+}$ (5%) at T=10 K; the respective curves are given on top.*

the already mentioned feature concerning complementary behaviour of the spectra in the range from 10 eV to 11 eV, the strong peaks at ~8.3 eV and ~9.1 eV become evident. Moreover the increasing ratio shows that the host sensitisation of the *f-f* emission is more efficient than of the *d-f* emission in the region of fundamental absorption of the matrix ($h\nu > 11$ eV).

The presence of two peaks in the 8-10 eV interval in the ratio curve can be explained by the gaps in the *f-d* absorption (see excitation spectrum of the *d-f* emission in Figures 4.14, 4.15a). At the same time, excitation spectra of the *f-f* luminescence have still considerable intensity in this range. To explain such behaviour the investigation of nominally pure $LiYF_4$ is helpful.

4.2.2.1 Investigation of the undoped $LiYF_4$ system

To clarify the influence of the host matrix itself on the electronic relaxation in the $LiYF_4$:Er system, a certain amount of measurements was performed in the nominally pure $LiYF_4$.

The inset in Figure 4.15b demonstrates two emission spectra of undoped YLF exited by 10.78 and 12.41 eV photons at T=8 K (curves 2' and 1' respectively). The first excitation energy corresponds to the absorption in the Urbach tail of $LiYF_4$. Due to the still relatively small absorption coefficient (see curve 1 in Figure 4.15c) the centres of the extrinsic origin, namely impurities and/or defects are excited as well. Therefore, in the transparency range the broad extrinsic emission in the nominally pure $LiYF_4$ crystal (curve 2' in Figure 4.15b) is efficiently excited in the 6-10 eV energy range (see excitation curve 2). This broad band emission with a maximum at 450 nm can transfer its energy to the *f-f* transitions. In this way the efficiency of the *f-f* excitation increases and two first peaks in the ratio spectrum in Figure 4.14 arise.

The STE emission in $LiYF_4$ has been identified by Hayes *et al.* [Hay80] at 300 nm. The maximum in the emission spectrum of pure YLF crystal investigated in this work is located at 340 nm (curve 1' in Figure 4.15b). This discrepancy is partly due to the fact that the emission spectrum is not corrected for the transmission of the spectrograph-CCD system. Moreover, it is not excluded that, like in other fluorides, there are either several kinds of excitons in different configurations or perturbed

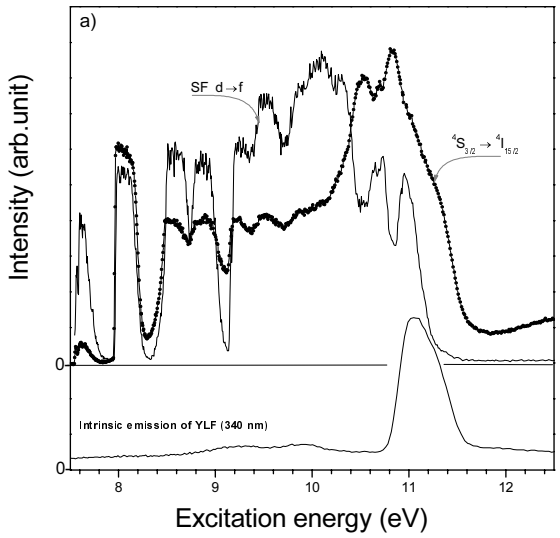

Figure 4.15: *a) Excitation spectra monitoring the $^4S_{3/2} \rightarrow {}^4I_{15/2}$ and spin-forbidden d-f luminescence in $LiYF_4:Er^{3+}$(5%), measured at T=10 K. For comparison, the excitation spectrum monitoring emission peaking at 340 nm (lowest curve) in the undoped $LiYF_4$ is shown.*

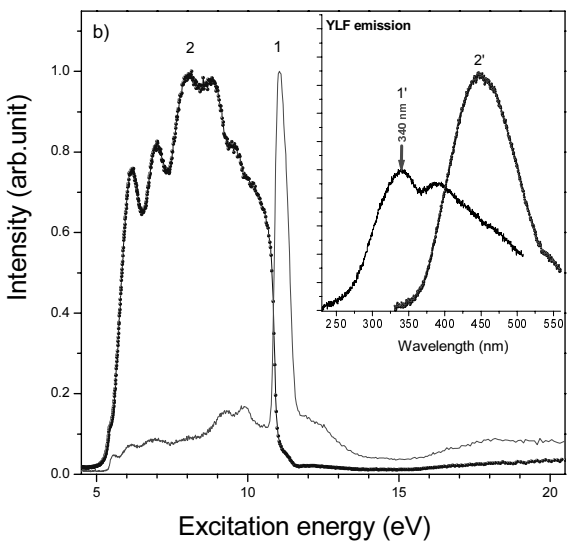

b) Excitation spectra monitoring the intrinsic emission (curve 1) and extrinsic emission peaking at 450 nm (curve 2) measured in the pure $LiYF_4$ at T=8 K. The respective emission spectra are shown in the inset (curves 1' and 2' excited at 12.41 eV and 10.78 eV respectively). Emission curves are not corrected for the apparatus function of the detection system.

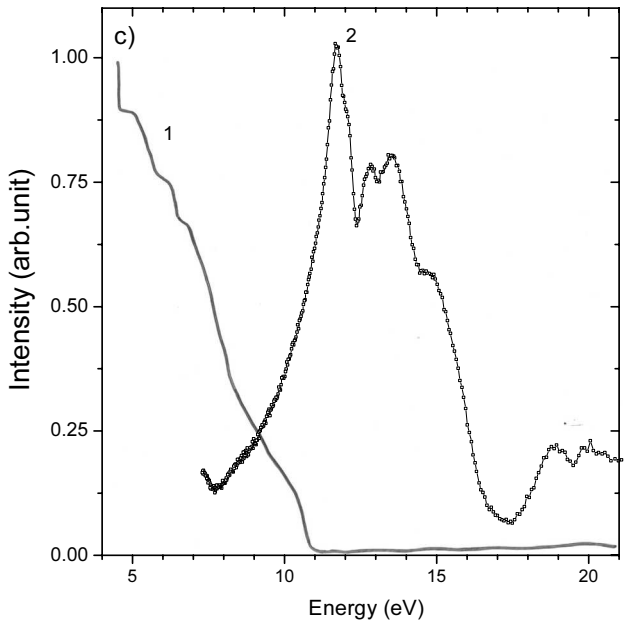

c) Transmission spectrum of $LiYF_4$ at T=300 K (curve 1, measured by E. Schultheiss, Giessen Physikalisches Institut, 1986) and reflection spectrum of $LiYF_4:Er^{3+}$(5%) measured at T=10 K (curve 2).

excitons formed near defect. The peak at 11.04 eV in the excitation spectrum of the 340 nm emission (see curve 1 in Figure 4.15b) corresponds, possibly, to the formation of anionic Frenkel's defect, the emission of which is shifted to the higher wavelength from the STE emission.

As the STE recombination energy is not sufficient to excite *d*-levels of the Er^{3+} the STE can transfer its energy to the *4f* level resulting in appearance of the *f-f* emission. The comparison of the excitation spectra monitoring SF *d-f*, $^4S_{3/2} \rightarrow {}^4I_{15/2}$ and STE emissions in Figure 4.15a confirms that excitonic energy transfer is one of the population channels for the *f*-levels (appears like a shoulder in the respective excitation curve between 11 eV and 11.8 eV). Moreover, before self-trapping, the free exciton can migrate through the crystal (within the range from few to thousands lattice constant, depending on the host matrix) and transfer its energy, which in this case is sufficient to excite *d*-states of Er^{3+} ion, directly to the luminescence centre. So, the peak at 10.95 eV in the excitation spectrum of the *d-f* emission is ascribed to excitonic energy transfer.

Coming back to the doped system, in the reflection spectrum of $LiYF_4:Er^{3+}$(5%) (curve 2 in Figure 4.15c) a pronounced peak at 11.65 eV is detected. This maximum in the reflection spectrum is ascribed to the excitonic peak in analogy to other wide band gap fluorides (e.g. LiF). Taking into account the earlier deduced energy gap value E_g=12.4 eV the binding energy is estimated to be 0.75 eV.

4.2.2.2 Charge transfer excitation and autoionization processes

The competition between *f-f* and *d-f* emissions excited between 10 eV and 11.0 eV, resulting in additional peaks in the *f-f*/*d-f* ratio spectrum in Figure 4.14, is more complicated for interpretation. The charge transfer excitations of the type $F^- \rightarrow Er^{3+}$ can play also a role. The energetic positions of such transitions for fluoride crystals were recently discussed by Belsky and Krupa [Bel99]. For Er^{3+}, the energy of the charge transfer transitions is calculated to be about 10.5 eV (see Chapter 3.8). However, the charge transfer bands observed for others RE ions (e.g. Eu^{3+}) are typically broad and featureless. But this does not exclude that the charge transfer absorption independently of other processes contributes to the excitation mechanisms of the *f*-levels in the discussed energy range.

So called autoionisation states can also contribute in the competition between *f-f* and *d-f* emissions. In the combined system of host plus rare earth impurity, the *f-d* transition can promote one electron from the ground state to the excited *5d*-states located in the conduction band of the host. In case of a strong coupling between these states and the continuum of the solid, the electron can be completely delocalised in the conduction band and the consecutive autoionisation process gives rise to $Ln^{4+} + e^-$

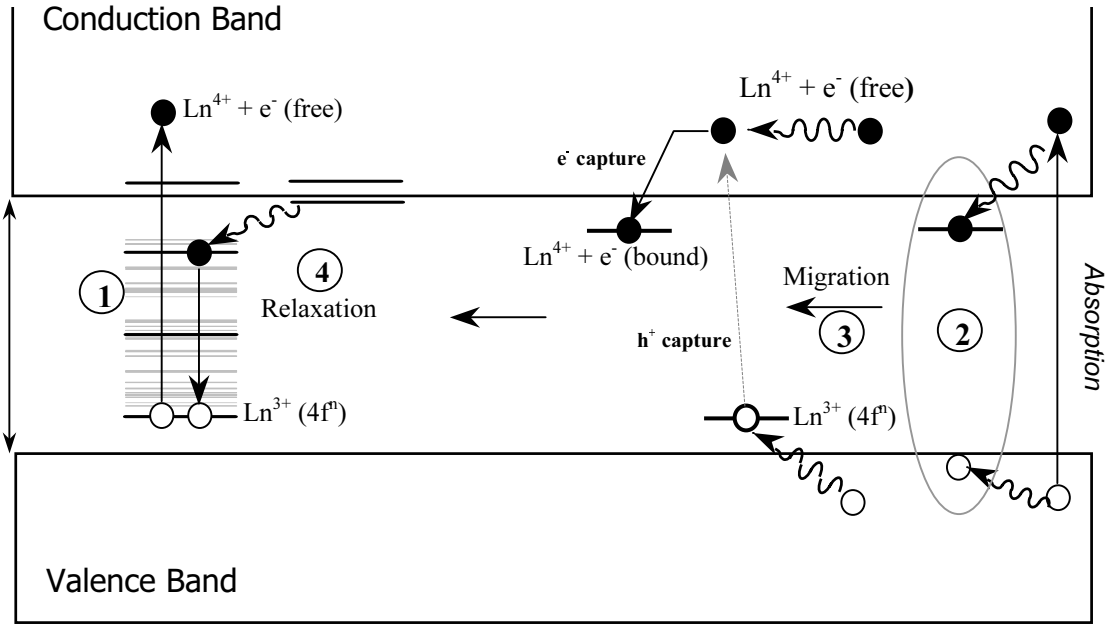

Figure 4.16: *Energy scheme of exciton and free charge carrier recombination on rare earth ion involving autoionisation states.*

(free) state (process 1 in Figure 4.16). Then, the capture of the free-electron can be interpreted in the model of the exciton trapped on the impurity center as $Ln^{4+} + e^-$ (bounded) state and the emitted energy during the process as the excess of the exciton recombination energy [McC98, Bel99] (processes 2, 3, 4 in Figure 4.16).

The propensity of the rare earth ion to give up one electron should be regarded as its hole acceptor capability. It means that these ions embedded in a solid will develop a more or less intense short range potential for hole attraction depending on the stabilisation energy of the 4^+ charge state [McC98, Bel99].

In order to locate the position of the autoionization state the knowledge of the energetic position of the *4f* ground state relative to the valence band of the host matrix is required. Recent photoemission and two step photoconductivity experiments [Thi01, Jia02, Yen03] shows that in oxides the ground state of Er^{3+} is situated below the top of the host valence band (YAG:Er - –3.3 eV, Y_2O_3:Er - –1.0 eV, Gd_2O_3 - –0.7 eV). Unfortunately, information about the position of the *4f* ground state of Er^{3+} in fluorides is not available. Therefore, one can only speculate that the autoionization states, which relax preponderantly to the *f*-states when populated, contribute to the excitation mechanisms of the *f-f* emission between 10 eV and 11 eV.

4.2.3 Soft X-ray excitation

Additionally an attempt was made to investigate electronic relaxation in $LiYF_4$:Er system under primary excitation far up into the conduction band (see Appendix B). The excitation spectra of *d-f* and *f-f* emission in the *soft x-ray* range between 50 eV and 200 eV are shown in Figure 4.17. The spectral analysis of the luminescence was performed with a VUV monochromator optimized for the range of the *d-f* emissions. The longer-wavelength *f-f* transitions ($\lambda > 500$ nm) are out of the working range of the respective instrument, therefore, the $^2P_{3/2} \rightarrow {}^4I_{13/2}$ had to be chosen as a representative of *f-f* emissions. The spectral range covers the Li K-, Y M_{45}-, and the Y N_1-edges. The spectra do not show pronounced structures because the respective core excitations into the bottom of the conduction band are parity forbidden [Chi01]. Dividing both spectra results in a more or less straight line indicating that the branching between *d-f* and *f-f* emission does not depend on photon energy of excitation in the soft x-ray region. The tendency of increase towards smaller photon energies of excitation is in agreement with the fact that the *d-f* emission itself will go to zero, whereas the *f-f* emission will reach a finite level below the threshold of inelastic scattering ($h\nu < 20$ eV).

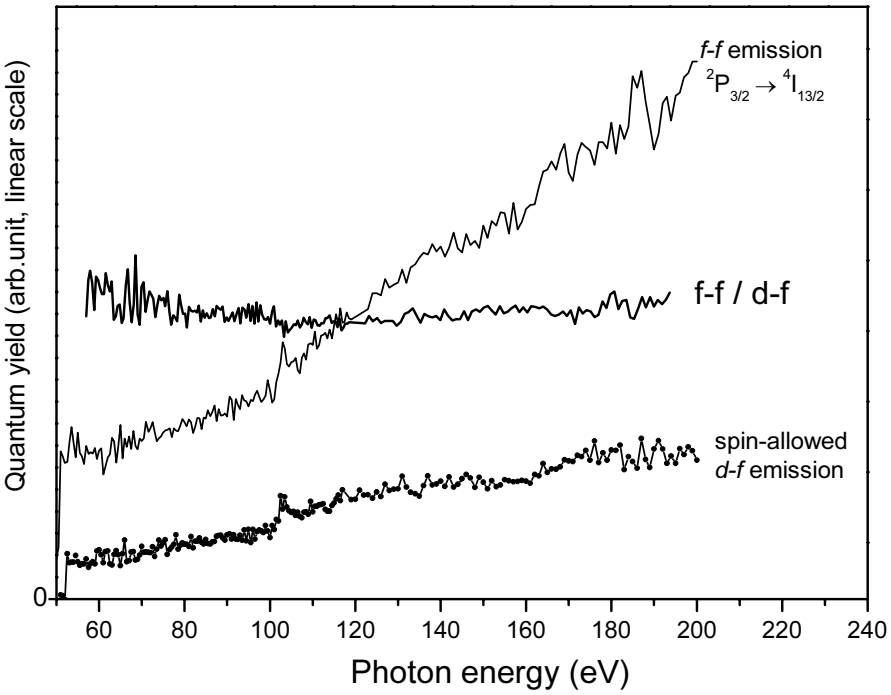

Figure 4.17: *Luminescence excitation spectra of the spin-allowed d-f emission and one of the f-f emissions of $LiYF_4:Er^{3+}$ (5%) at T=10 K in the soft x-ray region. The ratio of both curves is included as well.*

The energy transfer to the *f*-levels takes place mainly via relaxation of intrinsic excitations (STE, electron-hole pairs) while the excitation of *d-f* emissions is tentatively assigned to the impact excitation mechanism. All hot electrons of different origins (photo excitation, Auger processes) with energies above ~8 eV can excite the Er^{3+} ions from the ground state into the *d*-levels.

4.3 Branching of absorbed energy

Energy relaxation of the Er^{3+} ion in $LiYF_4$ strongly depends on several parameters such as temperature, doping concentration and initially excited state. The character of these dependencies was revealed through series of experiments in which the above mentioned parameters were varied. The results are represented in the following section.

4.3.1 Initially excited state

In Figure 4.18, *f-f* luminescence spectra are shown for different excitation energies (T = 8 K, Er^{3+} doping concentration is 1 %). The excitation energies hν = 8 eV and 7.6 eV correspond to the lowest $4f^{10}5d$ LS and HS states. The most interesting aspect is the gradual redistribution between the $^2P_{3/2}$ (402 nm) and the $^4S_{3/2}$ (550 nm) emission for primary excitation *above* the lowest HS state. The intra-configurational transition $^2P_{3/2} \rightarrow {}^4I_{13/2}$ is the most intense emission line in case of excitation into levels lying sufficiently higher than quartet $4f^{10}5d$. With decreasing excitation energy, the intensity of this emission decreases as well. Under primary excitation into the lowest HS state itself, the intensity of the $^2P_{3/2}$ emission becomes very low. Further decrease of excitation energy yields no remarkable changes in the emission spectra until photon energies of primary excitation reach the value of 5.4 eV, which corresponds to $^2I_{13/2}$. Then the $^2P_{3/2}$ emission band reappears again after excitation in low lying $4f^n$ states (see curve measured under 4.86 eV excitation). This feature actually indicates the presence of other channels of relaxation for excitation photon energies in the interval from ~5.4 to ~8 eV.

4.3.2 Doping concentration

With increasing doping concentration, the possibility must be taken into account that two optically active centres are sufficiently close to each other to interact. This interaction may be too weak to have a detectable effect on the energy levels so that the centres retain their individual identities but may yet be sufficiently strong to

enable excitation to be transferred from one ion to another. The occurrence of energy transfer between centres can significantly affect the luminescence properties of a material.

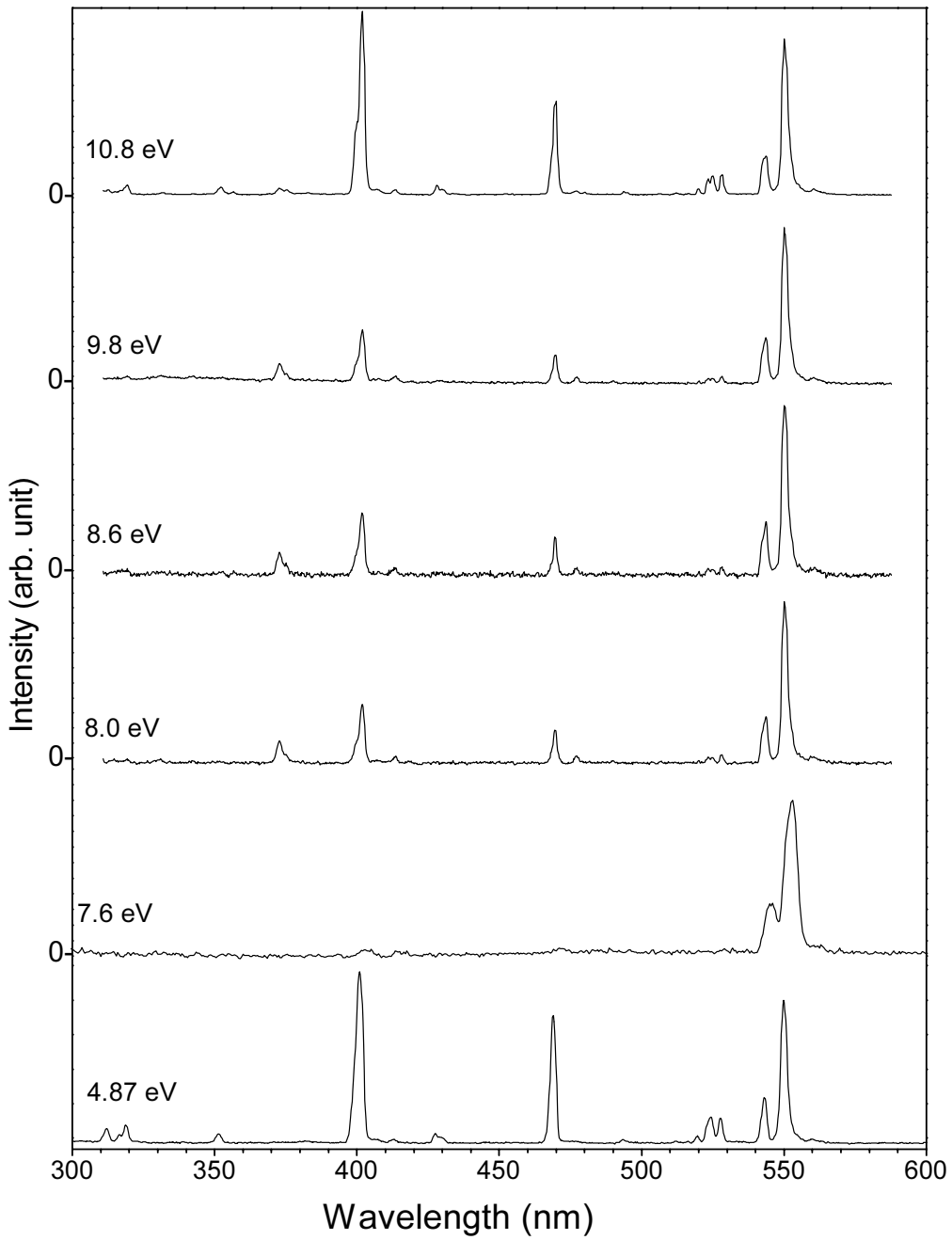

Figure 4.18: *Luminescence spectra of $LiYF_4:Er^{3+}$ (1%) at 8 K for different photon energies of excitation. All curves are normalized at the maximum of the $^4S_{3/2} \rightarrow {}^4I_{15/2}$ transition peaking at 550 nm. The photon energies of excitation are given at the curves.*

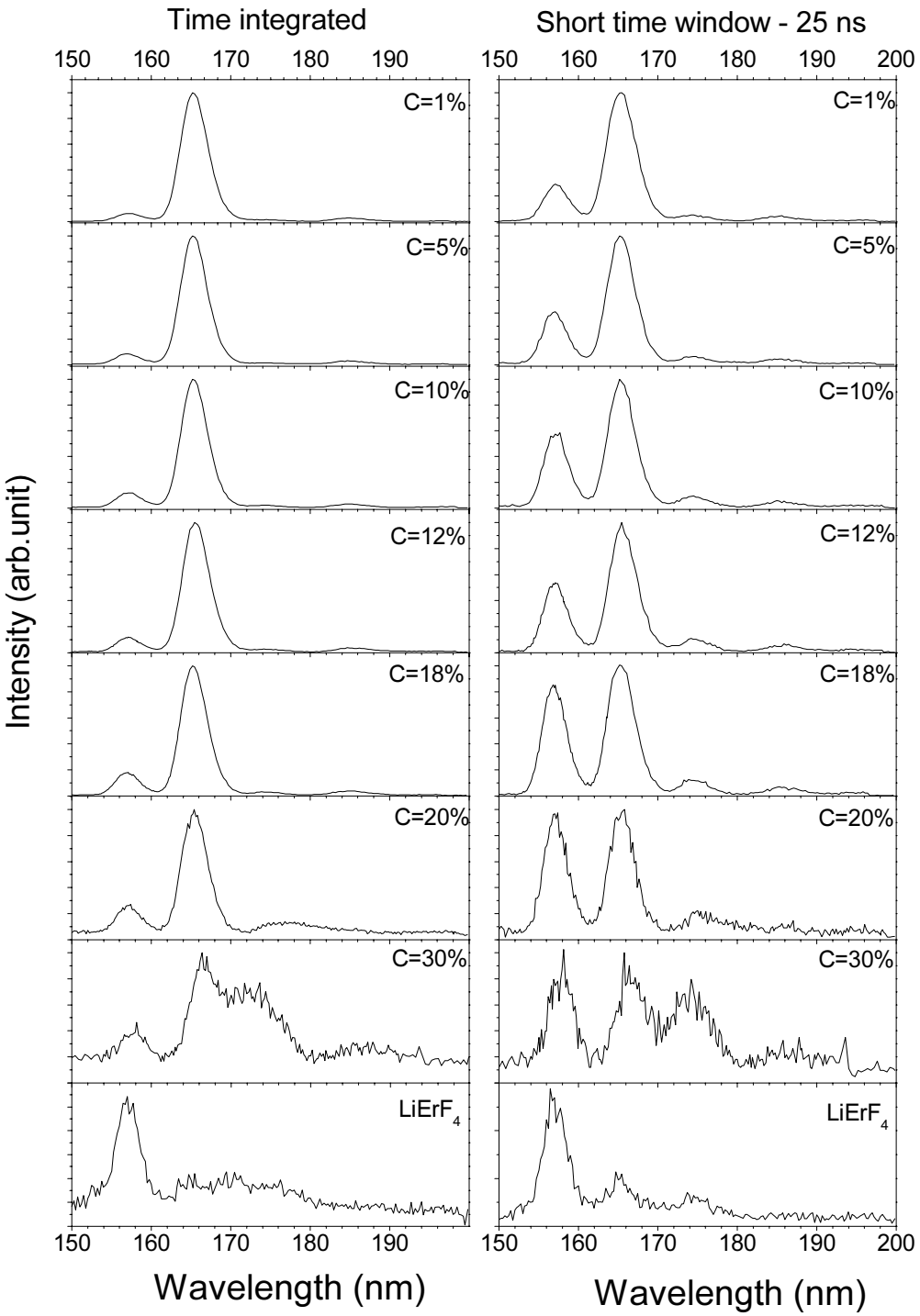

Figure 4.19: *Luminescence of $LiYF_4:Er^{3+}$ as a function of Er^{3+} concentration excited by 10.8 eV photons at T=296 K and measured in two time windows: time-integrated (left) and short, from 0 to 25ns, time window (right). All spectra are normalized to the most intense band originating from spin-forbidden d-f emission peaking at 165.2 nm.*

A set of VUV emission spectra for different concentrations is shown in Figure 4.19. The spectra were measured at T = 296 K under excitation above quartet $4f^{10}5d$. The concentration was varied from 1% to 100% (stochiometric crystal). The time-integrated spectra as well as time-resolved ones were recorded.

Time integrated spectra (left part) were collected during the full period between excitation pulses. Spectra shown on the right part of the figure were collected during the first 25 ns after the excitation pulses. Due to the fact that spin-allowed *d-f* luminescence is fast with a decay time in the nanosecond range, in the short time window mainly transitions from the quartet $4f^{10}5d$ state are monitored. Nevertheless, the dominant peak of the corresponding curves arises from the spin-forbidden transition from the HS $4f^{10}5d$ state to the ground state due to the temporal overlap of

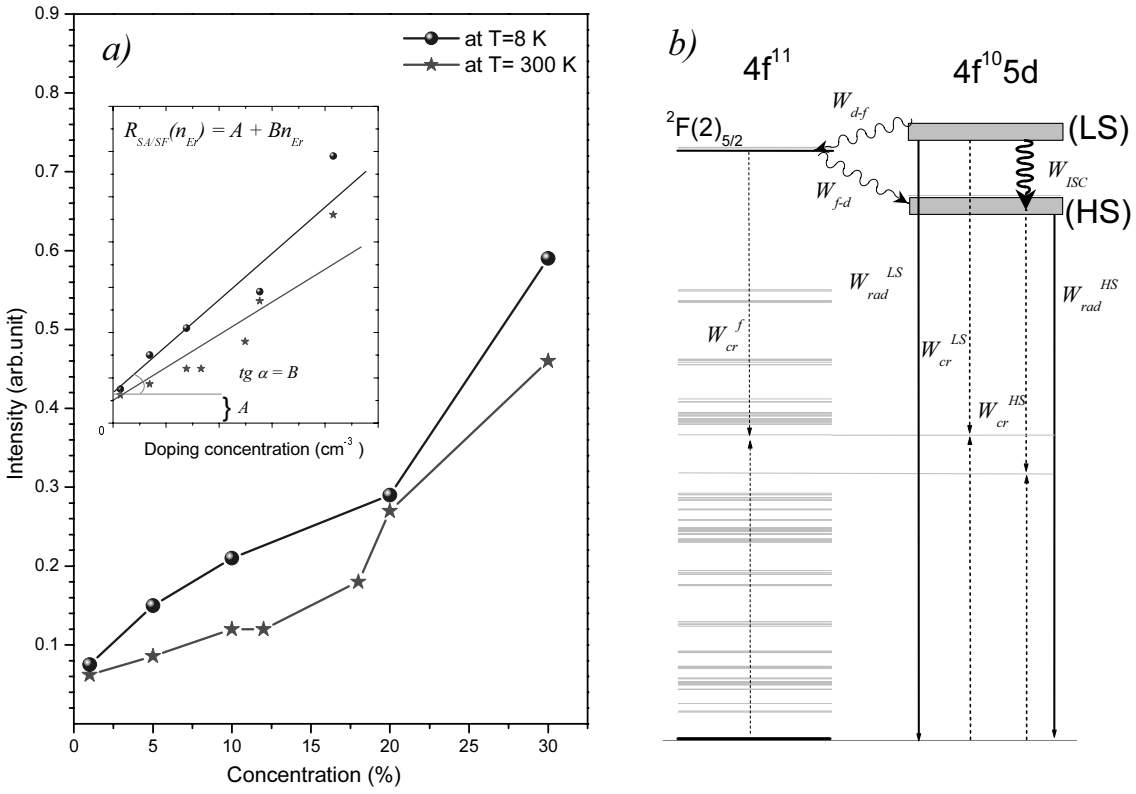

Figure 4.20: *a) Relative intensity of the spin-allowed $4f^{10}5d$ emission as a function of concentration at T=8 K and at room temperature. Emission band areas were measured to calculate the ratio $R_{SA/SF}$. The inset demonstrates linear fit of the respective data; b) simplified schematic energy level diagram for Er^{3+} in $LiYF_4$ showing various relaxation processes after f-d excitation.*

both components. Since the luminescence yield decreases with increasing doping concentration, the time interval 25 ns was chosen to get reasonable intensity in highly concentrated system (compare with Figure 4.4). As one can see from Figure 4.19, raising the concentration leads to a considerable increase in the relative intensity of the spin-allowed emission in spite of the fact that absolute intensity decreases.

Relative intensity of the spin-allowed emission (relative with the respect to the intensity of the SF luminescence) deduced from Figure 4.19 as a function of concentration is shown in Figure 4.20a. At T=8 K the relative intensity of the SA luminescence increases faster with increasing the concentration than at room temperature. This fact can be explained by the presence of the non-radiative transfers from LS to HS state depopulating quartet $4f^{10}5d$ (see Figure 4.20 (b)) that are more efficient at higher temperature.

In addition, one can write a set of the rate equations for the model depicted in Figure 4.20 (b) after excitation into the LS state:

$$\frac{dN_{LS}}{dt} = N_{pump} - N_{LS}(W_{rad}^{LS} + W_{ISC} + W_{d-f} + W_{cr}^{LS}) \tag{4.3}$$

$$\frac{dN_{f}}{dt} = N_{LS}W_{d-f} - N_{f}(W_{rad}^{f} + W_{f-d} + W_{cr}^{f}) \tag{4.4}$$

$$\frac{dN_{HS}}{dt} = N_{LS}W_{ISC} + N_{f}W_{f-d} - N_{HS}(W_{rad}^{HS} + W_{cr}^{HS}) \tag{4.5}$$

where N_{LS}, N_{HS}, N_f are populations of the $4f^{10}5d$ LS, $4f^{10}5d$ HS and $^2F(2)_{5/2}$ states respectively. W_{ISC}, $W_{d\text{-}f}$, $W_{f\text{-}d}$ and W_{rad} describe probabilities of the respective processes as it shown in Figure 4.20 (b). W_{cr}^{LS}, W_{cr}^{HS}, W_{cr}^{f} describe probabilities of the cross-relaxation processes starting from $4f^{10}5d$ LS, $4f^{10}5d$ HS or $^2F(2)_{5/2}$ states respectively. Moreover, W_{cr} are concentration dependent parameters which in common case can be written as $W_{cr}=k\cdot n_{Er}$, where k is a constant and n_{Er} is the concentration of the Er^{3+} ions. In addition, as it was shown in section 4.1.1.2, depopulation of the HS state can occur non-radiavely through the LS state (thermal quenching). As this quenching process requires enhanced temperatures it is omitted here.

Some remarks concerning $^2F(2)_{5/2}$ state should be made. Radiative *f-f* transitions starting from $^2F(2)_{5/2}$ also take place (detailed discussion of the respective bands is given in [Weg98]), but the luminescence intensity of this transitions are so

low, in comparison with the SA *d-f* emission, that it can be neglected *i.e.* $W_{rad}^{f} \equiv 0$. The gap between $^2F(2)_{5/2}$ and the next low-lying $4f^{11}$ state is ~ 8000 cm^{-1} thus the corresponding non-radiative transfer is unexpected. In case of the constant pumping ($dN/dt \equiv 0$):

$$N_f = \frac{N_{LS} W_{d-f}}{W_{f-d} + W_{cr}^{f}} \tag{4.4'}$$

$$N_{HS} = \frac{N_{LS} W_{ISC} + N_f W_{f-d}}{W_{rad}^{HS} + W_{cr}^{HS}}. \tag{4.5'}$$

The intensity of emission can be written as $I(t) \propto N(t) \cdot W_{rad}$, then for SA and SF emission, taking into account (4.4') and (4.5'), one can write:

$$I_{SA} = N_{LS} \cdot W_{rad}^{LS} \tag{4.6}$$

$$I_{SF} = N_{HS} \cdot W_{rad}^{HS} = N_{LS} \cdot \frac{W_{ISC} + \dfrac{W_{d-f} W_{f-d}}{W_{f-d} + W_{cr}^{f}}}{W_{rad}^{HS} + W_{cr}^{HS}} \cdot W_{rad}^{HS}. \tag{4.7}$$

The intensity ratio $R_{SA/SF}$ (or relative intensity of SA luminescence) can be written as:

$$R_{SA/SF} = \frac{I_{SA}}{I_{SF}} = \frac{W_{rad}^{LS}}{W_{ISC} + \dfrac{W_{d-f} \cdot W_{f-d}}{W_{f-d} + W_{cr}^{f}}} + \frac{W_{cr}^{HS}}{\dfrac{W_{rad}^{HS}}{W_{rad}^{LS}} \cdot \left(W_{ISC} + \dfrac{W_{d-f} W_{f-d}}{W_{f-d} + W_{cr}^{f}} \right)} \tag{4.8}$$

The appearance of the cross-relaxation starting from the LS and HS $4f^{10}5d$ states is evident from the decay time measurements discussed in section 4.4 and 4.5.2 (the increase of the doping concentration leads to the decay kinetics shortening). The lack of the experimental evidences for the presence of the cross-relaxation process starting from the $^2F(2)_{5/2}$ state allows to assume $W_{cr}^{f} \equiv 0$. In this case, taking into consideration that $W_{cr}^{HS} = k_{HS} \cdot n_{Er}$, the intensity ratio $R_{SA/SF}$ takes the form

$$R_{SA/SF} = \frac{W_{rad}^{LS}}{W_{ISC} + W_{d-f}} + \frac{W_{rad}^{LS}}{W_{rad}^{HS}} \cdot \frac{k_{HS}}{W_{ISC} + W_{d-f}} \cdot n_{Er} \tag{4.8'}$$

The linear fit of the respective data as it is shown in Figure 4.20a results in values for parameters $A = 0.073$ and $B = 1.4 \cdot 10^{-22}$ cm^3, where

$$A = \frac{W_{rad}^{LS}}{W_{ISC} + W_{d-f}} \tag{4.9}$$

and

$$B = \frac{W_{rad}^{LS}}{W_{rad}^{HS}} \cdot \frac{k_{HS}}{W_{ISC} + W_{d-f}} = A \cdot \frac{k_{HS}}{W_{rad}^{HS}} \tag{4.10}$$

The analysis of the decay kinetic measurements performed for the spin-forbidden *d-f* emission as it is described in the section 4.5.2 yields for the ratio $\frac{k_{HS}}{W_{rad}^{HS}}$ the value of $3.67 \cdot 10^{-21}$ cm^3 (the same ratio resulting from the relation (4.10) is equal to $1.93 \cdot 10^{-21}$ cm^3). This fact confirms at least that two independent from each other models concerning intensity and decay time measurements are producing consistent results.

The radiative decay time of the spin-allowed *d-f* emission τ_0 was also estimated from the decay kinetic measurements (see section 4.4). In that case calculated $1/\tau_0$ contains as regular constituents W_{ISC} and W_{d-f}, *i.e.*

$$\frac{1}{\tau_0} = W_{rad}^{LS} + W_{ISC} + W_{d-f} \tag{4.11}$$

By solving together (4.9) and (4.11) the following values can be calculated:

$$W_{rad}^{LS} = \frac{1}{\tau_0} \cdot \frac{1}{1 + 1/A} = 1.19 \cdot 10^7 \text{ s}^{-1} \tag{4.12}$$

and

$$W_{ISC} + W_{d-f} = \frac{1}{\tau_0} \cdot \frac{1}{1 + A} = 1.63 \cdot 10^8 \text{ s}^{-1} \tag{4.13}$$

Here very similar results obtained by Wegh [Weg98] for $LiYF_4$:Er(2%) single crystal at T=10 K can be mentioned. A simple empirical model was assumed. From the LS $4f^{10}5d$ state two process can occur: radiative decay to the various $4f^{11}$ states with probability $W_{rad(LS)}$ and non-radiative decay to the HS $4f^{10}5d$ state with probability W_{nr}. From the HS $4f^{10}5d$ state, the only process that can occur is the radiative decay with probability $W_{rad(HS)}$ (see Figure 4.20 (b)). Thus, the competition between radiative and non-radiative decay from the LS states determines the relative intensities of spin-allowed and spin-forbidden *d-f* emission [Weg98] :

$$R_{SF/SA} = \frac{W_{nr}}{W_{rad}^{LS}} \tag{4.14}$$

One can easily see that without taking into account cross-relaxation processes Equation (4.8') transforms to the form of (4.14) ($R_{SA/SF} = (R_{SF/SA})^{-1}$, $W_{nr} = W_{ISC} + W_{d-f}$).

Finally, following values were obtained by Wegh according to the above mentioned empirical model: W_{rad}=1.9·10^7 s^{-1} and W_{nr}=2.0·10^8 s^{-1}. Comparison with (4.12) and (4.13) accentuates the important role of the cross-relaxation among the processes leading to the depopulation of the *d*-states of Er^{3+} ion in YLF.

After the system was excited with photons of the energy higher than LS state, two possibilities for the branching of the *d-f* emission can be considered. The first one supposes rapid relaxation to the LS state with subsequent branching into the different luminescence channels. The second one assumes branching starting immediately after excitation. The comparison of the excitation spectra for the SA and SF emission shown in Figure 4.21 gives a clear proof in favour of the second model, indicating that branching of the *d-f* emission depends on the excitation energy.

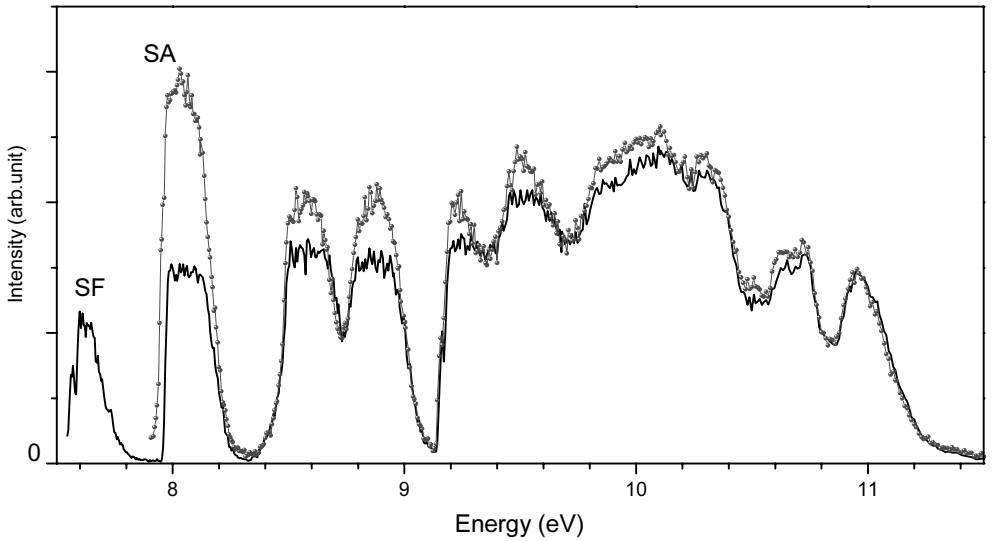

Figure 4.21: *Excitation spectra for spin-allowed and spin-forbidden d-f luminescence of $LiYF_4$:Er(1%) at T=9 K. Assignments of the curves are given in the figure. Both curves are normalised to the intensity value at10.8 eV.*

A significant energy redistribution as a function of the doping concentration takes place in the infrared and visible parts of the spectra as well. The set of emission spectra depicted in Figure 4.22 mirrors the relative intensities of intra-configurational *f-f* transitions depending on Er^{3+} concentration. All the spectra shown were excited with hν = 10.8 eV VUV-photons at room temperature. The Er^{3+} concentration was varied from 1% to 30%. The spectra were measured with a somewhat reduced spectral

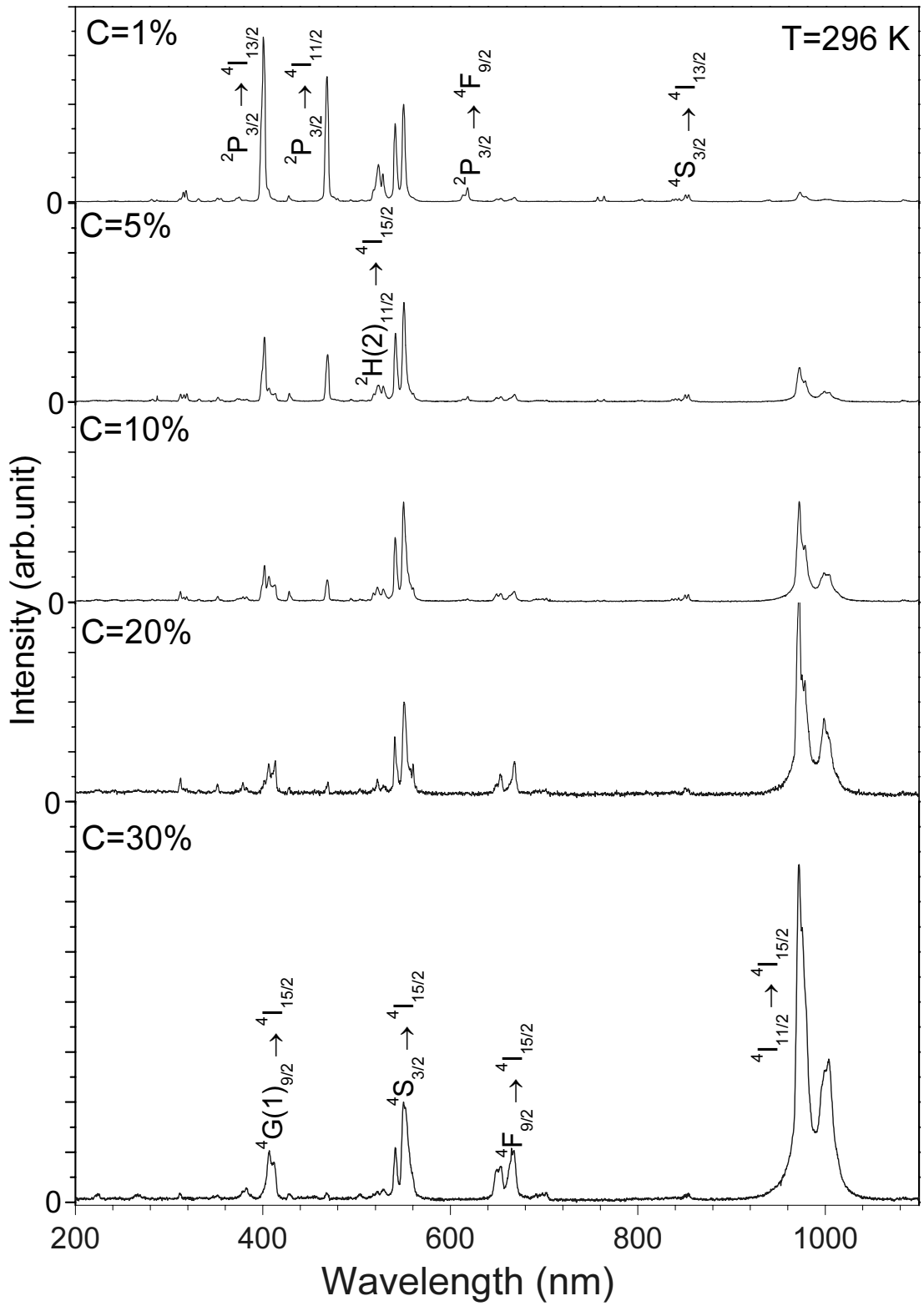

Figure 4.22: *Luminescence of $LiYF_4:Er^{3+}$ as a function of Er^{3+} concentration at T=296 K. Excitation was achieved with VUV photons ($h\nu$ = 10.8 eV). All spectra are normalized to the most intense peak originating from $^4S_{3/2} \rightarrow {}^4I_{15/2}$ emission. The assignments of the most intense lines are given in the figure.*

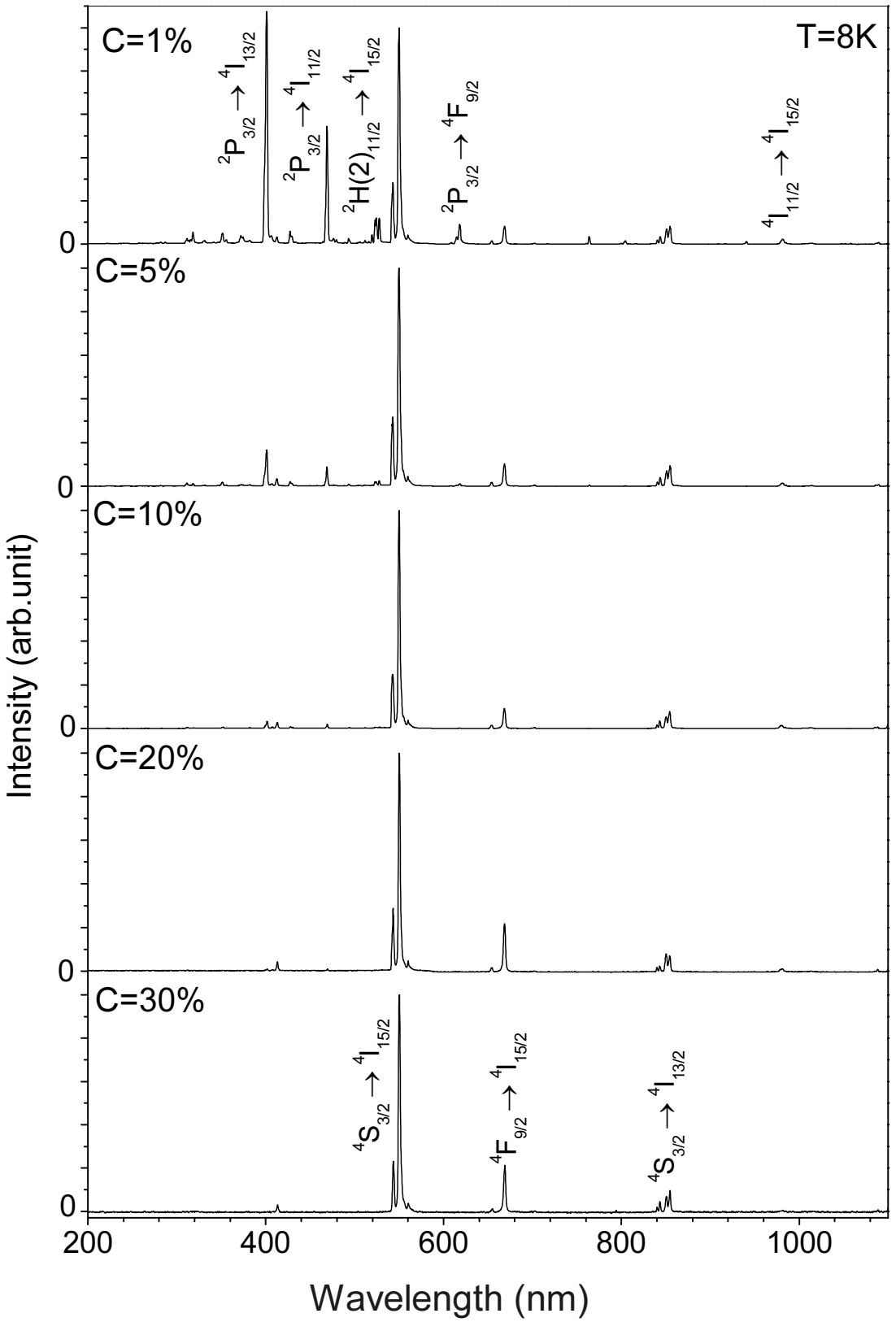

Figure 4.23: *Luminescence of $LiYF_4:Er^{3+}$ as a function of Er^{3+} concentration at T=8 K. Excited by10.8 eV photons. All spectra are normalized to the most intense peak originating from $^4S_{3/2} \rightarrow {}^4I_{15/2}$ emission. The assignments of the most intense lines are given in the figure.*

resolution ($\Delta\lambda$ = 1.6 nm). As it is nearly impossible to compare spectra originating from different crystals (different alignments, surface properties etc) in an *absolute* scale, the spectra were normalized to the most intense component of the $^4S_{3/2} \rightarrow {}^4I_{15/2}$ emission.

The dominant transitions originate from the $^2P_{3/2}$ state, terminating at the $^4I_{13/2}$ (402 nm) and at the $^4I_{11/2}$ (470 nm) states, and from the $^4S_{3/2}$ state terminating at the $^4I_{15/2}$ ground state (550 nm). The numbers given in the brackets correspond to the wavelength of the respective main peak values. Significant concentration quenching is obvious for radiative transitions originating from the $^2P_{3/2}$ state. The most striking observation in Figure 4.22 concerns the behaviour of the $^4I_{11/2} \rightarrow {}^4I_{15/2}$ emission. At low concentration it is practically absent (note, however, the considerably reduced sensitivity of the monochromator-detector system in this spectral region). The presented spectra are not corrected for the transmission function of the respective detector and monochromator, otherwise the intensity of the infrared emission in the highly doped systems is enhanced so strongly that other emission bands practically vanish. The same set of measurements has been performed also at T=8 K (see Figure 4.23) resulting in a very similar concentration dependency of electronic relaxation

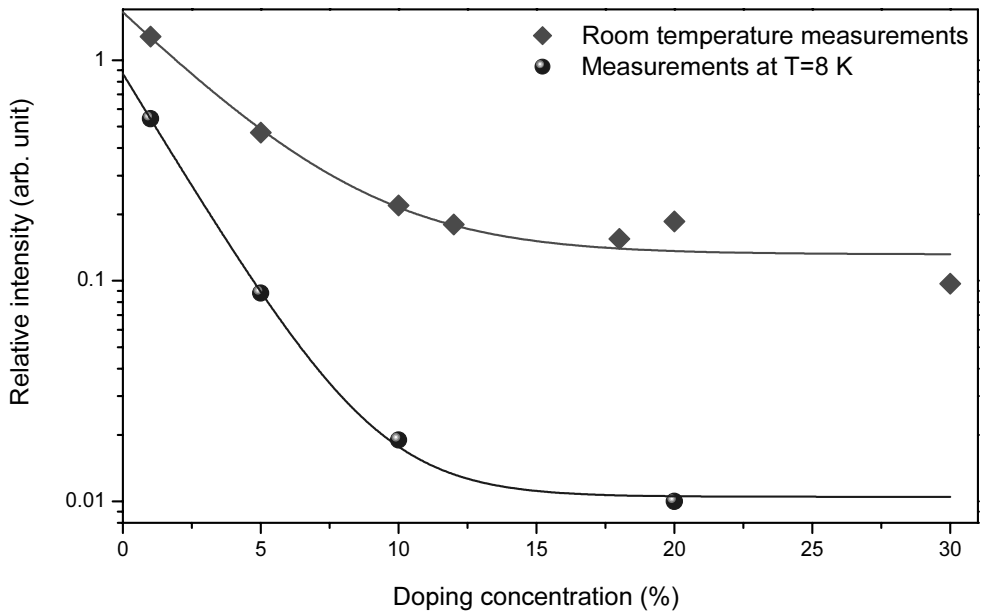

Figure 4.24: *Intensity of the $^2P_{3/2} \rightarrow {}^4I_{11/2}$ emission as a function of the doping concentration at T=8 K and at room temperature. Points present experimental data and respective fits are shown as solid lines.*

(not corrected for the apparatus function as well). The most outstanding difference between low and room temperature spectra is the negligible relative intensity of the $^4I_{11/2} \rightarrow {}^4I_{15/2}$ emission even in highly concentrated system. Raising the temperature and the concentration makes it the strongest *f-f* emission. As the dramatic enhancement of the emission requires higher concentration and elevated temperature, it indicates that non-radiative decay and cross-relaxation processes efficiently populate the $^4I_{11/2}$ state.

In order to trace the quenching of the $^2P_{3/2}$ emission, the intensity of the emission band (peak value) as a function of the doping concentration at T=8 K and at room temperature is plotted in Figure 4.24. As a probe, $^2P_{3/2} \rightarrow {}^4I_{11/2}$ emission was chosen because it has sufficient intensity and there is no overlap with other bands. The experimental data points can be very well fitted with a single exponential dependency (solid curves in the figure). Then the relative intensity of the emission can be predicted for different doping concentrations. The same procedure for other emission bands undergoing quenching can, in one's turn, give a preliminary assessment of the luminescence spectrum of $LiYF_4$ doped with any desired amount of Er under certain condition (temperature, excitation energy).

4.3.3 Temperature

The fact that the temperature also strongly influences electronic relaxation is evident from previous measurements. In addition to Figure 4.22 and 4.23 showing emission spectra under *d*-excitation, Figure 4.25 demonstrates effect of the striking energy redistribution in emission spectra obtained at different temperatures following selective Er^{3+} $^4D_{5/2}$ excitation with hν=4.86 eV. The upper curves were recorded for the crystal with the lowest doping concentration of Er^{3+} ions. The luminescence originating from $^2P_{3/2}$ state becomes about two times stronger at room temperature indicating that this state is efficiently populated with an increase of the temperature. In addition, $^2H(2)_{11/2} \rightarrow {}^4I_{15/2}$ emission around 522 nm becomes more efficient at room temperature, indicating thermal redistribution between $^4S_{3/2}$ and $^2H(2)_{11/2}$.

In the case of highly concentrated systems (see lower part), the influence of the temperature is still more pronounced. Even without correction for the apparatus function (one has to keep in mind that at 1000 nm the sensitivity is about a few per cent of the maximum at 450 nm) the $^4I_{11/2} \rightarrow {}^4I_{15/2}$ transition intensity significantly

increases with increasing temperature. One of the explanation of such significant energy redistribution is cross relaxation of the type:

$$(^2P_{3/2}, {}^4I_{15/2}) \rightarrow (^2H(2)_{11/2}, {}^4I_{9/2})$$

As the cross relaxation is more efficient at enhanced concentration, it also explains the absence of radiative transitions originating from the $^2P_{3/2}$ in highly concentrated

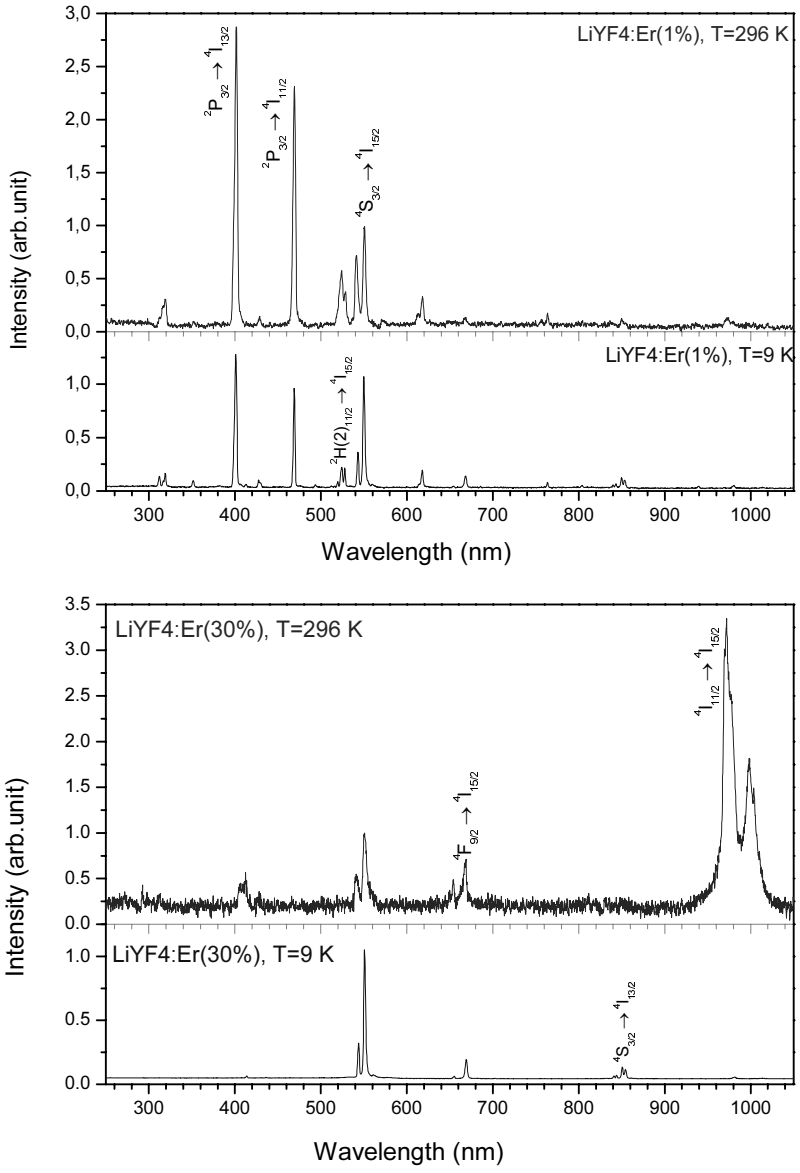

Figure 4.25: *Influence of the temperature on electronic relaxation. Top: luminescence of $LiYF_4$:Er(1%) at T=9 K and T=296 K. Bottom: luminescence of $LiYF_4$:Er(30%) at T=9 K and T=296 K. The curves were obtained following selective Er^{3+} $^4D_{5/2}$ excitation with hv=4.86 eV. All spectra are normalized to the peak originating from $^4S_{3/2} \rightarrow {}^4I_{15/2}$ transition. The assignments of the most intense lines are given in the figure.*

systems. So, the above mentioned cross relaxation can completely deplete the $^2P_{3/2}$ state in favour of the $^2H(2)_{11/2}$ and $^4I_{9/2}$, which consequently relax to the next low lying states $^4S_{3/2}$ and $^4I_{11/2}$ accordingly, due to the small energy separation between these levels.

4.4 Decay analysis

Experimental decay times of the Er^{3+} spin-allowed luminescence as a function of doping concentrations were obtained through the measurement of the decay curves (as was described in section 2.4.1). During the treatment of the data, different models were used. An analysis of the decay kinetics in a quantitative way is represented in the following section.

4.4.1 Simple model

In the simplest case the experimental decay curves for low doping concentrations can be fitted within the single exponential decay model with decay time τ:

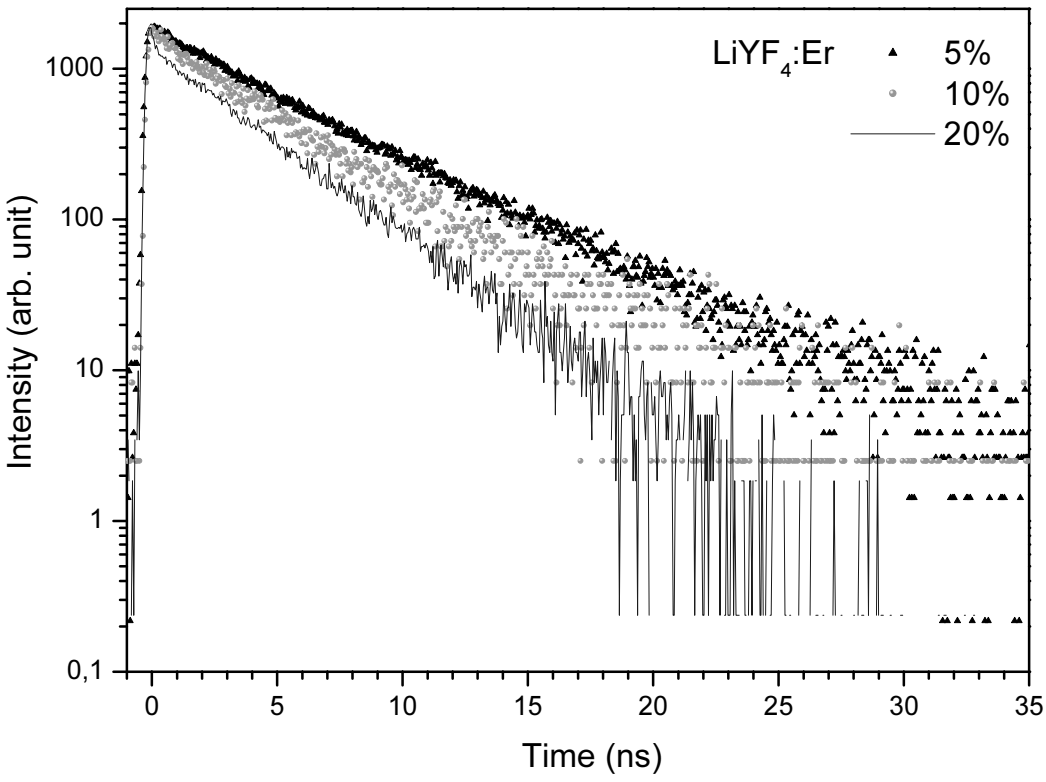

Figure 4.26: *Comparison of decay kinetics of the SA d-f luminescence of Er^{3+} for different doping concentration in $LiYF_4$, excited with 8.1 eV photons at T=10 K.*

$$I(t) = I_0 \cdot \exp(-\frac{t}{\tau}) \tag{4.15}$$

For example, for the $LiYF_4$:Er(1%) the single exponential decay fitting results in a decay time equal 5.56 ns (see Table 4.2). Interionic processes such as energy migration or cross-relaxation can strongly influence decay kinetics even at low doping concentration. Non-exponential behavior of decay curves becomes evident already at doping concentration more than 10%. Thus, the more complex model describing decay kinetics must be employed.

4.4.2 Inokuti-Hirayama model

A model of the luminescence decay proposed by Inokuti and Hirayama [Ino65] was developed with the assumption of the non-radiative energy transfer (see section 3.5). The luminescence decay kinetics within the Inokuti-Hirayama model is described by the following equation:

$$I(t) = I_0 \cdot \exp\left(-\frac{t}{\tau_{IH}} - \gamma \cdot \sqrt{t} \right), \tag{4.16}$$

where

$$\gamma = \frac{4}{3}\pi^{3/2} n_A \cdot \sqrt{C_{DA}} \,. \tag{4.17}$$

The so-called microparameter C_{DA} is a characteristic constant of the given ion and host (see Equation (3.29)). Moreover, C_{DA} is independent of the doping concentration. n_A is the concentration of acceptor ions. τ_{IH} represents radiative lifetime of a donor.

In Figure 4.27 SA *d-f* luminescence decay kinetics of $LiYF_4$:Er(5%) is shown (dots). If the exponential tail is extrapolated to $t = 0$ as it is shown in the figure (solid line) and subtracted from the data, the remainder *I(t)* is also seen to be non-exponential. The inset in Figure 4.27 demonstrates remainder *I(t)* plotted against $t^{1/2}$. Although the statistic is poor, the *I(t)* shows nice linear dependency on $t^{1/2}$ according to Equation (4.16).

In Figure 4.28 decay kinetics of the SA *d-f* luminescence for crystals with different Er doping concentration are depicted. Dots are experimental points, lines represent fit results according to the Inokuti-Hirayama model. As it can be seen from

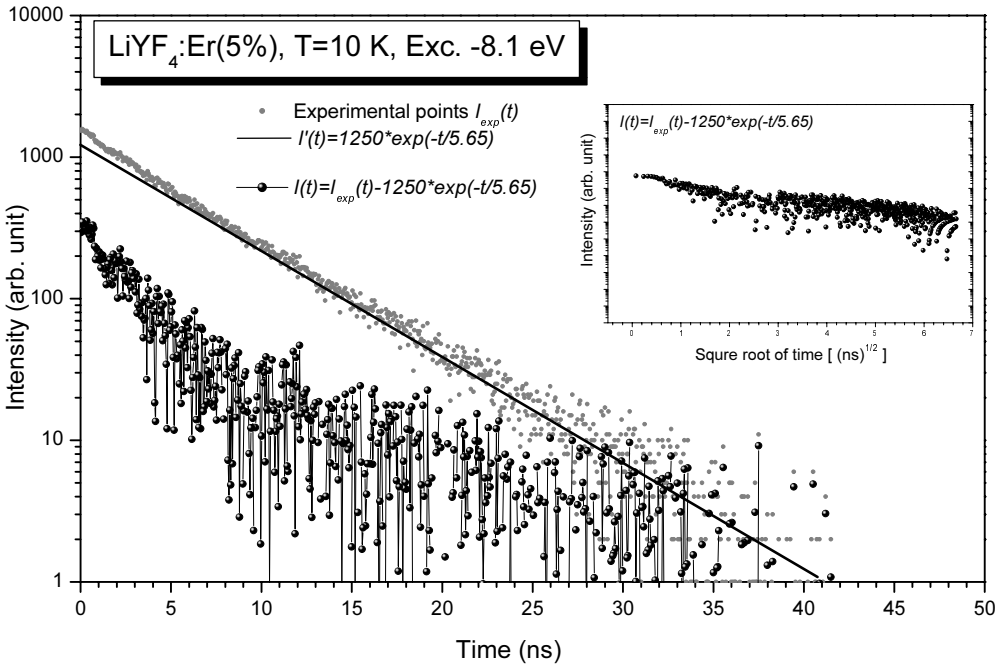

Figure 4.27: *Decay kinetics of the SA d-f luminescence of $LiYF_4$:Er(5%) crystal under 8.1 eV excitation at T=10 K. Dots are experimental points, solid line represents exponential decay. The remainder I(t) obtained after subtraction of the exponential part from the experimental data is shown as well. I(t) plotted against $t^{1/2}$ is demonstrated in the inset.*

the figure, the experimental decay curves follow very well the Inokuti-Hirayama model. The fitting parameters are summarized in Table 4.2 and confirm a fact that the increase of the doping concentration leads to the shortening of the decay time.

	τ [ns]	τ_{IH} [ns]	γ [$s^{-1/2}$]
$LiYF_4$:Er(1%)	5.56	5.67	865
$LiYF_4$:Er(5%)	5.25	5.65	1455
$LiYF_4$:Er(10%)	5.01	5.5	3000
$LiYF_4$:Er(12%)	4.81	5.41	3761
$LiYF_4$:Er(18%)	4.46	5.0	5440
$LiYF_4$:Er(20%)	3.79	4.78	5640
$LiYF_4$:Er(30%)	3.11	4.38	8290

Table 4.2: *Parameters of the fitting of decay kinetics obtained within the single exponential (τ) and the Inokuti-Hirayama (τ_{IH}) models.*

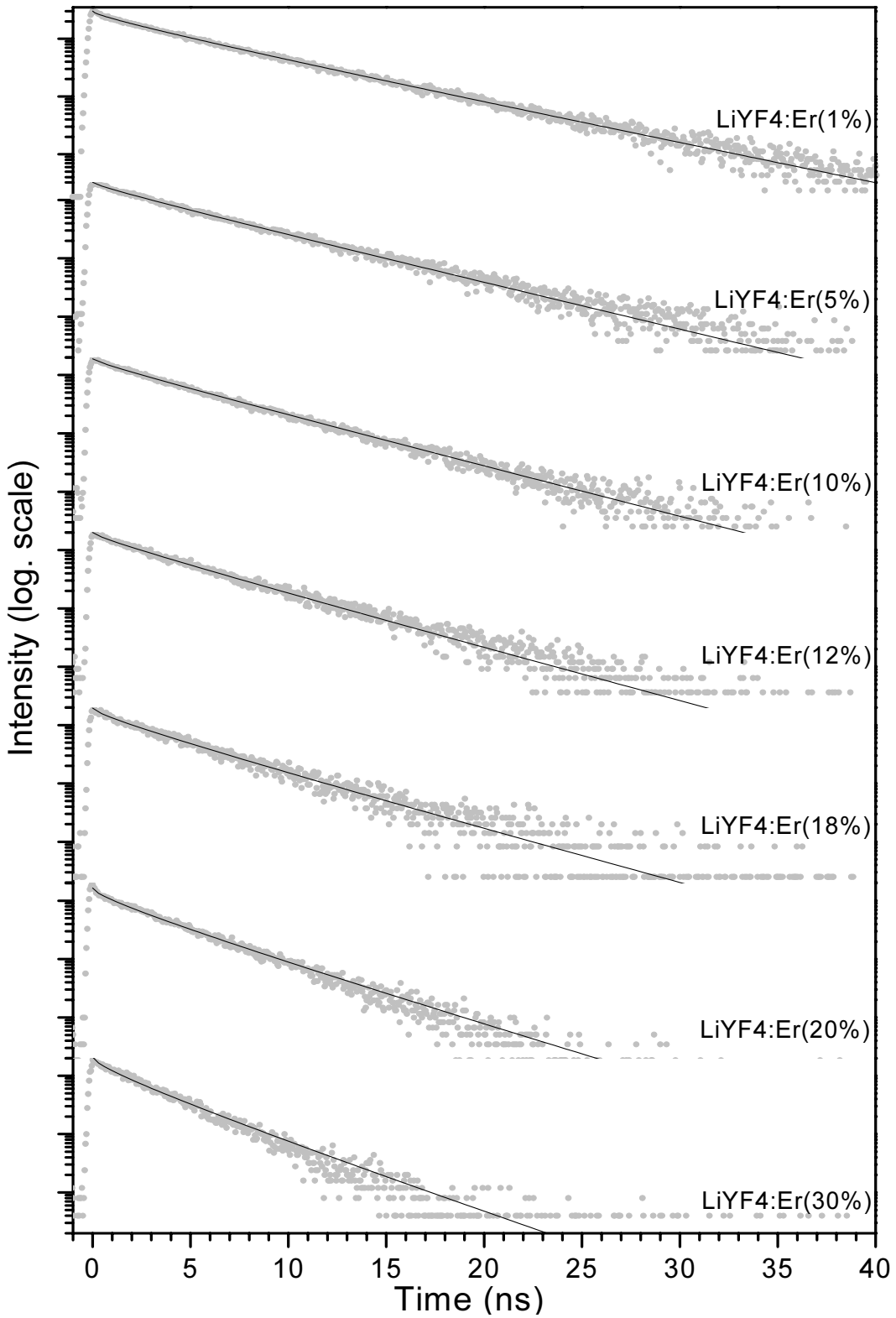

Figure 4.28: *Decay kinetics of the SA d-f luminescence for $LiYF_4$ crystals with different Er doping concentration. Excitation was achieved with 8.1 eV photons at T=10 K. Dots are experimental points, curves represent results of the fit according to the Inokuti-Hirayama model.*

As the increase of the Er^{3+} doping concentration leads to the shortening of the decay time of the fast SA luminescence, one can suppose that an energy transfer process such as cross-relaxation is responsible for the lifetime shortening. In this case the cross-relaxation rate can be represented as $\gamma\sqrt{t}$, with $\gamma \propto n_A$, where n_A is Er^{3+} concentration (see Equation (4.17)). Indeed, experimentally obtained values of the $\gamma(n_A)$, shown in the Figure 4.29 satisfy the linear dependence.

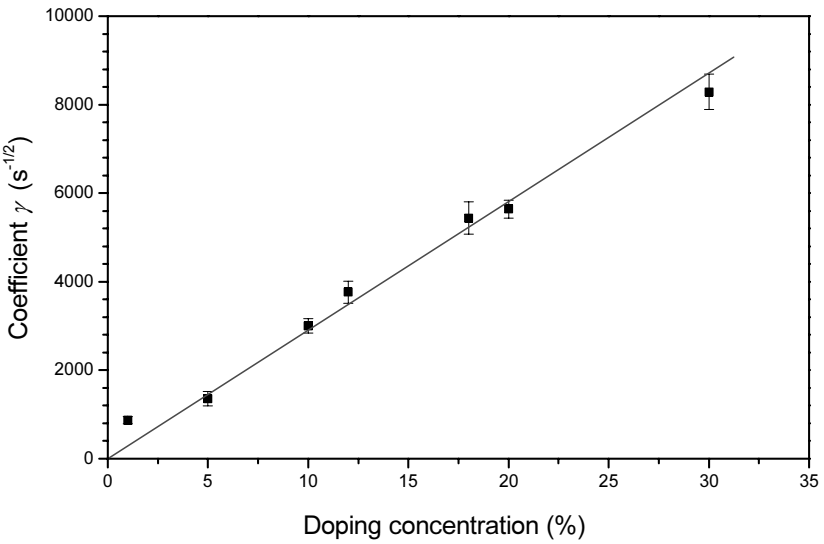

Figure 4.29: *Values of the γ parameter of the Inokuti-Hirayama model as function of Er concentration obtained by the fitting of experimental decay curves.*

Moreover, in the Inokuti-Hirayama model (Equation (4.16)), τ_{IH} is supposed to be independent of doping concentration. The fact that τ_{IH} depends on the doping concentration indicates that some additional energy transfer process, which was not taken into account in Inokuti-Hirayama model contributes to the decay kinetics. And the higher is the doping concentration, the greater becomes this contribution.

4.4.3 Introduction of the donor-donor transfer

One of the initial assumptions of the Inokuti-Hirayama model is the absence of the donor-donor-interactions. If the donor-donor transfer occurs in addition to the donor-acceptor transfer the luminescence decay kinetics is described by the following expression:

$$I(t) = I_0 \cdot \exp\left(-\frac{t}{\tau_0} - \gamma \cdot \sqrt{t} - W_D \cdot t \right) \quad , \tag{4.18}$$

where γ is given by Equation (4.17), and W_D is an ensemble-averaged migration-assisted energy transfer rate between donors. τ_0 is the intrinsic decay time of the excited donor ion. As it was described in the section 3.5, two approaches are employed to treat energy migration between donors. Both the *diffusion* model and the *hopping* model are approximate, but not equivalent, approaches to the general problem of donor-acceptor energy transfer in the presence of donor-donor migration. Huber [Hub79] has investigated the regions of validity of both models, and the general problem has been extensively reviewed by Burshtein [Bur85].

In case when the donor-donor transfer mechanism is much weaker than the donor-acceptor transfer mechanism, *i.e.* $\boldsymbol{C_{DD} \ll C_{DA}}$ (realized at low temperature up to 15-30 K depending on the system [Heg81, Heg82]), the *diffusion* model is valid with

$$W_D = W_{diff} = \frac{16}{3}\pi^2 \left(\frac{1}{2}\right)^{\frac{3}{4}} \cdot n_A \cdot n_D \cdot (C_{DA})^{\frac{1}{4}} \cdot (C_{DD})^{\frac{3}{4}} . \tag{4.19}$$

If the donor-donor transfer mechanism dominates over the donor-acceptor transfer mechanism *i.e.* $\boldsymbol{C_{DD} \geq C_{DA}}$ the *hopping* model is valid, and

$$W_D = W_{hopping} = \sqrt{\frac{8}{27}\pi^5} \cdot n_A \cdot n_D \cdot \sqrt{C_{DA} \cdot C_{DD}} . \tag{4.20}$$

Here C_{DD} and C_{DA} are microparameters of the donor-donor and the donor-acceptor energy transfer for the dipole-dipole interaction. They are characteristic constants of the given ion and host. n_A and n_B are concentrations of the acceptor and donor ions respectively.

The parameter τ_{IH} obtained from the fitting of the decay curves according to the Inokuti-Hirayama model can now be written as $\frac{1}{\tau_{IH}} = \frac{1}{\tau_0} + W_D$ (compare Equations (4.16) and (4.18)). $1/\tau_{IH}$ as a function of the doping concentration is shown in Figure 4.30. Then the values of $1/\tau_0$ and W_D (given in Table 4.3) can be determined from the graph. As it was already mentioned in section 4.3, W_{ISC} and $W_{d\text{-}f}$, which were not taken into account in models discussed above, are independent of the doping concentration and contribute into the calculated $1/\tau_0$ as a regular constituents (see

	$1/\tau_{IH}$ [x10^8 s^{-1}]	γ [$s^{-1/2}$]	W_D [x10^8 s^{-1}]
$LiYF_4$:Er(1%)	1.76	865	0.016
$LiYF_4$:Er(5%)	1.77	1455	0.028
$LiYF_4$:Er(10%)	1.82	3000	0.071
$LiYF_4$:Er(12%)	1.85	3761	0.101
$LiYF_4$:Er(18%)	2.00	5440	0.293
$LiYF_4$:Er(20%)	2.09	5640	0.349
$LiYF_4$:Er(30%)	2.28	8290	0.536

Table 4.3: *Fitting parameters obtained within the model described by Equation (4.18).*

Equation 4.11). From the value of the radiative decay probability (see expression (4.12)) the radiative decay time of the SA *d-f* luminescence is estimated to be 84 ns.

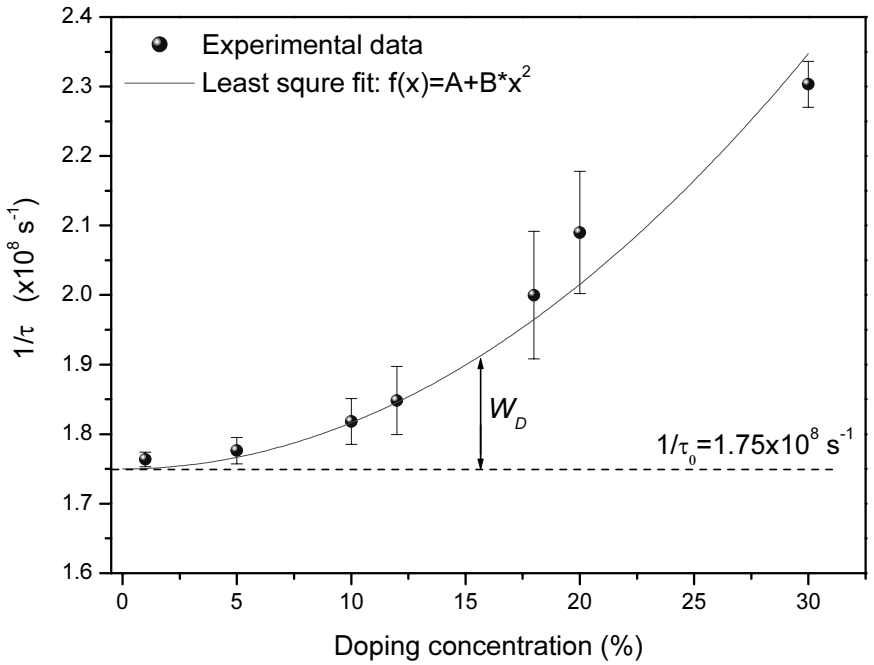

Figure 4.30: *Values of $1/\tau_{IH}$ as function of the doping concentration obtained from the fitting of the experimental decay curves within the Inokuti-Hirayama model.*

The migration-assisted energy transfer rate between donors W_D in case of the *hopping model*, as in case of the *diffusion model*, in general depends on both donor and acceptor concentrations (Equation (4.19) and (4.20)). In $LiYF_4$:Er system Er^{3+} ions appear both as donors and as acceptors concurrently. Thus W_D obtained from the fitting procedure satisfies the quadratic dependency on Er^{3+} doping concentration as it is shown in Figure 4.29.

	C_{DA} [10^{-38} cm^6 s^{-1}]	R_o [Å]	C_{DD} (Diffusion) [10^{-37} cm^6 s^{-1}]	R_o^{DD} (Diffusion) [Å]	C_{DD} (Hopping) [10^{-36} cm^6 s^{-1}]	R_o^{DD} (Hopping) [Å]
1%	70.7	4.60	43.5	6.23	116.6	10.78
5%	8.00	3.20	1.88	3.69	3.12	5.89
10%	8.51	3.24	1.32	3.48	1.78	5.37
12%	9.29	3.28	1.27	3.46	1.60	5.27
18%	8.64	3.24	1.81	3.67	2.85	5.81
20%	7.52	3.20	1.81	3.67	3.04	5.87
30%	7.22	3.15	1.10	3.38	1.47	5.20

Table 4.4: *Calculated values of the microparameters C_{DA} and C_{DD} and the range parameters for donor-acceptor (R_0) and donor-donor (R_0^{DD}) energy transfer in LiYF4:Er system using diffusion and hopping models.*

After W_D, γ, τ_0, have been determined, other important parameters can be calculated. The value of the microparameter C_{DA} can be obtained from Equation (4.17). The critical radius R_0, was calculated using Equation (3.34). From Equation (4.19) and (4.20) C_{DD} can be calculated within the *diffusion* and *hopping models* respectively. The values of the C_{DA}, C_{DD} and R_0 are collected in Table 4.4 and will be discussed in the next section.

The donor-donor transfer is strongly dependent on temperature, varying as T^3 up to 30K [Heg82]. At very low temperature this transfer is negligible, only donor-acceptor transfer is effective, and the decay has the non-exponential pattern predicted for such a situation. Moreover, the diffusion model is expected to be valid at low

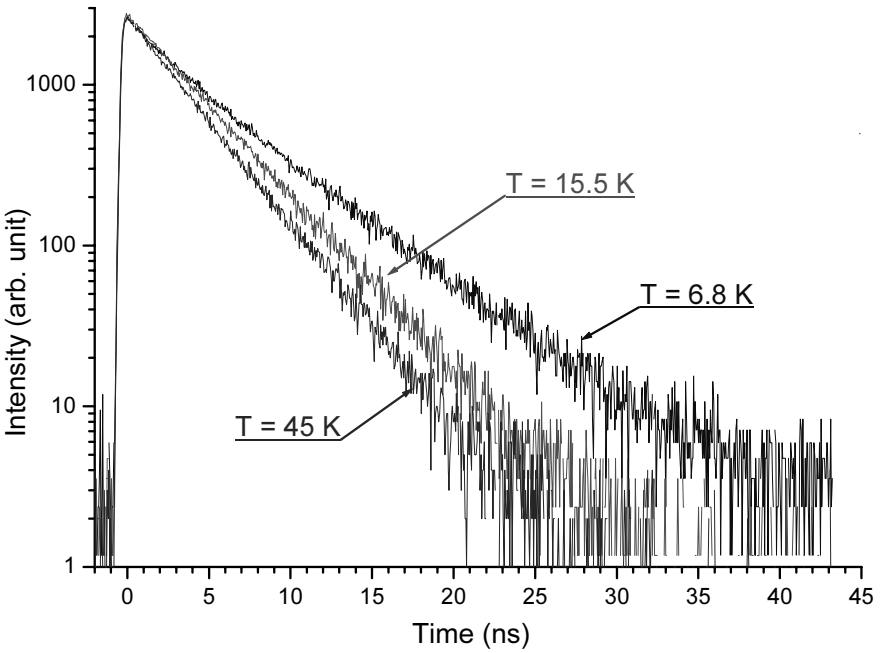

Figure 4.31: *Decay curves of SA d-f luminescence for $LiYF_4$:Er(5%) excited with 8.05 eV photons and measured at different temperatures. Respective temperatures are given on the graph.*

temperatures. The increase of the temperature leads to the increase of the energy migration rate from the *static* case, *i.e.* without donor-donor transfer, to very rapid transfer and subsequent exponential decay at temperatures of ≥ 30K. The situation described above is depicted in Figure 4.31. Three decay curves of SA *d-f* luminescence for $LiYF_4$:Er(5%) measured at different temperatures are shown. One can easily see that an increase of the temperature favors the shortening of the decay. As migration increases the decay becomes exponential at earlier times except for a small region around t = 0. In the limit of exceedingly fast migration the decay becomes single exponential as it is described on page 49 (see Equation (3.49)).

In addition, a quantitative confirmation of the theory is given in Figure 4.32, where experimental data are fitted with above discussed model and fitting parameters are shown on the graph.

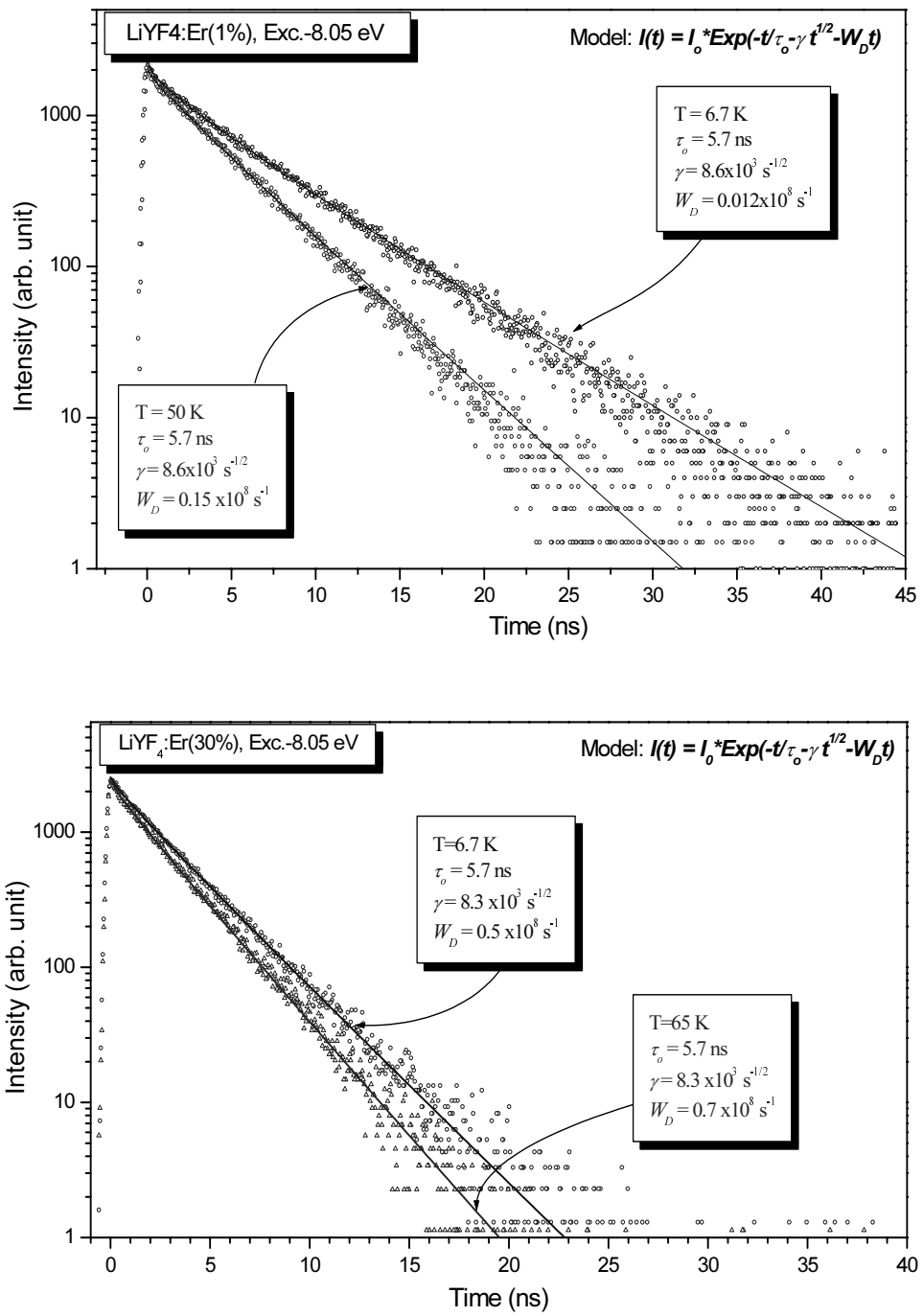

Figure 4.32: *Decay curves of SA d-f luminescence for $LiYF_4$:Er excited with 8.05 eV photons and measured at different temperatures. Points present experimental data and respective fits are shown as solid lines. Temperatures, concentrations and fit parameters are given on the graph.*

4.4.4 Discussion

First of all it is necessary to make some notes concerning the fit procedure mentioned in the previous section. As it is known main criterion for the optimal fit is the minimal value of the chi-squared (χ^2). At the same time the χ^2 can have several local minima corresponding to different sets of the parameters. Thus one needs additional criteria to choose the proper solution. At the first step of the fitting procedure all the fit parameters were varied. With increasing doping concentration, fitting errors also increase due to the worse statistics. An analysis of the obtained solutions shows that for samples doped with 5%, 10% and 12% of Er the parameter γ satisfies perfectly Equation (4.17). Correction and subsequent fixation of γ for $LiYF_4$:Er(20%) in agreement with expression (4.17) gives a fit of the same quality (the same value of the χ^2). The same procedure has been done for $LiYF_4$:Er(30%). The quality of the fit becomes poor but still acceptable. However, this kind of adjustment of the parameter γ turned out to be ineffective for the crystal doped with Er(1%). This fact shows later up in the calculation of microparameters C_{DA} and C_{DD}, and values of the critical radius for the respective processes as a considerable jump of above mentioned parameters in $LiYF_4$:Er(1%)(see Table 4.4).

Such a discrepancy can be partly connected with the different origins of samples. $LiYF_4$:Er(1%) crystal was obtained from a different source than the others. In addition, as it was mentioned in the section 2.5, the presence of Pr^{3+} admixture was detected in the crystals with doping concentration more than 1%. Moreover the size of the $LiYF_4$:Er(1%) sample does not allow to cleave it before the measurement, thus different surface effects can influence the decay kinetics. At very high doping concentration, the formation of the Er-clusters becomes probable, which also alter the decay.

With the exception of results obtained for the $LiYF_4$:Er(1%) crystal, only slight deviations within the experimental error are observed. The averaged* value of the microparameter C_{DA} is $8.39 \cdot 10^{-38}$ cm^6 s^{-1}. When Er^{3+} ion is doped into $LiYF_4$, it substitutes Y^{3+}. The minimal distance between two Y^{3+} ions in $LiYF_4$ is $3.73 \cdot 10^{-8}$ cm. From this point of view the averaged value obtained for the critical radius of the cross-relaxation process R_0 equal to $3.23 \cdot 10^{-8}$ cm seems to be reasonable. Then the

* *Here and later the $LiYF_4$:Er(1%) and $LiYF_4$:Er(30%) crystals were not taken into account.*

critical Er concentration defined in terms of a range parameter R_0 by Equation (3.33) is calculated to be ~51%.

The microparameter C_{DD} was calculated within both *diffusion* and *hopping* models. The respective values are $1.62 \cdot 10^{-37}$ cm^6 s^{-1} and $2.48 \cdot 10^{-36}$ cm^6 s^{-1}. Consequently, the correlations between C_{DA} and C_{DD} resulting from the decay measurements are the following:

diffusion model: $C_{DD} \sim 2 \cdot C_{DA}$;

hopping model: $C_{DD} \sim 30 \cdot C_{DA}$.

As it was already mentioned in section 4.4.3, the diffusion model is valid when $C_{DA} >> C_{DD}$ and the hopping model is valid if $C_{DA} \leq C_{DD}$. So, from this criterion one might expect the hopping model to be a reasonable description of the behaviour.

A simultaneous application of the Inokuti-Hirayama model and the model taking into account donor-donor transfer (D-D model) seems, however, to be problematic. The use of the microparameter C_{DA} obtained within the Inokuti-Hirayama model (and, in particular, of the nominal doping concentration) in the D-D model implies the same energy transfer in both cases. In order to solve this problem, two questions has to be discussed:

(i) does it make sense to use both models simultaneously at all, and if yes

(ii) what input parameters for the calculation of the microparameters should be used?

Questions (i)

In a sample with diverging interaction, of the type $1/R^n$, there are always donors in which the excitation vanishes at an arbitrarily fast rate. The migration of the excitation over the sample accelerates its decay only because it provides access to these donors (energy sinks)[Bur72]. The movement of the excitation over the donors changes the trapping efficiency strongly since all the excitations, including those which are initially remote from any trap, can now move to ions which have traps as near neighbours. The presence of such traps (“killer centres”) simply shortens the lifetime of donors. A strong concentration dependence indicates that the “killer centres” are somehow related to a local accumulation of ions (ion pairs, triads or small clusters; it is a well known fact that the rare earth ions have a tendency to form clusters).

One can think about the effect of *pairing* firstly suggested by Varsanyi and Dieke [Var61] in LaF_3:Pr and investigated by Imbusch [Imb67] in ruby (Cr^{3+} in Al_2O_3). When two (or more) Er^{3+} ions are close enough to interact strongly with each other, the resultant complex may act as a single optical centre with distinct spectroscopic properties, while the individual centres lose their separate identities. The energy transfer from single ions to pairs is shown to occur nonradiatively, and its efficiency is enhanced by a fast energy transfer between individual single ions [Imb67]. Moreover, the density of pairs increases as the square of the doping concentration. If one assumes that the probability of the above mentioned process is a constituent of W_D in expression (4.18), then it can partly explain the high value of C_{DD}.

In addition, it is entirely reasonable to observe donor-acceptor energy transfer according to the Inokuti-Hirayama model among ions on the regular lattice sites. The simultaneous appearance of the donor-acceptor and donor-donor transfers then means that the final step of the transfer process is different. In one case it leads to an excitation of an acceptor, in the other case, it is *e.g.* quenching process.

Questions (ii)

The analysis of the decay kinetics of SA luminescence of Er^{3+} in $LiYF_4$ yields τ_0, γ, and W_D. Figures 4.29 and 4.30 clearly show that parameter γ and W_D are related to the Er^{3+} concentration. In the temperature range $8 \lesssim T \lesssim 30$ K the decay of the donor ions is a result of competing donor-donor and donor-acceptor transfer processes. The fact that the both kind of transfer appear simultaneously then means that Er ions occupy at least two distinct types of site in the crystal. Ions in the one type of site are involved in “killer centres” and, as it was already mentioned, may be related to the accumulation of ions. Er ions of the other type are, accordingly, not involved in “killer centres”.

The discrimination between different classes of ions influences the deduction of the microparameters from the measured γ and W_D values. It seems to be justified, at least at low concentration limit, to take the overall concentration of Er^{3+} for the calculation of the microparameter C_{DA}. Here one can even speculate that the decrease of C_{DA} for high concentrations (see Table 4.4) arises from an overestimate of the “true concentration” (Er ions in regular sites) by the total concentration.

The calculation of the microparameter C_{DD} from W_D is, however, questionable. Taking into account the existence of two types of Er^{3+} ions, at least n_A in expressions (4.19) and (4.20) should be replaced by an estimate of the "killer centres" concentration. Moreover, C_{DA} involved in these expressions is not any longer identical with that obtained within the Inokuti-Hirayama model. On the basis of the present results it would be speculative to go into more details. The values of the microparameter C_{DD} in Table 4.4 are therefore only rough estimates, whereas the value of C_{DA} is reliable.

The ion-ion interaction in lanthanide solid-state systems has been the subject of numerous investigations in order to understand the fundamental aspect of this interaction. A very similar analysis of the energy transfer among Er^{3+} ions in LaF_3 has been performed by Okamoto *et al.* [Oka75] in the middle of the 70ies. The decay kinetics of the excited $^4S_{3/2}$ state of Er^{3+} ions at 295 K was studied. The value of the cross-relaxation constant (as the C_{DA} parameter was called) they obtained varied from sample to sample by a factor of 2. The averaged values of C_{DA} and C_{DD} were calculated to be $4.5 \cdot 10^{-41}$ $cm^6\ s^{-1}$ and $7.0 \cdot 10^{-40}$ $cm^6\ s^{-1}$ respectively ($C_{DD} \sim 16 \cdot C_{DA}$).

	C_{DA} [10^{-39} $cm^6\ s^{-1}$]	C_{DD} [10^{-39} $cm^6\ s^{-1}$]	R_0 [10^{-8} cm]
$LiYF_4:Er^{3+} \rightarrow Er^{3+}$	83.9	162 / 2480	3.23
$LiYF_4:Nd^{3+} \rightarrow U^{3+}$ [Lou96]	160	21.0	-
*$LaSc_3(BO_3)_4$: $Yb^{3+} \rightarrow Er^{3+}$ [Leb00]	4.16	35	8.4
*$LiLaP_4O_{12}:Nd^{3+} \rightarrow Yb^{3+}$ [Lur86]	1.6	4.0	5.8
*$YAG:Nd^{3+} \rightarrow Nd^{3+}$ [Lup89]	0.18	-	-
*$LaF_3:Er^{3+} \rightarrow Er^{3+}$ [Oka75]	0.045	0.7	3.7
*$LiYF_4:Tm^{3+} \rightarrow Tm^{3+}$ [Raz95]	0.059	3.24	-
*YF_3: $Yb^{3+} \rightarrow Ho^{3+}$ [Wat72]	0.018	-	6.0

Table 4.5: *Values of C_{DA}, C_{DD} and R_0 obtained from literature for interactions between two lanthanide ions in different host matrices. * - measurements done at room temperature.*

The values of C_{DA}, C_{DD} and R_0 calculated in this work are given in Table 4.5 in comparison with other values obtained from the literature for interactions between two lanthanide ions. It should also be mentioned that with the exception of the paper of Louis *et al.* [Lou96] ($LiYF_4:Nd^{3+} \rightarrow U^{3+}$, authors imply the Inokuti-Hirayama and D-D models simultaneously as well) and this work, all values given in the table were obtained for the *4f-4f* system. It was shown by Dexter[Dex53] that in the case of the multipole-multipole interaction the energy transfer probability is proportional to the rates of the radiative transition involved on both donor and acceptor (whereas for the exchange interaction there is no dependence on radiative transition rates). Thus, for the parity allowed *d-f* transitions non-radiative energy transfer rate expected to be significantly higher than for the parity forbidden *f-f* transitions. This fact is in a good agreement with the data represented in Table 4.5.

In addition, the existence of several non-equivalent centres can contribute to the observed decay kinetics. As possible sources for these non-equivalent sites were considered distortions of the lattice due to the size mismatch between Y^{3+} and RE^{3+}, the departure from stoichiometry [Deb81], or strains in the lattice caused by impurities. The existence of regions with defects or dislocations, facets, inclusions and so on produce local differences in the Er concentration that also influence the results.

In the case of dipole-dipole interaction $C_{DA} \approx B\frac{Q_A}{\tau_{rad,D}}\int\frac{f_D(E)F_A(E)}{E^4}dE$ (see Equation (3.29)) where B is a constant, Q_A is the acceptor integral absorption cross section, $\tau_{rad,D}$ is the radiative lifetime of the donor ion level, and $f_D(E)$ and $F_A(E)$ are the normalised donor emission and acceptor absorption band shapes (in the photon energy E space). In a homogeneous system, the microparameter C_{DA} is identical for all donor–acceptor pairs. If all the multipolar D–A interactions are possible, for a nearest acceptor, the transfer mechanism is determined by a mixed interaction picture. However, for a distant acceptor, this picture is usually dominated by the dipole–dipole interaction [Lup99]. In sensitized crystals, the mutual asymmetric D–A crystal field perturbations transform the homogeneous systems of D and A ions in inhomogeneous, but composed by homogeneous subsystems. Since the high-order multipolar interactions are short-range interactions and the perturbations at the donor site are caused by the nearest acceptor, the selective manifestation of the mixed interaction

picture in the energy transfer is possible for each of the perturbed subsystems. Moreover, it was shown in [Bas96] that when more than one of the multipolarities contribute to the energy transfer, the total rate takes a more complicated form and is not equal to the sum of the individual rates.

Relations (4.16) and (4.17) are valid if the interaction is of a dipole-dipole type with all the acceptors. An attempt to fit the decay kinetics within the Inokuti-Hirayama model in the common case (Expression 3.32) has been done as well. The multipole order *s* was varied to get the best fit. The very good agreement with previous results (dipole-dipole interaction) was obtained for the crystals with doping concentration less than 18%. Better fit turned out to be possible for other samples if $s > 7$. In [Lup89] it was also assumed that dipolar interaction is dominated by a short-range interaction (that can be of superexchange type) leading to a much faster drop in I(t) at the beginning of the decay but not affecting the interaction with the more distant ions. The experimental confirmation of this assumption has been found. This fact may causes the discrepancy between the values of C_{DA} (for high concentration) defined from the parameter γ. A similar conclusion was made by Morgan, Huber and Yen [Mor86], when they studied the nature of the $^3P_0$ fluorescence quenching processes in $LaF_3:Pr^{3+}$. Two models were used and the obtained results were compared and discussed. In the first model (the continuum model of Inokuti and Hirayama) a long range multipolar interaction is assumed to be responsible for the cross-relaxation process, while in the second model a short-range superexchange interaction is proposed. The parameters obtained from the long-range model are considered to be more fortuitous than an actual indication of the accuracy of the model [Mor86]. Although at later times the fluorescence decay profile can be described with reasonable success by both models, it was concluded that the short-range superexchange interaction is dominant and provides the most consistent description of the fluorescence decay.

There is a number of interesting questions attached to the donor-donor transfer. Is it, for example, a resonant or non-resonant process? What are the effects of random strains and lattice defects, since these can shift the electronic levels of adjacent ions out of resonance with each other. The resultant inhomogeneous broadening of a transition can be much larger than the homogeneous broadening, particularly at low temperatures [Hen89]. Obviously, further investigations in this

direction with stronger requirements to the samples quality and smaller doping concentration are desired.

4.4.5 Cross-relaxation

As was discussed in previous sections, as the concentration of Er^{3+} ions is increased in $LiYF_4$, both the quantum efficiency and luminescence lifetime decrease for the LS $4f^{10}5d$ state. This concentration quenching has been attributed to the quenching at "killer center". In case of the resonant transfer among the ions (in this type of process an excitation can be transferred from one ion to a neighboring ion such that second ion ends up in the same excited state), this process was labeled as donor-donor transfer in order to distinguish it from the cross-relaxation, labeled as donor-acceptor process.

Then, however, question arises what kind of cross-relaxation process it is. To answer this question, the set of emission curves measured at T=9 K after excitation just above highest LS *5d* state for different Er concentration is shown on Figure 4.33. As before, all curves are normalized to the most intense emission band peaking at 550 nm (to get more detailed information about bands with low intensity, the spectra are shown in an enlarged scale). Luminescence intensity of the several transitions changes with doping concentration. Whereas $^2P_{3/2} \rightarrow {}^4I_{13/2}$, $^2P_{3/2} \rightarrow {}^4I_{11/2}$ and $^2P_{3/2} \rightarrow {}^4F_{9/2}$ luminescence is almost completely quenched already in $LiYF_4$:Er(20%), emission intensity of the $^4F_{9/2} \rightarrow {}^4I_{15/2}$ continuously rises with the increase of Er^{3+} doping concentration. Relative luminescence intensities as functions of the doping concentration for above mentioned emission bands are plotted in Figure 4.34. Such a behavior can be explained by the presence of the cross-relaxation process, which occurs in two steps:

$$(4f^{10}5d\,(\mathrm{LS}),\ {}^4I_{15/2}) \rightarrow ({}^2P_{3/2},\ {}^2P_{3/2}) + \Delta E_1$$
$$({}^2P_{3/2},\ {}^4I_{15/2}) \rightarrow ({}^4F_{9/2},\ {}^4F_{9/2}) + \Delta E_2$$

where $\Delta E_1 \approx 50\ \mathrm{cm}^{-1}$ and $\Delta E_2 \approx 350\ \mathrm{cm}^{-1}$.

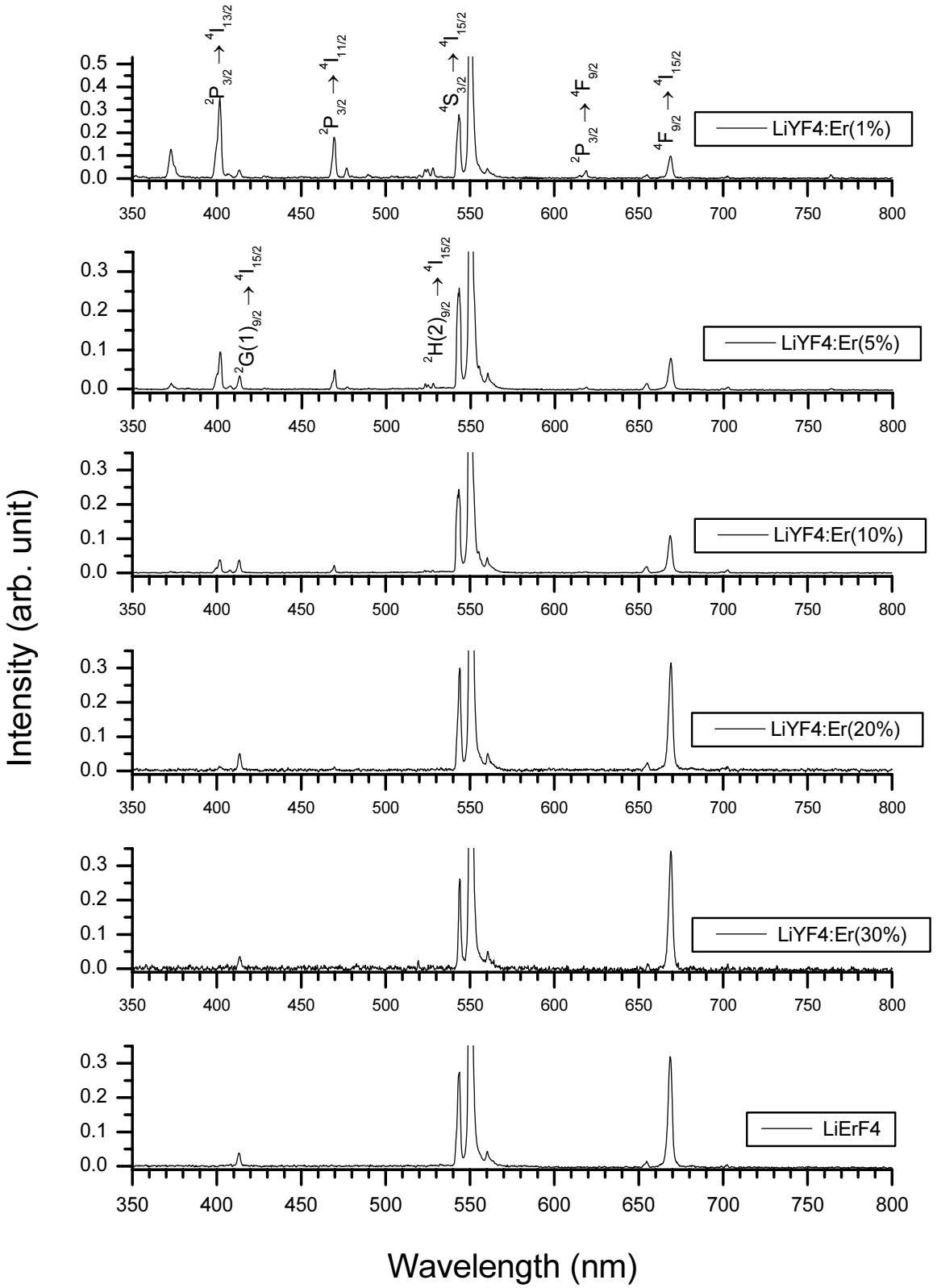

Figure 4.33: *Luminescence of LiYF4:Er as a function of Er^{3+} concentration. All curves are normalized to the most intense emission band peaking at 550 nm. Excitation was achieved with VUV photons (hv = 8.05 eV) at T = 9 K.*

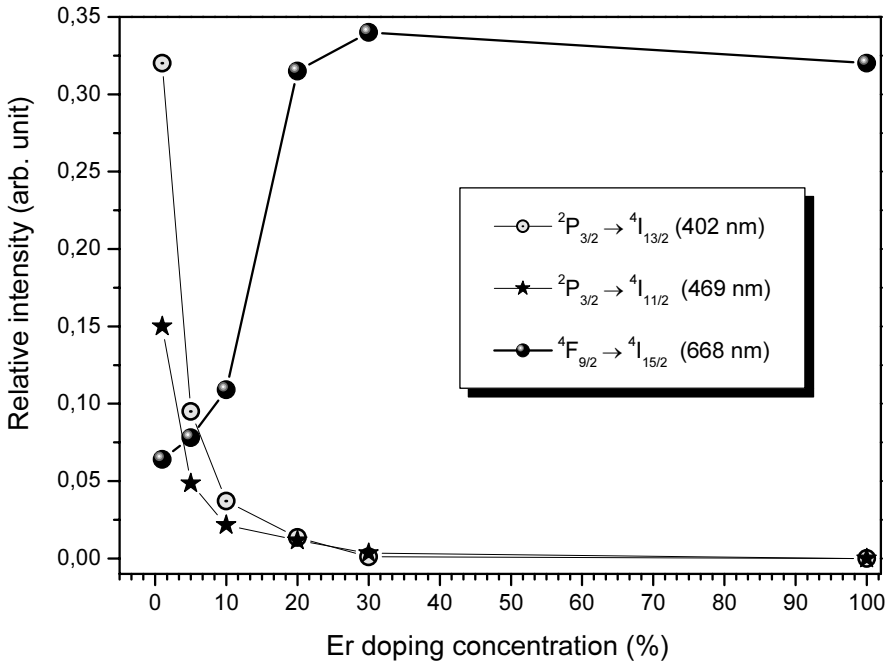

Figure 4.34: *Relative intensity of certain luminescent transitions as a function of the doping concentration. The respective assignments of the transition are given on the figure.*

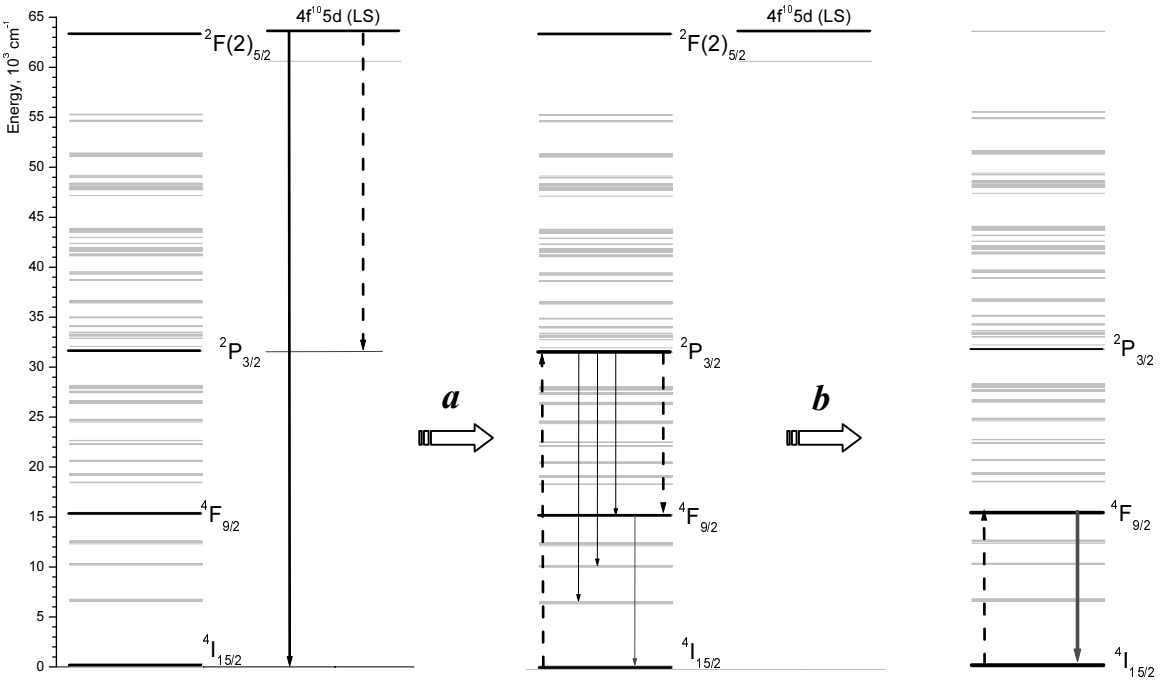

Figure 4.35: *Scheme of possible cross-relaxation processes in $LiYF_4$:Er. Solid arrows denote observed radiative transitions, dashed ones indicate possible nonradiative processes.*

These processes are depicted schematically in Figure 4.35. First ion at the excited $4f^{10}5d$ (LS) state decays to the $^2P_{3/2}$ state while an adjacent unexcited ion is raised to the $^2P_{3/2}$ state. This cross-relaxation is regarded as a donor-acceptor transfer in that it depopulates the $4f^{10}5d$ (LS) states of the Er^{3+} system (process (*a*) in Figure 4.35). As a result of the cross-relaxation both ions will appear in the $^2P_{3/2}$ state which can decay radiatively (402 and 469 nm lines) or non-radiatively in the second stage of the cross-relaxation. In the second stage cross-relaxation on the same way removes the $^2P_{3/2}$ excitation through the $^4F_{9/2}$ level. Finally, radiative decay from the $^4F_{9/2}$ state to the ground state takes place (process (*b*) in Figure 3.35). In addition to the donor-acceptor process, a donor-donor transfer also occurs, in which an ion in the excited $4f^{10}5d$ (LS) state decays to the ground state while an adjacent ion is raised from the ground state to the $4f^{10}5d$ (LS) state.

4.5 The model of electronic relaxation in $LiYF_4:Er^{3+}$

From point of view of application as a scintillator or as a lamp phosphor for Hg-free discharge lamps, the central question concerns the population of the radiating levels following VUV excitation of *d*-levels. In order to systematize the data obtained in previous chapters the model of electronic relaxation in the studied system will be presented.

4.5.1 Excitation of the lowest HS- and LS-states

The simplest case concerns excitation of the lowest HS- and LS-states in crystals with the lowest concentration of Er^{3+} ions. Discussing only the population of the most intense emitting states at low temperature, such as the $^4S_{3/2}$ or the $^2P_{3/2}$ state (see Figure 4.22 - 4.23), two possibilities can be considered: (i) radiative cascades $4f^{10}5d\rightarrow$ higher $4f^{11}$ levels, accompanied by additional nonradiative intraconfigurational relaxation, or (ii) nonradiative interconfigurational relaxation of the type $4f^{10}5d\rightarrow 4f^{11}$, followed by a combination of radiative intraconfigurational cascades and nonradiative relaxation. The doping concentration and the temperature, however, strongly influence the electronic relaxation.

Primary excitation of the lowest high-spin state

In the case of the lowest HS state, none of the UV lines observed by Wegh [Weg98], who performed measurements under primary selective excitation of Er^{3+} ions into the $^2F(2)_{7/2}$ (54675 cm^{-1}) lying under HS $4f^{10}5d$ state*, are found. Moreover as one can see from Figure 4.18, $^2P_{3/2}$ emission is missing (only some shoulder is distinguishable around 400 nm and 470 nm). Based on this observation non-radiative interconfigurational relaxation into high *f*-levels was ruled out [Kha02]. Recent measurements performed with better statistic, however, demonstrate the presence of

* *similar measurements were performed in this work as well and the perfect agreement with [Weg98] was obtained.*

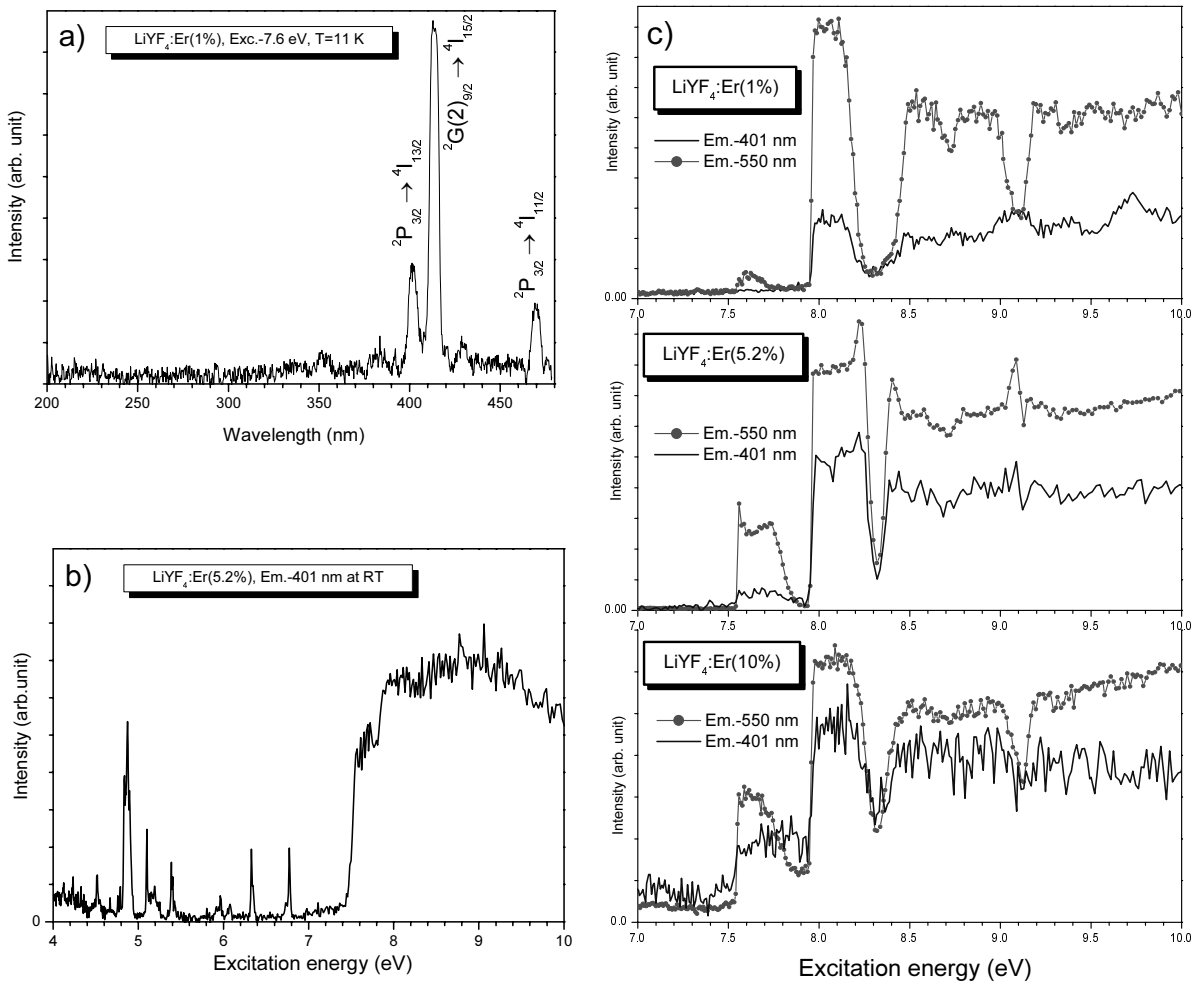

Figure 4.36: *a) Emission spectrum of the $LiYF_4$:Er(1%) sample under 7.6 eV excitation at 10 K; b) Excitation spectrum of the $^2P_{3/2} \rightarrow {}^4I_{13/2}$ (401 nm) emission in $LiYF_4$:Er(5.2%) crystal measured at room temperature using a LiF filter to exclude the second order effect; c) Excitation spectra monitoring the $^4S_{3/2} \rightarrow {}^4I_{15/2}$ (550 nm) and the $^2P_{3/2} \rightarrow {}^4I_{13/2}$ (401 nm) emission measured at 9.5 K in crystals with different doping concentration.*

the weak emission from $^2P_{3/2}$ and $^2G(1)_{9/2}$. As it is an essential point concerning relaxation mechanisms, additional discussion is required. The emission spectrum of the $LiYF_4$:Er(1%) sample under 7.6 eV excitation is shown in Figure 4.35a. The total intensity of the peaks depicted in Figure 4.36a amounts to less than 2% of the $^4S_{3/2}$ emission (not shown in the figure). The faint signal around 400 nm in Figure 4.18 (7.6 eV excitation) resolves into contribution from the $^2P_{3/2}$ and the $^2G(2)_{9/2}$ states. Hence, there is a good agreement between two spectra. As both curves were obtained without

filters blocking higher orders of the exciting radiation it is reasonable to ascribe the population of the $^2P_{3/2}$ and the $^2G(2)_{9/2}$ states to a higher order effect of excitation.

The situation becomes more complicated taking into account the temperature and concentration dependence of the $^2P_{3/2}$ ($^2G(2)_{9/2}$) population. The influence of the temperature is demonstrated in Figure 4.36b. The excitation spectrum of the $^2P_{3/2} \rightarrow {}^4I_{13/2}$ (401 nm) emission in $LiYF_4$:Er(5.2%) crystal (Figure 4.35b) was measured at room temperature using a LiF filter to exclude the second order effect. One can easily see that at room temperature the $^2P_{3/2}$ emission can be efficiently excited with 7.6 eV photons. Taking into account that the $^2P_{3/2}$ is definitely not populated via radiative transition from the HS state and that the HS state is well separated in energy both from the $^2F(2)_{5/2}$ state (~2250 cm^{-1}) and the $^2D(2)_{3/2}$ state (~6000 cm^{-1}) what excludes the nonradiative relaxation (at given temperature), one can expect that the cross-relaxation process is responsible for the population of the $^2P_{3/2}$.

Furthermore, the influence of the doping concentration is shown in Figure 4.36c. Excitation spectra monitoring the $^4S_{3/2} \rightarrow {}^4I_{15/2}$ (550 nm) and the $^2P_{3/2} \rightarrow {}^4I_{13/2}$ (401 nm) emission measured at 9.5 K in crystals with different Er^{3+} concentration are shown together (spectrum for the 402 nm emission in $LiYF_4$:Er(5.2%) is also measured using LiF filter). Although absolute intensity degreases with the raise of the concentration, the relative HS excitation (7.6 eV) efficiency of the $^2P_{3/2}$ emission increases with the doping concentration confirming the presence of the cross-relaxation channel of the $^2P_{3/2}$ state population.

It is difficult to single out one dominant cross-relaxation channel due to the large number of intermediate levels involved and the fact that phonons can be absorbed or emitted to conserve energy. However, from the inspection of the energy level scheme (Figure 4.3) one can expect

$$(4f^{10}5d\,(\mathrm{HS}),\ {}^4I_{15/2}) \rightarrow ({}^4G_{7/2}({}^4G_{9/2},\ {}^4G_{11/2}),\ {}^2K_{13/2}({}^2P_{1/2},\ {}^4G_{5/2}))$$

and $$(4f^{10}5d\,(\mathrm{HS}),\ {}^4I_{15/2}) \rightarrow ({}^2H(2)_{9/2},\ {}^4G(1)_{9/2})$$

or $$(4f^{10}5d\,(\mathrm{HS}),\ {}^4I_{15/2}) \rightarrow ({}^4G(1)_{9/2},\ {}^2H(2)_{9/2}).$$

Moreover, the cross-relaxation depopulating the HS state shows also up in luminescence decay measurements. Respective decay kinetics reveal the exponential decay accompanied with the considerable shortening of the decay time, which gradually varies from 1.92 μs in case of $LiYF_4$:Er(5%) to 1.1 μs in case of

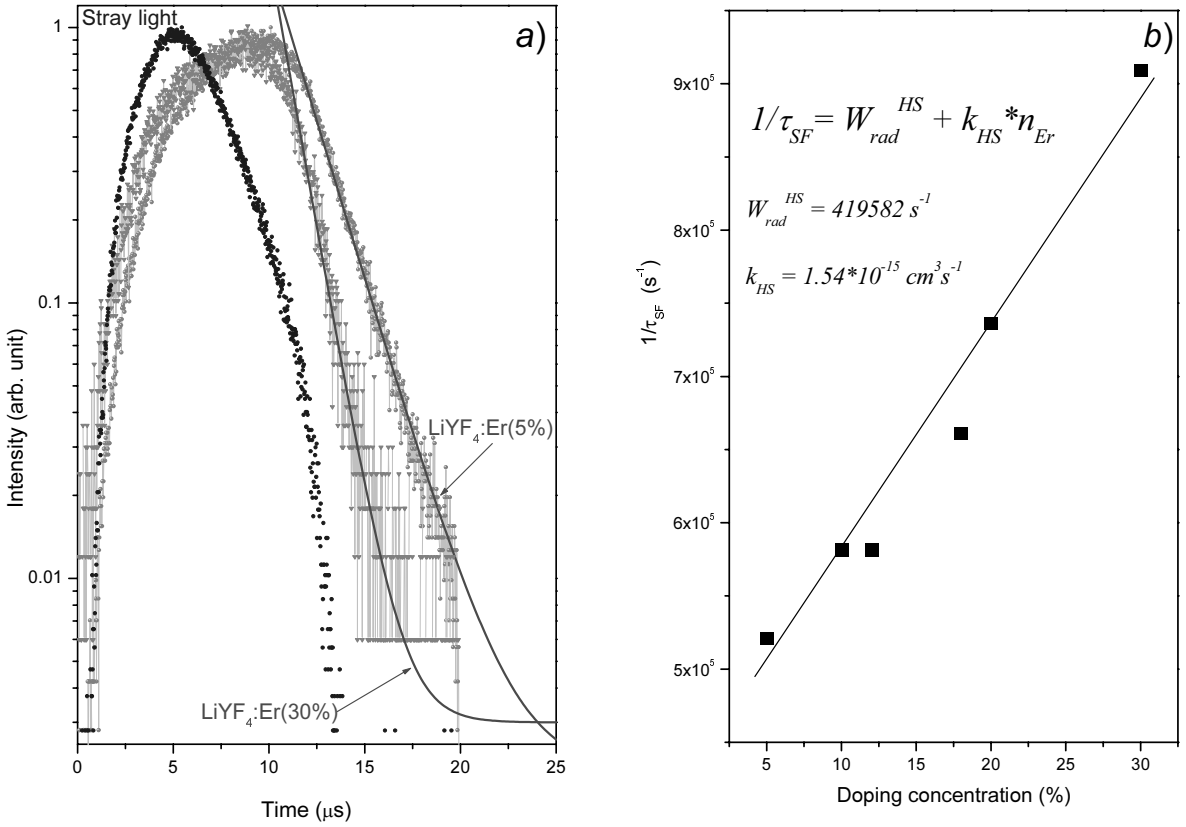

Figure 4.37: *a) Decay curves for SF d-f luminescence in $LiYF_4$:Er(5%) and in $LiYF_4$:Er(30%) under 7.7 eV excitation at T=9 K. For comparison the instrumental time-response is shown. Dots are experimental points, lines represent the results of exponential fitting; b) SF luminescence decay probability as a function of doping concentration. Line represents a fit of the experimental data. Respective fitting parameters are given in the figure.*

$LiYF_4$:Er(30%). In Figure 4.37a the decay kinetics of the SF *d-f* luminescence peaking at 165 nm in $LiYF_4$:Er(5%) and in $LiYF_4$:Er(30%) are shown. The measurements were performed under synchrotron radiation with a fast mechanical chopper. The instrumental time-response is shown as well. A deconvolution procedure was not performed. The growing part of the decay curves is connected with the excitation mode (note the shape of the response pulse).

The total decay probability can be considered as a sum of the radiative decay probability and the probability of the cross-relaxation process, which expected to be responsible for the shortening of the decay kinetics:

$$1/\tau_{SF} = W_{rad}^{HS} + W_{cr}^{HS} = W_{rad}^{HS} + k_{HS} \cdot n_{Er} \,. \qquad (4.21)$$

Then from the $1/\tau_{SF}(n_{Er})$ dependency (Figure 4.37b) the radiative lifetime of the HS $4f^{10}5d$ state $\tau_{rad}(HS)$ and the cross-relaxation coefficient k_{HS} can be roughly estimated, resulting in values 2.38 μs and $1.5 \cdot 10^{-15}$ cm^3 s^{-1} respectively.

The next possibilities for the energy relaxation are radiative cascades. Starting from the HS state, besides the ground state and the $^4I_{13/2}$ state (which would emit outside the spectral range investigated here), also the $^4I_{11/2}$ state, the $^4F_{9/2}$ and the $^4S_{3/2}$ / $^2H_{11/2}$ states are populated by radiative transitions (see Table 4.1 and Figure 4.4c). Figure 4.4c shows that most pronounced sidebands of the "slow" emission are those terminating at $^4I_{13/2}$, $^4S_{3/2}$ / $^2H_{11/2}$ and at $^4F_{3/2,\ 5/2}$. The $^2H_{11/2}$ and the $^4F_{3/2,\ 5/2}$ states will contribute to the $^4S_{3/2}$ state via nonradiative relaxation. Moreover, since $^2H_{11/2}$ and $^4S_{3/2}$ as well as the $^4F_{3/2}$ and $^4F_{5/2}$ levels are thermally coupled with each other they are usually treated as combined levels with a Boltzmann population distribution [Pol95]. The *f*-levels between the $^2P_{3/2}$ state and the $^2F(2)_{5/2}$ state are nearly not involved in the relaxation at all. It seems reasonable that radiative transitions of the HS state are the dominating source of population of $^4S_{3/2}$ which then shows up in emission.

Since the $^4G_{7/2}$ (28165 cm^{-1}, just under $^2P_{3/2}$) level was populated, different mechanisms of relaxation were studied from the point of view of laser action from the lower lying levels [Pol94, Pol95, Tka90, Tka85, Per83, Mor75, Auz94, Pet78, Orl94]. Based on this investigations one can deduce the following possible reasons for the occurrence of very intense $^4I_{11/2}$ emission at higher doping concentration and elevated temperatures: (i) a redistribution of the excitation from the $^4S_{3/2}$ and $^2H_{11/2}$ levels to $^4I_{11/2}$ due to the cross-relaxation processes of type

$$(^4S_{3/2} + {}^2H_{11/2},\ ^4I_{15/2}) \rightarrow (\ ^4I_{9/2},\ ^4I_{13/2})$$ [Lut91, Pol94] and

$$(^2P_{3/2},\ ^4I_{15/2}) \rightarrow (^2H(2)_{11/2},\ ^4I_{9/2})$$ (section 4.3.3)

with subsequent multiphonon decay $^4I_{9/2} \rightarrow {}^4I_{11/2}$; (ii) longest lifetime of the $^4I_{11/2}$ among all higher lying levels in combination with a low branching ratio from $^4I_{11/2}$ to $^4I_{13/2}$ [Qui89].

Primary excitation of the lowest low-spin state

In this case, additionally to the $^4S_{3/2}$ emission, the strong $^2P_{3/2}$ emission is 'switched on'. The absence of the UV lines corresponding to *f-f* transition indicates that relaxation along the *f*-ladder is not responsible for the population of the emitting states. The most prominent emitting state $^4S_{3/2}$ is reached via radiative decay of the lowest LS state (see Table 4.1 and Figure 4.4b). The $^2P_{3/2}$ state, however, is definitely not excited via a radiative cascade. As one can see from the decay kinetics measurements (section 4.4), the energetic position of the $^2P_{3/2}$ state halfway in-between the ground state and the lowest LS state favours cross-relaxation of the type ($4f^{10}5d$ (LS), $^4I_{15/2}$) → ($^2P_{3/2}$, $^2P_{3/2}$). This process is the only simple explanation for the population of the $^2P_{3/2}$ state following primary excitation of the lowest $4f^{10}5d$ LS state. Further processes leading to devastation of the $^2P_{3/2}$ are radiative decay to the $^4I_{13/2}$ (401 nm), $^4I_{11/2}$ (470 nm) and $^4F_{9/2}$ (620 nm) or cross-relaxation of the type ($^2P_{3/2}$, $^4I_{15/2}$) → ($^4F_{9/2}$, $^4F_{9/2}$) which becomes more favourable with increase of doping concentration.

In addition, on the basis of the decay analysis one can roughly estimate a contribution of various processes responsible for the devastation $4f^{10}5d$ LS state of the Er^{3+} ion in $LiYF_4$. In the simplest case, when the decay times are evaluated from the single exponential decay curve fitting*, the total decay from the $4f^{10}5d$ LS state can be written as:

$$\frac{1}{\tau} = W_{rad}^{LS} + W_{nr}^{LS} = W_{rad}^{LS} + W_{cr} + W_D + W_{ISC} + W_{d-f} \ . \qquad (4.22)$$

Simple substitution of the already calculated parameters in formula (4.22) yields the values of the cross-relaxation rates. The final results for the crystals with different Er^{3+} concentration are represented schematically in Figure 4.38. At low doping concentrations the most probable relaxation channels is non-radiative transitions to the nearest low lying states. As it is expected, the probability of the cross-relaxation process rises gradually with increasing Er^{3+} concentration. The donor-donor transfer is very low efficient at low temperatures because of the Stokes shift between *f-d* absorption and *d-f* emission. Hence W_D amounts to only few percents from the total

*In this case the decay time was evaluated as an area under respective decay curves, normalized to 1.

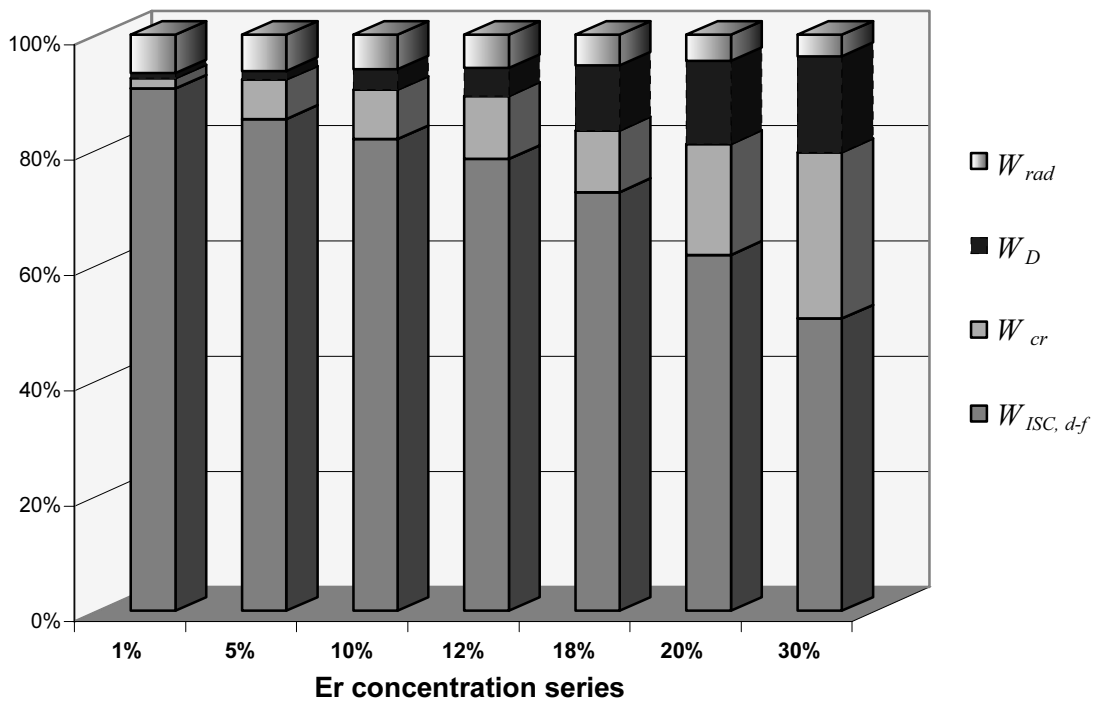

Figure 4.38: *Contribution of various processes responsible for the depletion of the Er^{3+} $4f^{10}5d$ LS state in $LiYF_4$ at T=10 K.*

decay probability in highly concentrated $LiYF_4$:Er(30%) crystal. At higher temperatures overlapping is larger, and donor-donor transfer becomes more efficient.

It should be noted, however, that taking into account discussion in section 4.4.4, results represented in Figure 4.38 give a very rough estimation of the percentage of various processes responsible for the depletion of the Er^{3+} $4f^{10}5d$ LS state.

4.5.2 Higher excitation energies within the transparency range of the host

The simplest model of electronic relaxation following primary $4f^{10}5d$ excitation with higher photon energies still within the transparency range of the host includes two steps, (i) rapid electronic relaxation to the lowest $4f^{10}5d$ states, and (ii) branching into the different relaxation channels as described above. Then, however,

the branching between the different emission lines and bands should be independent of photon energy of excitation. The excitation spectra shown in Figures 4.10 and 4.21 are a clear proof that this simple model is wrong. There is definitely interaction between the high *f*-levels and the high *d*-excitations bringing about pronounced resonances in favour of particular decay channels. The different behaviour of excitation spectra for the *d-f* and *f-f* emissions shows that the relaxation into the *f*-states can occur without passing through the *d*-states. The recent calculations of the respective energy levels by van Pieterson *et al.* [Pie01] do not cover the energetic range under discussion. Moreover, it was shown that considerable mixing of the *d*- and *f*-states occurs complicating the analysis of the relaxation processes. It seems a worthwhile goal to extend these calculations to higher excitation energies.

The charge-transfer as well as the autoionisation states can be involved into the energy relaxation processes in the 10-11 eV spectral range as it was described in section 4.2.

4.5.3 Host excitation below threshold of inelastic electron scattering

The dominant electronic relaxation channel in ionic crystals following primary host excitation (below threshold of inelastic scattering of photoelectrons) is formation of self-trapped excitons [Son93]. It was shown by van der Kolk et al. [Kol01] that self-trapped excitons can be an efficient intermediate state concerning host-guest energy transfer in RE^{3+} doped systems. The transfer efficiency, however, depends on the amount of spectral overlap between STE-emission and guest absorption. The studies of the STE luminescence in nominally pure $LiYF_4$ show that the maximum of STE emission is at ~ 4.6 eV. There is no overlap with the Er^{3+} *f-d* excitations. This can account for the absence of *d-f* emission following the host excitation. On the other hand, there is overlap with *f-f* excitations. Consequently, *f-f* transitions can be observed in the luminescence. Experimental results show that in this way also these *f*-states are populated which can be directly excited by the photons with sufficiently low energy. Therefore, the respective UV lines also show up in the luminescence spectra following host excitation.

4.5.4 Host excitation at higher photon energies

Primary excitation far up into the conduction band results in free electron-hole pairs. Depending on the photon energy of excitation, the electrons may have sufficient kinetics energy to create additional electronic excitations in inelastic scattering processes. These processes have been systematically investigated, e.g., by Lushchik et al. [Lus96] for alkali halide crystals. As already mentioned above, these ideas can also be applied to explain how a dopant in an ionic host is excited [Mak00]. Above the threshold energy, excitation of Er^{3+} ions in a host crystal occurs via inelastic scattering of photoelectrons (also called 'impact excitation') which can be as selective as photon excitation. Well above the threshold, in the energy range of 50-200 eV, the kinetics energy of the electrons is sufficient to excite Er^{3+} ions not only to the lowest but also higher $4f^{10}5d$ states. In other words, all the peculiarities in the branching between different luminescence channels showing up in photoluminescence excitation spectra, will be washed out. This is the reason why the ratio between the luminescence yield of *d-f* and *f-f* emission (Figure 4.17) is nearly independent of photon energy of excitation. The tendency of increase towards smaller photon energies of excitation is in agreement with the fact that the intensity of the *d-f* emission itself will go to zero, whereas the *f-f* emission intensity will reach a finite level below the threshold of inelastic scattering.

Chapter 5

Summary

The main purpose of the present work was a systematic spectroscopic characterization of $LiYF_4$ doped with Er^{3+} with an attempt to analyse the electronic relaxation. The examinations were focused on the energy transfer processes between the Er^{3+} ions leading to the optical transitions. The influence of the different parameters such as temperature, doping concentration and initial excited state was treated to provide complementary information concerning the electronic relaxation.

The $LiYF_4:Er^{3+}$ system exhibits intense VUV emission due to the inter-configurational $4f^{10}5d$-$4f^{11}$ transition. Both the spin-allowed and the spin-forbidden *f-d* emission of Er^{3+} were monitored. Transition from the high-spin state $4f^{10}5d$ configuration to the ground state is observed as a band with maximum at 165 nm. Because of the spin-forbidden character of the transition, this emission has a decay time of more than 2 μs. Transitions from the higher energetic quartet state are spin-allowed. The emission band corresponding to the transition to the ground state has a maximum at 157 nm and a decay time τ_0 = 84 ns. Careful time-resolved emission measurements allow to distinguish and assign a number of $4f^{10}5d$-$4f^{11}$ transitions, which have not analysed before.

The luminescence intensity and bandwidth of the spin-forbidden *5d–4f* emission of Er^{3+} were measured in wide temperature range from 6 to ~ 900 K. From the respective temperature dependencies the values of the phonon energy $\hbar\omega \approx 52$ meV (420 cm^{-1}) and an activation energy $\varepsilon_a = 0.60 \pm 0.03$ eV were estimated.

Besides the electronic relaxation of the $4f^{10}5d$ levels, the relaxation within the *f*-manifold was analysed. These emissions consist of sharp lines due to the strong

shielding of the *f*-orbitals from the crystal environment. Excitation spectra of the most intense emission bands were recorded and compared. Following selective excitation of the HS state around 7.6 eV, the $^4S_{3/2}\rightarrow{}^4I_{15/2}$ (550 nm) emission shows up, whereas the $^2P_{3/2}\rightarrow{}^4I_{13/2}$ (402 nm) emission is absent (only at room temperature, a slight signal is observed). Above 10 eV the $^2P_{3/2}\rightarrow{}^4I_{13/2}$ emission is strongly enhanced compared with the $^4S_{3/2}\rightarrow{}^4I_{15/2}$ emission. The excitation spectra of the $^4S_{3/2}\rightarrow{}^4I_{15/2}$ and $^2P_{3/2}\rightarrow{}^4I_{13/2}$ *f-f* emissions were compared with the excitation spectra of the spin-forbidden (165 nm) and spin-allowed (157 nm) *d-f* luminescence. For obvious reasons, the *d-f* emission can only be excited by *f-d* excitations whereas the *f-f* emission can also be excited via *f-f* excitations. In the excitation spectrum of the $^4S_{3/2}\rightarrow{}^4I_{15/2}$ emission, the lowest $4f^{n-1}5d$ HS state at 7.55 eV (energetic position of the zero-phonon line), which is well separated from the LS-state, can be clearly observed. Above 10 eV, striking differences are observed. Maxima in the *f-f* excitation spectra correspond to minima in the *d-f* excitation spectra and vice versa. Such a different behaviour of the *f-f* and *d-f* emission arises from the different excitation mechanisms. The charge transfer excitations of the type $F^-\rightarrow Er^{3+}$ and autoionisation processes were discussed as possible candidates to populate *f*-levels. The contribution of the excitonic absorption into the population of *f*-states was studied as well. The investigation of the nominally pure $LiYF_4$ gave information about the electronic states of the host matrix. The reflection spectrum of $LiYF_4$:Er has shown a pronounced peak at 11.65 eV, which was ascribed to an excitonic host excitation. Then, the band gap energy and the binding energy of the exciton were estimated to be 12.4 eV and 0.75 eV, respectively.

In addition, some experimental results concerning $LiYF_4$:Er system under inner-shell excitation were discussed with an attempt to trace the relaxation processes in this system after excitation with the energies much higher than the band-gap.

The gradual redistribution between emission bands following the change of the excitation energy observed in this work shows that the initial excited state is an essential parameter influencing electronic relaxation. It was concluded that $^4S_{3/2}$ and $^2P_{3/2}$ levels are populated through different channels, and possible energy transfer processes leading to the population of these levels were discussed.

The occurrence of energy transfer between two optically active centers can significantly affect the luminescence properties of a material. As the probability of the energy transfer depends on doping concentration, the qualitative alterations of the

luminescence following changes of the concentration were investigated. An analysis of the concentration dependency of the Er^{3+} *5d–4f* emission has been performed. Dramatic energy redistribution in the visible and infrared part of the emission spectra concerned with the change of the concentration was studied and discussed as well.

Experimental decay times of the Er^{3+} spin-allowed luminescence as a function of doping concentrations were obtained through the measurement of the decay curves. For the treatment of the data, different models were used. An analysis of the decay kinetics in a quantitative way was represented. The combination of the independently obtained data sets concerning luminescence intensity and decay kinetics measurements yields a number of important parameters describing electronic relaxation in the given system such as migration-assisted energy transfer rate between donors W_D, microparameters C_{DA} and C_{DD}, critical acceptor concentration C_k and the radiative decay time τ_{rad}.

Finally, to systematize all the data obtained in this work, a model of electronic relaxation in the given system was proposed.

Appendix A

Software used at the experiment

As was already mentioned, the Princeton Instruments LN/CCD detector system was used for collecting luminescence data. The system is controlled by an additional computer with the preinstalled WinSpec program operating under the Microsoft Windows system. The WinSpec is a high performance software package written specially for acquisition and analysis of images using Princeton Instruments cooled digital CCD cameras. A screenshot of the program is shown in Figure A1.

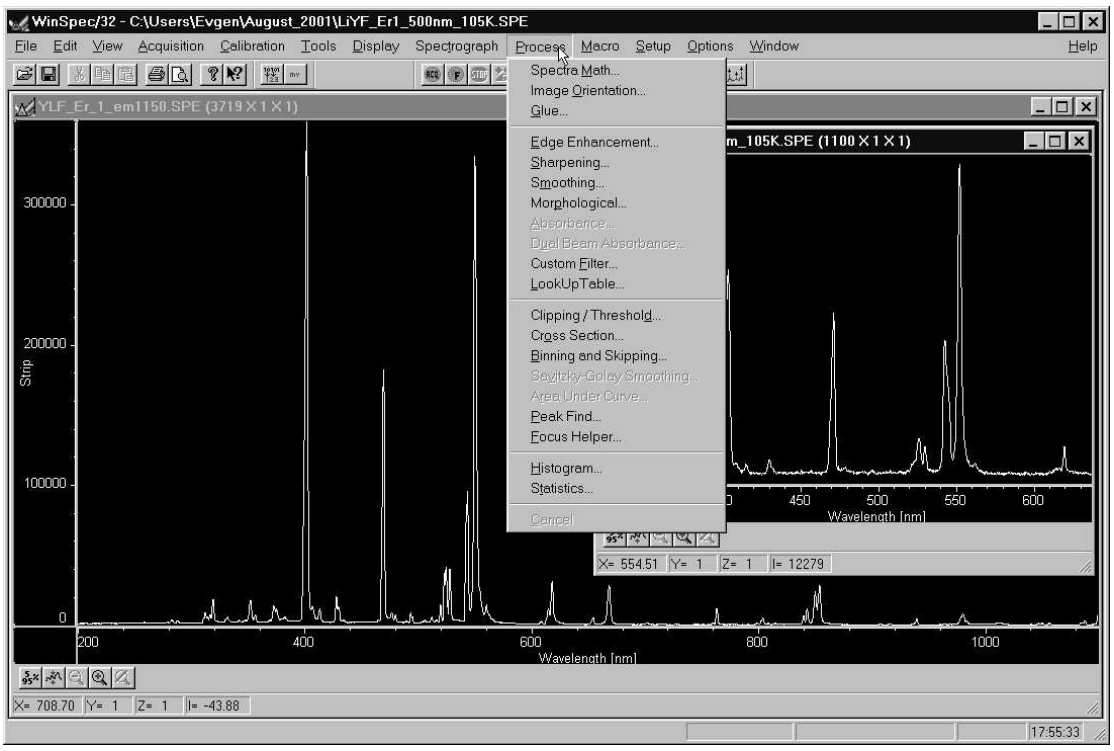

Figure A1: *Screenshot of the WinSpec program.*

As time resolved measurements in the UV-visible range are not possible with the CCD detector, a conventional photomultiplier is used. An additional program SpectraX was developed during my Ph.D. work to allow time resolved data acquisition and computer control of the ARC monochromator SpectraPro-308 (see screenshot in Figure A2) . The program operates under the Microsoft Windows system. SpectraX was developed using the graphical programming language LabVIEW . LabVIEW contains comprehensive libraries for data collection, analysis, presentation and storage. Due to the flexibility and performance of a programming, this software package is very convenient to build own solutions for specific scientific system. The appearance of the LabView programming interface is shown in Figure A3.

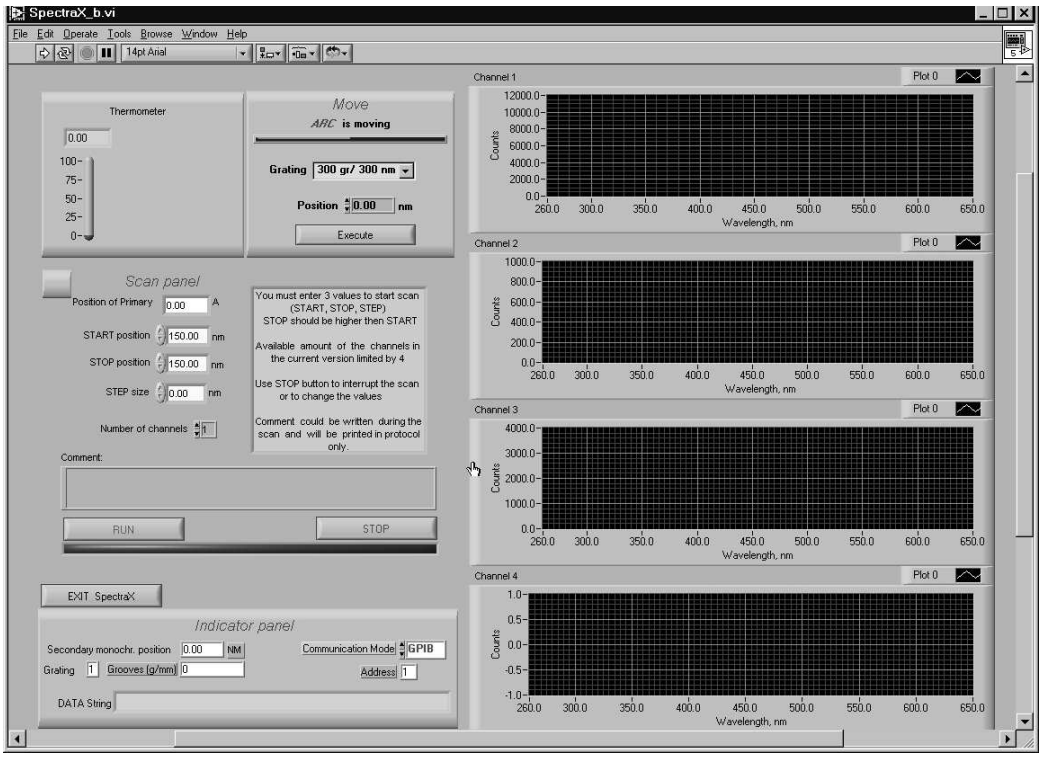

Figure A2: *Screenshot of the SpectraX program.*

In the future, an additional module enabling the temperature control of the sample holder, will be added. This upgrade allows to automate the procedure of the temperature control and helps significantly to simplify and quicken temperature dependent luminescence measurements.

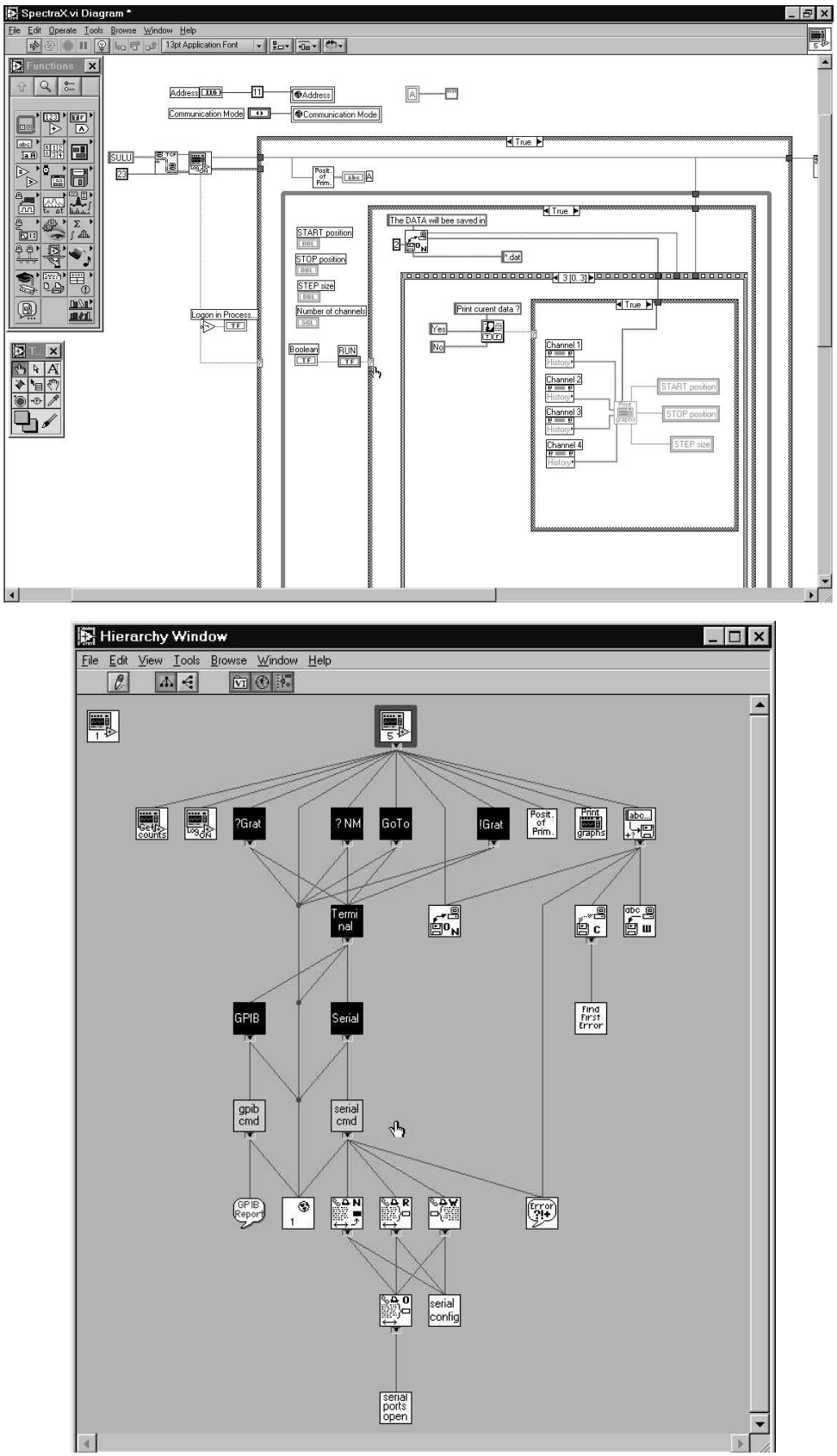

Figure A3: *Appearance of the LabView programming interface. Upper screenshot shows a diagramic view of SpectraX. The hierarchy of the program can be simultaneously monitored and corrected (lower screenshot).*

Appendix B

BW3 Experiment

Investigation of the $LiYF_4$:Er system under inner-shell excitation was not the main purpose of the present work, but an attempt to trace the relaxation processes in this system after excitation with the energies much higher than the band-gap was made. Some additional data obtained in the frame of this experiment are also interesting and therefore are represented here, but without any profound analysis.

The measurements under soft X-ray excitation were performed at the BW3 beamline of HASYLAB at DESY. BW3 is a state-of-the-art beamline for the 40-2000 eV photon energy region. It produces a high photon flux with a resolution better than or comparable to the natural line widths of the core levels in this region, making it well suited for core level spectroscopy.

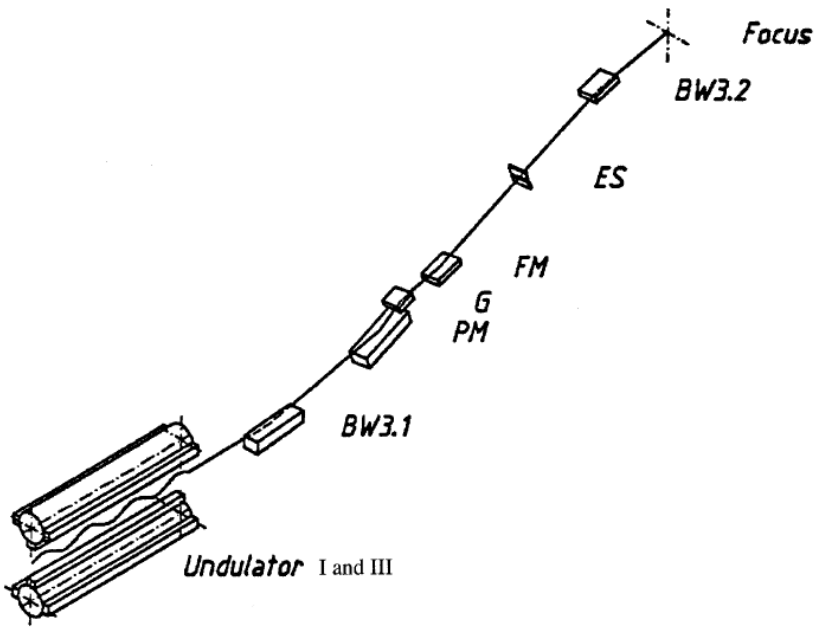

Figure B1: *Schematic representation of the BW3 beamline. See text for more details.*

The source of the beamline is a configuration of two interchangeable plane undulators mounted on a revolver type device. Together the first harmonics of the undulators cover the spectral range 40-1800 eV. The first optical element of the beamline is a water-cooled mirror (BW3.1, see Figure B1), with three interchangeable coatings, SiC, Au and SiO_2, for optimum reflectivity over the large photon energy range. The mirror deflects the radiation into a modified SX-700 plane grating monochromator built by Zeiss. It consists of a premirror (PM), a plane grating (G), and a spherical focusing mirror (FM), which focuses the light onto the exit slit (ES). The monochromator is equipped with two different gratings, which together cover the spectral range 40 eV - 2000 eV. All optical elements up to the focusing mirror (FM) are water cooled to avoid resolution degradation due to thermal deformation induced by the heat load from the undulator radiation.

Data acquisition and running of the beamline is performed with a LINUX computer through a CAMAC controller. Another feature of the software is that the undulator gap can be changed during monochromator scans. The resulting photon flux variations due to the finite step size are smaller than 1%. This enables co scanning of the undulator first harmonic and the monochromator photon energies.

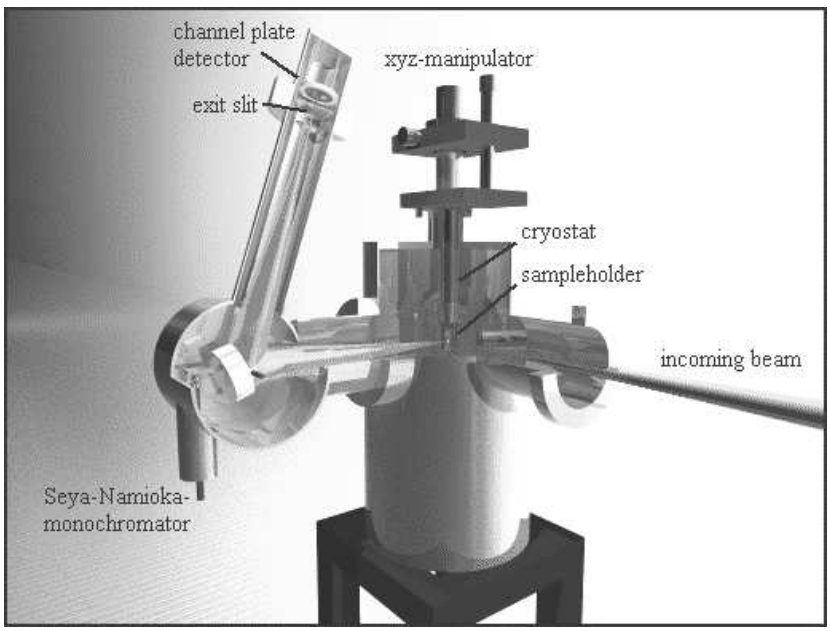

Figure B2: *Homemade experimental chamber (designed by S. Vielhauer) for the mounting at the beamline BW3.*

Monochromatized light from the exit slit is refocused by an ellipsoidal mirror (BW3.2) into a spot of about 150 μm in diameter at the sample position. Behind the refocusing mirror different experimental endstations can be connected to the beamline on a platform.

In this work the experimental chamber designed by S. Vielhauer [Vie03] was used (see Figure B2). The chamber is provided with a 0.4 m Seya-Namioka monochromator. The monochromator is equipped with a holographicaly corrected Jobin-Yvon grating with 1200 grooves per mm and covering spectral range from 30 up to 500 nm. Luminescence is measured by a fast (≈ 400 ps FWHM) open micro-channel plate detector or by a conventional photomultiplier. The typical spectral resolution is approximately 10 Å. The samples are mounted on the sample holder attached to a flow type liquid He cryostat enabling measurements in the temperature range from 6 K to 350 K.The energy range of excitation was 40-800 eV.

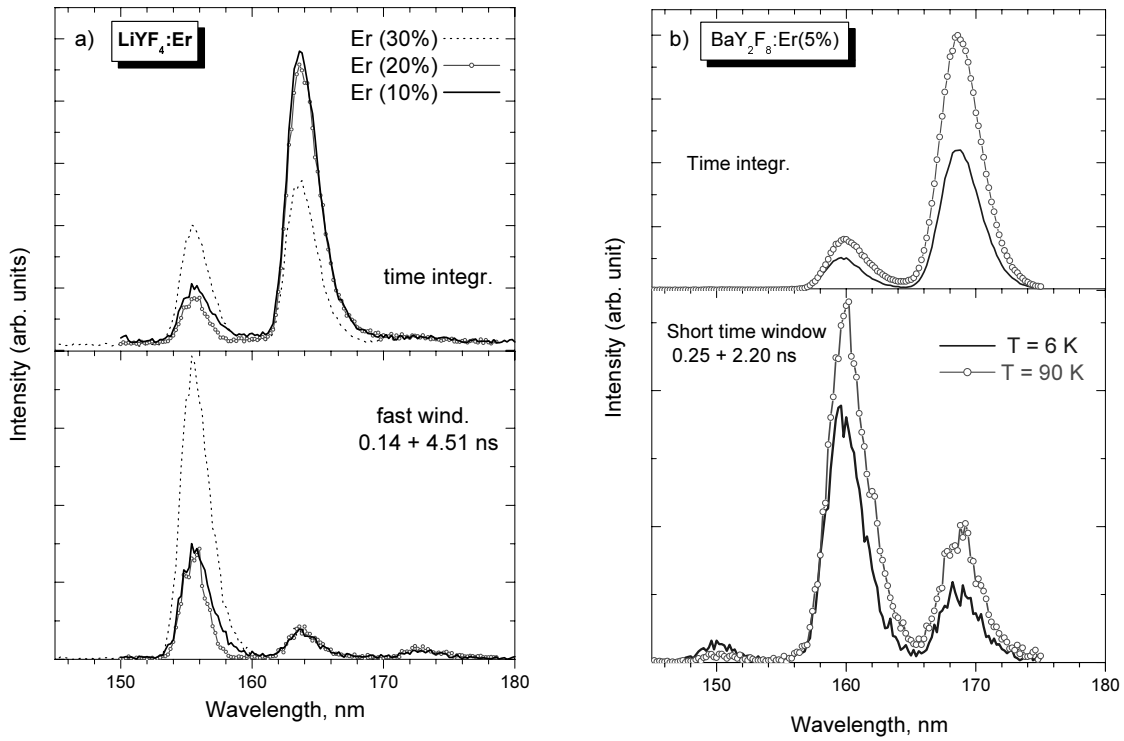

Figure B3: *a) d-f luminescence spectra of Er^{3+} in $LiYF_4$ with different doping concentration under 150 eV excitation at T=10 K; b) d-f luminescence spectra measured at different temperatures in BaY_2F_8:Er(5%) crystal under 150 eV excitation. In both cases time-integrated and time-resolved (short time window) spectra are shown.*

The results of time-resolved emission spectra measurements for $LiYF_4$:Er with different doping concentration under 150 eV excitation are shown in Figure B3a. Although concentration quenching leads to a decrease of the total quantum yield of *d-f* luminescence, the quantum yield of the fast spin-allowed component increases with the concentration of Er^{3+}.

Previously unknown weak emission band (Figure B3b) at 150 nm, above the well-known S-A transition (160 nm), was detected in BaY_2F_8:Er(5 %) crystal at 10 K. The decay of this emission is faster than that of the S-A transition and cross-luminescence, and lies in the sub-nanosecond range. This emission is very weak, being thermally quenched at 90 K. At the moment, the origin of this band is not clear. Possibly, it can be the emission from the higher *d*-state or from the *d*-state of Er^{3+} ions situated in sites with different symmetry.

The decay kinetics for the spin-allowed transitions in $LiYF_4$:Er are shown in Figure B4. Even in case of low-doped systems one can clearly see that the decay has non-exponential character. Moreover, the total decay probability of the spin-allowed emission excited with soft X-rays is higher than in case of excitation with VUV photons (see Chapter 4.4). The decay time for fast spin-allowed luminescence (singe exponential fit) varies from 2.86 ns in $LiYF_4$:Er(5%) to 1.95 ns in $LiYF_4$:Er(30%).

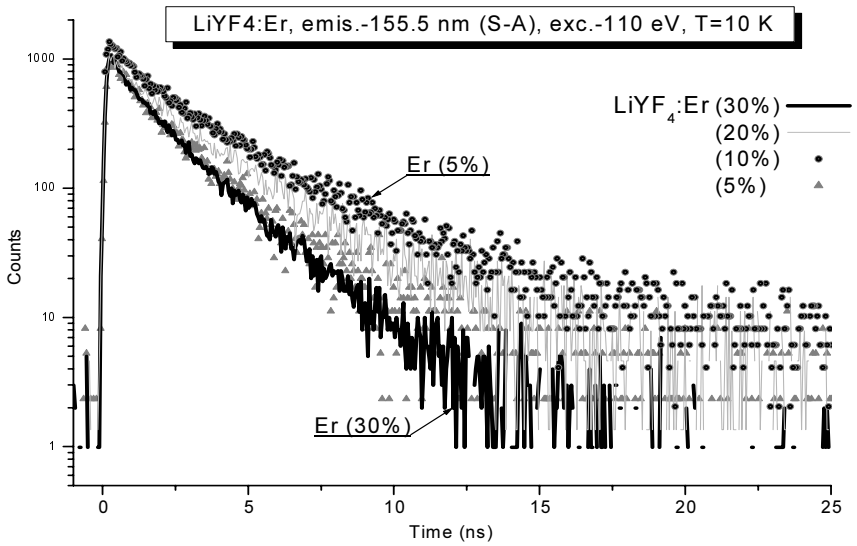

Figure B4: *Decay curves of spin-allowed 5d-4f luminescence of Er^{3+} in $LiYF_4$ with different doping concentration under 110 eV excitation at T=10 K.*

Appendix C

In the following Appendix the experimental values of the Er^{3+} energy levels in $LiYF_4$ host are given. They are deduced from several sources: [Jay89, Cou98, Weg99]. Positions of the $4f^{10}5d$ levels were taken from this work.

$^{2S-1}L_J$ level	$\lvert M_J \rvert$	E_{exp} (cm^{-1})
$^4I_{15/2}$	5/2	0
	15/2	17
	3/2	28
	1/2	57
	9/2	255
	7/2	290
	11/2	320
	13/2	355
$^4I_{13/2}$	1/2	6540
	3/2	6545
	13/2	6585
	7/2	6680
	5/2	6704
	9/2	6731
	11/2	6745
$^4I_{11/2}$	1/2	10213
	3/2	10230
	5/2	10290
	7/2	10300
	11/2	10309
	9/2	10327
$^4I_{9/2}$	9/2	12364
	3/2	12486
	7/2	12540
	5/2	12568
	1/2	12663

$^{2S-1}L_J$ level	$\|M_J\|$	E_{exp} (cm^{-1})
$^4F_{9/2}$	9/2	15307
	3/2	15325
	1/2	15341
	7/2	15416
	5/2	15469
$^4S_{3/2}$	3/2	18433
	1/2	18492
$^2H(2)_{11/2}$	5/2	19 152
	7/2	19 172
	9/2	19224
	11/2	19309
	1/2	19326
	3/2	19342
$^4F_{7/2}$	5/2	20571
	7/2	20573
	3/2	20662
	1/2	20671
$^4F_{5/2}$	5/2	22255
	3/2	22279
	1/2	22304
$^4F_{3/2}$	3/2	22622
	1/2	22653
$^2G(1)_{9/2}$	9/2	24531
	3/2	24610
	7/2	24645
	5/2	24703
	1/2	24756
$^4G_{11/2}$	5/2	26393
	7/2	26394
	9/2	26458
	11/2	26558
	1/2	26611
	3/2	26624
$^4G_{9/2}$	5/2	27454
	7/2	27462
	9/2	27532
	3/2	27560
	1/2	27571

$^{2S-1}L_J$ level	$\lvert M_J \rvert$	E_{exp} (cm^{-1})
$^2K_{15/2}$	3/2	-
	1/2	-
	15/2	27844
	5/2	-
	7/2	-
	13/2	27987
	11/2	-
	9/2	-
$^4G_{7/2}$	1/2	28132
	5/2	28156
	3/2	28165
	7/2	-
$^2P_{3/2}$	3/2	31585
	1/2	31651
$^2K_{13/2}$	1/2	32873
	3/2	-
+	13/2	33078
$^2P_{1/2}$	1/2	-
	5/2	33150
+	7/2	-
$^4G_{5/2}$	3/2	-
	11/2	33272
	9/2	-
	1/2	33450
	5/2	-
$^4G_{7/2}$	7/2	-
	5/2	34074
	3/2	34153
	1/2	34185
$^2D_{5/2}$	5/2	34930
	1/2	34994
	3/2	35019
$^2H(2)_{9/2}$	9/2	36401
	7/2	36503
	5/2	-
	3/2	36558
	1/2	36684

$^{2S-1}L_J$ level	$\lvert M_J \rvert$	E_{exp} (cm^{-1})
$^4D_{5/2}$	5/2	38685
	1/2	-
	3/2	-
$^4D_{7/2}$	3/2	-
	1/2	39340
	5/2	39431
	7/2	39552
$^2I_{11/2}$	3/2	41125
	1/2	41145
	7/2	41205
	5/2	-
	9/2	41285
	11/2	41336
$^2L_{17/2}$	3/2	41598
	1/2	-
	5/2	41725
	7/2	-
	9/2	41758
	11/2	41830
	13/2	-
	15/2	41902
	17/2	41951
$^4D_{3/2}$	3/2	42375
	1/2	42410
$^2P_{3/2}$	1/2	42898
	3/2	-
$^2I_{13/2}$	9/2	-
	3/2	43526
	5/2	43640
	7/2	43649
	11/2	-
	1/2	43796
	13/2	43886
$^4D_{1/2}$	1/2	$\sim 47200^*$
$^2L_{15/2}$	3/2	-
	1/2	47783
	15/2	47856
	5/2	-

$^{2S-1}L_J$ level	$\lvert M_J \rvert$	E_{exp} (cm^{-1})
	7/2	47927
	13/2	47992
	11/2	-
	9/2	-
$^2H(1)_{9/2}$	9/2	48158
	7/2	48216
	5/2	48305
	3/2	-
	1/2	-
$^2D(2)_{5/2}$	5/2	49039
	1/2	49063
	3/2	49188
$^2H(1)_{11/2}$	11/2	51078
	9/2	-
	7/2	51209
	5/2	51327
	3/2	-
	1/2	-
$^2F(2)_{7/2}$	7/2	54696
	5/2	54723
	3/2	54746
	1/2	54780
$^2D(2)_{3/2}$	3/2	-
	1/2	55310
HS $4f^{10}5d$	-	61050
$^2F(2)_{5/2}$	5/2	~ 63300*
	3/2	-
	1/2	-
LS $4f^{10}5d$	-	~ 63694*
$^2G(2)_{7/2}$	-	65922

* *These approximate values are determined from emission.*

List of Figures

2.1 SUPERLUMI set-up 6
2.2 The incident photon flux on the sample 8
2.3 Schematic representation of operating of the MSP 12
2.4 Cross section of charge-coupled devise 14
2.5 Principal scheme for frontside-illuminated CCD 15
2.6 Comparison of front-illuminated and back-illuminated CCD 15
2.7 CCD mounting diagram 16
2.8 Signal-to-Noise ratio of the LN/CCD detector 17
2.9 Principal scheme for time-resolved luminescence measurements 20
2.10 The incident photon flux on the sample 22
2.11 Apparatus function for the ARC SpectraPro-308 monochromator with in connection with a CCD detector or with a photomultiplier 23

3.1 The scheelite structure of $LiYF_4$ 28
3.2 Schematic representation of the rare-earth ion energy levels splitting . . . 34
3.3 Energy level splitting for $LiYF_4:Er^{3+}$ 35
3.4 Illustration of the excited-state absorption 38
3.5 Temperature dependency of the non-radiative transition probability 39
3.6 Interionic processes 43
3.7 Calculated and measured excitation spectrum of $LiYF_4$:Er(2%) monitoring the $^4S_{3/2} \rightarrow {}^4I_{15/2}$ emission [Pie01] 52
3.8 Energy of the charge transfer band in fluorides and oxides 54

4.1 Time-integrated luminescence spectrum of $LiYF_4:Er^{3+}$(1%) at T=10 K . . 56
4.2 Schematic electron configurations for the ground low-spin and high-spin *f-d* states of Er^{3+} 57

4.3 Simplified energy level scheme of $LiYF_4:Er^{3+}$ 58
4.4 Time-resolved luminescence of $LiYF_4:Er^{3+}$(1%) at T=10 K 60
4.5 Luminescence of $LiYF_4$:Er(5%) under 150 eV excitation at 10 K 63
4.6 Set of the emission curves for $LiYF_4$:Er(5%) excited with 9 eV photons at different temperatures 65
4.7 Temperature dependence of the SF *5d–4f* luminescence bandwidth of $LiYF_4$:Er(5%) 66
4.8 a) Temperature dependence of the SF *5d–4f* luminescence intensity of $LiYF_4$:Er(5%);
b) Schematic configuration coordinate diagram of energy levels for Er^{3+} in $LiYF_4$ 67
4.9 High resolution emission spectrum of $LiYF_4$:Er(5%) at T=10 K under 10.8 eV excitation 69
4.10 Excitation spectra of selected luminescence bands of $LiYF_4:Er^{3+}$(1%) measured at T=9 K 71
4.11 Excitation and emission spectra monitoring the transition from the high-spin $4f^{10}5d$ state to the $4f^{11}$ground state $^4I_{15/2}$ 72
4.12 Configurational coordinate diagram for Er^{3+} in $LiYF_4$ 73
4.13 Excitation spectra of spin-allowed *5d-4f* luminescence for $LiYF_4:Er^{3+}$(5%), $LiYF_4:Er^{3+}$(20%) and $LiErF_4$ at 300 K 75
4.14 Ratio between the excitation spectra of *f-f* luminescence, monitoring the $^2P_{3/2}\rightarrow{}^4I_{13/2}$ transition, and excitation spectra of *d-f* luminescence, monitoring transition from the quartet $4f^{10}5d$ state to the ground state measured for $LiYF_4:Er^{3+}$(5%) at T=10 K 76
4.15 a) Excitation spectra monitoring the $^4S_{3/2} \rightarrow {}^4I_{15/2}$ and spin-forbidden *d-f* luminescence in $LiYF_4:Er^{3+}$(5%), measured at T=10 K, and the excitation spectrum monitoring intrinsic emission in the pure $LiYF_4$;
b) Excitation spectra monitoring the intrinsic and extrinsic emissions measured in the pure $LiYF_4$ at T=8 K;
c) Transmission spectrum of $LiYF_4$ at T=300 K (measured by E. Schultheiss, Giessen Physikalisches Institut, 1986) and reflection spectrum of $LiYF_4:Er^{3+}$(5%) measured at T=10 K 78
4.16 Energy scheme of exciton and free charge carrier recombination on rare earth ion involving autoionisation states 80

4.17 Excitation spectra of the spin-allowed *d-f* emission and $^2P_{3/2} \rightarrow {}^4I_{13/2}$ emissions of $LiYF_4:Er^{3+}$(5%) at T=10 K in the soft x-ray region 82

4.18 Luminescence spectra of $LiYF_4$:Er(1%) at T=8 K for different photon energies of excitation 84

4.19 Time-resolved luminescence of $LiYF_4:Er^{3+}$ as a function of Er^{3+} concentration for T=296 K under 10.8 eV excitation 85

4.20 a) Relative intensity of the spin-allowed $4f^{10}5d$ emission as a function of concentration at T=8 K and at room temperature;
b) simplified schematic energy level diagram for Er^{3+} in $LiYF_4$ showing various relaxation processes after *f-d* excitation 86

4.21 Excitation spectra for spin-allowed and spin-forbidden *d-f* luminescence at T=9 K 90

4.22 Luminescence of $LiYF_4:Er^{3+}$ as a function of Er^{3+} concentration at T=296 K under 10.8 eV excitation. 91

4.23 Luminescence of $LiYF_4:Er^{3+}$ as a function of Er^{3+} concentration at T=8 K under 10.8 eV excitation 92

4.24 Intensity of the $^2P_{3/2} \rightarrow {}^4I_{11/2}$ emission band as a function of the doping concentration at T=8 K and at room temperature 93

4.25 Luminescence of $LiYF_4$:Er(1%) at T=9 K and T=296 K; luminescence of $LiYF_4$:Er(30%) at T=9 K and T=296 K. Both under 4.86 eV excitation 95

4.26 Comparison of decay kinetics of the SA *d-f* luminescence of Er^{3+} for different doping concentration in $LiYF_4$, excited with 8.1 eV photons at T=10 K 97

4.27 Decay kinetics of the SA *d-f* luminescence of $LiYF_4$:Er(5%) crystal under 8 eV excitation at T=10 K. Dots are experimental points, solid line represents exponential decay. 99

4.28 Decay kinetics of the SA *d-f* luminescence for $LiYF_4$ crystals with different Er doping concentration. Dots are experimental points, curves represent results of the fitting within the Inokuty-Hiroyama model 100

4.29 Values of the γ parameter of the Inokuti-Hirayama model as function of Er concentration 101

4.30 Values of $1/\tau_{IH}$ as function of the doping concentration obtained from the fitting of the experimental decay curves within the Inokuti-Hiroyama model 103

4.31 Decay curves of SA *d-f* luminescence for $LiYF_4$:Er(5%) excited with 8.05 eV photons and measured at different temperatures 105

4.32 Decay curves of SA *d-f* luminescence for $LiYF_4$:Er(1%) and $LiYF_4$:Er(30%) under 8.05 eV excitation and measured at different temperatures. Respective fits are shown as solid lines 106

4.33 Luminescence of $LiYF_4$:Er at T=9 K as a function of Er concentration in enlarged scale 114

3.34 Relative intensity of the $^2P_{3/2} \rightarrow {}^4I_{13/2}$, $^2P_{3/2} \rightarrow {}^4I_{11/2}$ and $^4F_{9/2} \rightarrow {}^4I_{15/2}$ emission lines as a function of the doping concentration 115

3.35 Two steps cross relaxation model 115

3.36 a) Emission spectrum of the $LiYF_4$:Er(1%) sample under 7.6 eV excitation at 10 K;
b) Excitation spectrum of the $^2P_{3/2} \rightarrow {}^4I_{13/2}$ emission in $LiYF_4$:Er(5.2%) measured at room temperature using a LiF filter;
c) Excitation spectra monitoring the $^4S_{3/2} \rightarrow {}^4I_{15/2}$ and the $^2P_{3/2} \rightarrow {}^4I_{13/2}$ emission measured at 9.5 K in crystals with different doping concentration. 118

3.37 a) Decay curves for SF *d-f* luminescence in $LiYF_4$:Er(5%) and in $LiYF_4$:Er(30%) under 7.7 eV excitation at T=9 K;
b) SF luminescence decay probability as a function of doping concentration. Line represents a fit of the experimental data. Respective fitting parameters are given in the figure. 120

3.38 Contribution of various processes responsible for the devastation of the Er^{3+} $4f^{10}5d$ LS state in $LiYF_4$ at T=10 K. 123

A1 Screenshot of the WinSpec program 131

A2 Screenshot of the SpectraX program 132

A3 Appearance of the LabView programming interface (the diagram of the SpectraX and the hierarchy of the program) 133

B1 Schematic representation of the BW3 beamline. 135

B2 Homemade experimental chamber for the mounting at the beamline BW3. 136

B3 a) d-f luminescence spectra of Er^{3+} in $LiYF_4$ with different doping concentration under 150 eV excitation at T=10 K;
b) d-f luminescence spectra measured at different temperatures in BaY_2F_8:Er(5%) crystal under 150 eV excitation. In both cases time-integrated and time-resolved (short time window) spectra are shown . . . 137

B4 Decay curves of spin-allowed 5d-4f luminescence of Er^{3+} in $LiYF_4$ with different doping concentration under 110 eV excitation at T=10 K 138

List of Tables

2.1 Technical data of the monochromators at SUPERLUMI 10

2.2 Technical data of conventional photomultipliers at the SUPERLUMI set-up 11

2.3 Technical data of the microsphere plate (MSP). 13

2.4 Crystal data and physical properties of $LiYF_4$ host. 29

4.1 Assignment of $d \rightarrow f$ emission bands starting from the lowest HS and LS state 62

4.2 Decay kinetic fitting parameters obtained within the single exponential (τ) and the Inokuti-Hiroyama(τ_{IH}) models. 99

4.3 Fitting parameters obtained within the model described by Equation (4.18) 103

4.4 Calculated values of the microparameters C_{DA} and C_{DD} and the range parameters for donor-acceptor (R_o) and donor-donor (R_o^{DD}) energy transfer in LiYF4:Er system. 104

4.5 The values of C_{DA}, C_{DD} and R_0 obtained from the literature for interactions between two lanthanide ions in different host matrixes. 110

C Experimental values of the Er^{3+} energy levels in $LiYF_4$ host 139

Bibliography

[Ash76] N. W. Ashcroft and N. D. Mermin, *Solid-State Physics*, Saunders College, Philadelfia, International Edition (1976).

[Auz94] F. Auzel, Y. Chen, *Photon avalanche luminescence of Er^{3+} ions in $LiYF_4$ crystals*, Journal of Luminescence 65, 45-56 (1995).

[Bas96] T. T. Basiev, Yu. V. Orlovskii, Yu.S. Privis, *High-order multipole interaction in nanosecond Nd-Nd energy transfer*, Journal of Luminescence 69, 187-202 (1996).

[Bec98] J. Becker, J. Y. Gesland, N. Yu. Kirikova, J. C. Krupa, V. N. Makhov, M. Runne, M. Queffelec, T. V. Uvarova, and G. Zimmerer, *VUV emission of Er^{3+} and Tm^{3+} in fluoride crystals*, Journal of Luminescence 78, pp. 91 96 (1998).

[Bel99] A. N. Belsky and J. C. Krupa, *Luminescence excitation mechanisms of rare earth doped phosphors in the VUV range*, Displays, 19, pp. 185 196 (1999).

[Bla94] G. Blasse, B. C. Grabmaier, *Luminescent Materials*, Springer-Verlag Berlin Heidelberg (1994).

[Blo66] J. Blok and D. A. Shirley, *Systematic Variation of Quadrupole Crystal-Field Shielding in Rare-Earth Ethyl Sulfates*, Phys. Rev. 143, 278 (1965).

[Bri23] P. W. Bridgman, *The Compressibility of Thirty Metals as a funtion of pressure and temperature*, Proc. Amer. Acad. Arts Sci. 58, 165-242, 1923.

[Bur62] G. Burns, *Shielding and Crystal Fields at Rare-Earth Ions*, Phys. Rev. 128(5), 2121-2130 (1962).

[Bur72] A. I. Burshtein, Zh. Eksp. Teor. Fiz. 62, 1695 (1972), [Sov. Phys. JETP 35, 882 (1972)].

[Bur85] A. I. Burshtein, *Energy decay kinetics in disordered systems*, Journal of Luminescence 34, 167 (1985).

[Chi01] W. Y. Ching and Yong-Nian Xu, *Comparative study of the electronic structure of two laser crystals: $BeAl_2O_4$ and $LiYF_4$*, Phys. Rev. B, 63, 115101 (2001).

[Coo00] D. W. Cooke, B. L. Bennett, K. J. McClellan, J. M. Roper, and M. T. Whittaker, *Electron-lattice coupling parameters and oscillator strengths of cerium-doped lutetium oxyorthosilicate*, Phys. Rev. B, Vol. 61, pp. 11973-11978 (2000).

[Cou98] M. A. Couto dos Santos, E. Antic-Fidancev, J. Y. Gesland, J. C. Krupa, M. Lemaître-Blaise, and P. Porcher, *Absorption and fluorescence of Er^{3+}-doped $LiYF_4$: measurements and simulation*, J. Alloys Comp., 275-277, pp. 435 441 (1998).

[Cry73] Crystal data: Determinative tables, Vol. 2: Inorganic compounds, U. S. Department of Commerce, Washington (1973).

[Czo18] J. Czochralski, *Ein neues Verfahren zur Messung der Kristallisationsgeschwindigkeit der Metalle*, Z. Phys. Chemie 92, 219 (1918).

[Deb81] K. K. Deb, R. G. Buser, and J. Paul, Appl. Opt. 20, 1203 (1981).

[Dex53] D. L. Dexter, *A theory of Sensitized Luminescence in Solids*, J. Chem. Phys. 21,836 (1953).

[DiB84] B. DiBartolo, *Energy Transfer Processes in Condensed Matter,* p. 103, Plenum Press, New York (1984).

[Die78] G. H. Dieke, «*Spectra and Energy levels of Rare Earth Ions in Crystals*», John Wiley & Sons, New York (1978).

[Dor^{1}00] P. Dorenbos, *The $4f^n \leftrightarrow 4f^{n-1}5d$ transitions of the trivalent lanthanides in halogenides and chalcogenides*, J. Luminesc., 91, pp 91 106, (2000).

[Dor^{2}00] P. Dorenbos, *The 5d level positions of trivalent lanthanides in inorganic compounds*, J. Luminesc., 91, pp 111 176, (2000).

[Dor^{3}00] P. Dorenbos, *5d-level energies of Ce^{3+} and the crystalline environment. I. Fluoride compounds*, Phys. Rev.B, 62, pp. 15640 15649, 2000; *II. Cloride, bromide, and iodide compounds*, Phys. Rev.B, 62, pp. 15650-15659, (2000).

[Ein16] A. Einstein, *Strahlungs-Emission und –Absorption nach der Quantentheorie*, Verhandl. der Deutschen Physikalischen Gesellschaft 13/14, 317 (1916).

[Ein17] A. Einstein, *Zur Quantentheorie der Strahlung*, Phys. Z. 18, 121 (1917).

[Eli73] L. R. Elias, W. S. Heaps, and W. M. Yen, *Excitation of UV Fluorescence in LaF_3 Doped with Trivalent Cerium and Praseodymium*, Phys. Rev.B, 8, pp. 4989 4995, (1973).

[Ell96] A. Ellens, *Electron-phonon coupling of lanthanide ions in solids*, Ph.D. thesis, Debye Institute, University of Utrecht (1996).

[Ell97a] A. Ellens, H. Andres, A. Meijerink and G. Blasse, *Spectral-line-broadening study of the trivalent lanthanide-ion series. I. Line broadening as a probe of the electron-phonon coupling strength*, Phys. Rev. B55, 173 (1997).

[Ell97b] A. Ellens, H. Andres, A. Meijerink and G. Blasse, *Spectral-line-broadening study of the trivalent lanthanide-ion series. II. The variation of the electron-phonon coupling strength through the series*, Phys. Rev. B55, 180 (1997).

[Erd72] P. Erdös and J. H. Kang, *Electronic Shielding of Pr^{3+} and Tm^{3+} in Crystals*, Phys. Rev. B63393 (1972).

[Far63] E. F. Farrell, J. H. Fang, and R. E. Newnham, Am. Mineral 48, 804 (1963).

[Foe48] Th. Förster, *Zwischenmolekulare Energiewanderung und Fluoreszenz*, Annalen d. Phys. 2, 55 (1948).

[Fre62] A. J. Freeman and R. E. Watson, *Theoretical Investigation of Some Magnetic and Spectroscopic Properties of Rare-Earth Ions*, Phys. Rev. 127, 2058 (1968).

[Gre87] J. E. Greedan, *Rare Earth Elements and Materials*, In Encyclopedia of Physical Science & Technology, Vol.12, editor R. A. Meyers, Academic Press Inc., Orlando, chapter 1, 18-39 (1987).

[Gri61] J.S. Griffith, *The theory of transition metal ions*, Cambridge, UK. (1961).

[Gue83] P. Gürltler, E. Roick, and G. Zimmerer, *SUPERLUMI: A high flux spectroscopic device for luminescence measurements*, Nuclear Instruments and Methods 208,835 (1983).

[Hay80] W. Hayes, M. Yamaga, D. J. Robbins and B. Cockayne, *Optical detection of exciton EPR in $LiYF_4$*, J. Phys. C 13, L1011 (1980).

[Hea76] W. S. Heaps, L. R. Elias, and W. M. Yen, *Vacuum-ultraviolet absorption bands of trivalent lanthanides in LaF_3*, Phys. Rev. B, 13, pp. 94104, (1976).

[Heg81] J. Hegarty, D. L. Huber, and W. M. Yen, *Trapping of optical excitation in Nd-doped PrF_3*, Phys. Rev. B 23, 6271–6279 (1981).

[Heg82] J. Hegarty, D. L. Huber, and W. M. Yen, *Fluorescence quenching by cross relaxation in $LaF_3:Pr^{3+}$*, Phys. Rev. B 25, 5638–5645 (1982).

[Hen89] B. Henderson and G. Imbusch, *Optical Spectroscopy of Inorganic Solids*, Clarendon Press, Oxford (1989).

[Her90] T. Herbert, W. P. Risk, R. M. Macfarlane, and W. Lenth, *Diode-Laser-Pumped 511 nm Upconversion Laser in $YLiF_4:Er^{3+}$,* OSA Proceedings on Advanced Solid-State Lasers, Washington DC, Vol. 6, 379 (1990).

[Hub79] D. L. Huber, *Fluorescence in the presence of traps*, Phys. Rev. B 20, 2307–2314 (1979).

[Hue78] S. Hüfner, *Optical Spectra of Transparent Rare Earth Compounds*, Academic Press (1978).

[Imb67] G. F. Imbusch, *Energy Transfer in Ruby*, Phys. Rev. 153, 326–337 (1967).

[Ino65] M. Inokuti and F. Hirayama, *Influence of energy transfer by the exchange mechanism on donor luminescence*, J. Chem. Phys. 43 (6), 1978 (1965).

[Jay89] C. K. Jayasankar, M. F. Reid, and F. S. Richardson, *Comparative Crystal-Field Analyses of $4f^n$ Energy Levels in $LiYF_4:Ln^{3+}$ Systems*, Phys. Stat. Sol. (b) 155, 559-569, 1989.

[Jia02] Dongdong Jia, R. S. Meltzer, and W. M. Yen, *Location of the ground state of Er^{3+} in doped Y_2O_3 from two-step photoconductivity*, Phys. Rev. B 65, 235116 (2002).

[Jor62] C.K. Jørgensen, *Orbitals in Atoms and Molecules*, Academic Press, New York, (1962).

[Jud62] B. R. Judd, *Optical absorption intensities of rare-earth ions*, Phys. Rev. Vol. 127, 750 (1962).

[Jor71] C. K. Jørgensen, *Modern Aspects of Ligand-Field Theory*, North-Holland, Amsterdam, (1971).

[Kha00] N. M. Khaidukov, M. Kirm, S. K. Lam, D. Lo, V. N. Makhov, G. Zimmerer, *VUV spectroscopy of KYF_4 crystals doped with Nd^{3+}, Er^{3+} and Tm^{3+}*, Optics Communications, Vol. 184, pp. 183-193 (2000).

[Kha02] N. M. Khaidukov, N. Yu. Kirikova, M. Kirm, J. C. Krupa, V. N. Makhov, E. Negodin and G. Zimmerer, *Inter- and intraconfigurational luminescence of LiYF4:Er3+ under selective VUV excitation*, proceedings of SPIE, Vol. 4766, pp. 154-164 (2002).

[Kir96] M. Kirm, I. Martinson, E. Feldbach, R. Kink, A. Lushchik, Ch. Lushchik and A. Maaroos, *Mechanisms of intrinsic and impurity luminescence excitation by synchrotron radiation in wide-gap oxides,* Journal of Electron Spectroscopy and Related Phenomena 79, 91-94 (1996).

[Koe97] S. Körding, *Lumineszenzspektroskopische Untersuchung der Erzeugung und Relaxation elektronischer Ein- und Mehrfachanregungen in Festem Xenon*, Diplomarbeit, Universität Hamburg (1997).

[Kol01] E. van der Kolk, P Dorenbos and C. W. E. van Eijk, *Vacuum ultraviolet excitation of $^1S_0$ and $^3P_0$ emission of Pr^{3+} in $Sr_{0.7}La_{0.3}Al_{11.7}Mg_{0.3}O_{19}$ and SrB_4O_7*, J. Phys.: Condens. Matter 13, 5471-5486, (2001).

[Kru95] J. C. Krupa, *Optical excitations in lanthanide and actinide compounds*, J. of Alloys and Compounds 225, 1-10 (1995).

[Kru97] J. C. Krupa, M. Queffelec, *UV and VUV optical excitations in wide band gap materials doped with rare-earth ions: 4f-5d transitions*, J. of Alloys and Compounds 250, 287-292 (1997).

[Lar00] M. Laroche, J.-L. Doualan, S. Girard, J. Margerie, and R. Morcorge, J. Opt. Soc. Am. B 17(7), 1291 (2000).

[Lac92] P. Lacovara, *Energy Transfer and Upconversion in Yb:Er:YAG*, OSA Proceedings on Advanced Solid-State Lasers, Santa Fe, Vol. 13, 296 (1992).

[Leb00] V. A. Lebedev, , V. F. Pisarenko, N. V. Selina, A. A. Perfilin and M. G. Brik, *Spectroscopic and luminescent properties of Yb,Er:$LaSc_3(BO_3)_4$ crystals*, Optical Materials 14 (2), 121-126 (2000).

[Loh67] E. Loh, *Ultraviolet Absorption Spectra of Ce^{3+} in Alkaline-Earth Fluorides*, Phys. Rev. 154, 270 (1967).

[Loh69] E. Loh, *Ultraviolet absorption spectra of europium and ytterbium in alkaline earth fluorides*, Phys. Rev. 84(2), 184, (1969).

[Lou96] M. Louis, S. Hubert, E. Simoni, J. Y. Gesland, *Energy transfer between lanthanide and actinide ions in $LiYF_4$*, Optical Materials 6, 121-127 (1996).

[Lus96] A. Lushchik, E. Feldbach, R. Kink, Ch. Lushchik, M. Kirm, and I. Martinson, *Secondary excitons in alkali halide crystals*, Phys. Rev. B, 53, 5379-5387 (1996).

[Lut91] W. Luthy, H. P.Weber, *The 3 μm erbium laser*, Infrared Physics, vol.32, 283-90 (1991).

[Lup99] V. Lupei, A. Lupei and G. Boulon, *Dopant distribution and energy transfer processes in crystals*, Spectrochimica Acta Part A, Vol. 55 (4), 783-794 (1999).

[Lup01] V. Lupei, A. Lupei, and S. Georgescu, *The effect of Nd concentration on the spectroscopic and emission decay properties of highly doped Nd:YAG ceramics*, Phys. Rev. B 64, 092102 (2001).

[Lur86] C. Lurin, C. Parent, G. Le Flem and M. Couzi , J. Less-Common Met. 126, 271 (1986).

[Mak00] V. N. Makhov, N. M. Khaidukov, N. Yu. Kirikova, M. Kirm, J. C. Krupa, T. V. Ouvarova, and G. Zimmerer*, VUV emission of rare-earth ions doped into fluoride crystals*, Journal of Luminescence 87-89, 1005-1007, (2000).

[McC98] D. S. McClure, C. Pedrini, *Excitons trapped at impurity centers in highly ionic crystals,* Phys. Rev. B 32, 8465 (1985).

[Mei99] A. Meijerink, R. T. Wegh, *VUV spectroscopy of lanthanides: extending the horizon*, Materials Science Forum, Vol. 315, pp. 11-26 (1999).

[Mel94] C. de Mello Donegá, A. Meijerink and G. Blasse, *Saturation effects in the excitation spectra of rare-earth ions*, Journal of Luminescence 62, 189-201 (1994).

[Mil70] S. A. Miller, H.E.Rast and H.H.Caspers, J. Chem. Phys. 52 (1970) 4172.

[Moo70] H. W. Moos, *Spectroscopic relaxation processes of rare earth ions in crystal,* Journal of Luminescence 1 and 2, 106, (1970).

[Mor75] A. M. Morozov, I. G. Podkolzina, A. M. Tkachuk, V. A. Fedorov, and P. P. Feofilov, *Luminescence and induced emission of the Lithium-erbium and lithium-holmium binary fluorides*, Opt. Spectrosc. (USSR) 39 (3), 338 (1975).

[Mor86] G. P. Morgan, D. L. Huber and W. M. Yen, *The nature of the $^3P_0$ fluorescence quenching processes in $LaF_3:Pr^{3+}$*, Journal of Luminescence 35, 277-287 (1986).

[Nug74] J. L. Nugent, J. Van der Sluis, J. Opt. Soc. Am. 64, 687 (1974).

[OCo84] D. V. O'Conner, D. Phillips, *Time-correlated single photon counting*, Academic Press, London (1984).

[Ofe62] G. S. Ofelt*, Intensities of crystal spectra of rare-earth ions*, J. Chem. Phys., Vol. 37, 511 (1962).

[Oka75] E. Okamoto, M. Sekita, and H. Masui, *Energy transfer between Er3+ ions in LaF3*, Phys. Rev. B, Vol. 11, 5103-5111 (1975).

[Orl94] Yu. V. Orlovskii, R. J. Reeves, and R. C. Powel, *Multiple-phonon nonradiative relaxation*, Phys. Rev. B, Vol 49 (6), 3821 (1994).

[Per83] Yu. E. Perlin, A. M. Tkachuk, and S. I. Klokishner, *Interaction between rare-earth ions in crystals of double fluorides* $LiY_{1-x}RE_xF_4$, Opt. Spectrosc. (USSR) 55 (1), 1 (1983).

[Pet78] M. V. Petrov and A. M. Tkachuk, *Optical spectra and multifrequency stimulated emission of* $LiYF_4$*:Er crystals*, Opt. Spectrosc. (USSR) 45, 147-155 (1978).

[Pie01] L. van Pieterson, *Charge Transfer and* $4f^n \rightarrow 4f^{n-1}5d$ *Luminescence of Lanthanide Ions*, Dissertation , Utrecht University, Holland (2001).

[Pie02] L. van Pieterson, M. F. Reid, G. W. Burdick, A. Meijerink, *transitions of the heavy lanthanides: experiment and theory,* Phys. Rev. B 65, 045114 (2002).

[Pol94] M. Pollnau, Th. Graf, J. E. Balmer, W. Lüthy, and H. P. Weber, *Explanation of the cw operation of the* Er^{3+} *3-μm crystal laser*, Phys. Rev. A 49, 3990–3996 (1994).

[Pol95] M. Pollnau, W. Lüthy, and H. P. Weber, *Population mechanisms of the green* Er^{3+}*:*$LiYF_4$ *laser,* J. Appl. Phys. 77, 6128-6134 (1995).

[Qui89] R. S. Quimby and W. J. Miniscalco, *Continuous-wave lasing on a self-terminating transition*, Appl. Opt. 28, 14 (1989).

[Ray63] D. K. Ray, *Investigation Into the Origin of the Crystalline Electric Field Effects on Rare Earth Ions; II. Conributions from the Rare Earth Orbitals*, Proc. Phys. Soc. 82, 47-57 (1963).

[Raz95] I. Razumova, A. Tkachuk, A. Nikitichev and D. Mironov, *Spectral-luminescent properties of Tm:YLF crystal*, Journal of Alloys and Compounds 225 (1-2), 129-132 (1995).

[Red82] B. R. Reddy and P. Venkateswarlu, J. Chem. Phys. 77, 2862 (1982).

[Ren80] G. M. Renfro, J. C. Windscheif, W. A. Sibley and R. F. Belt, *Optical transitions of Pr3+ and Er3+ ions in LiYF4*, Journal of Luminescence 22, 51-68 (1980).

[Rei00] M. F. Reid, L. van Pieterson, R. T. Wegh, and A. Meijerink, *Spectroscopy and calculations for* $4f^n$*-*$4f^{n-1}$*5d transitions of lanthanide ions in LiYF4*, Phys. Rev. B 62, 14744-14749 (2000).

[Rei02] M. F. Reid, L. van Pieterson, A. Meijerink, *Trends in parameters for the $4f^n$-$4f^{n-1}5d$ spectra of lanthanide ions in crystals*, J. Alloys Compounds 334, 240-245 (2002).

[Ris68] L. A. Riseberg and H. W. Moos, *Multiphonon Orbit-Lattice Relaxation of Excited States of Rare-Earth Ions in Crystals*, Phys. Rev. 174 (2), 429 (1968).

[Rog97] P. Rogin, J. Hullinger, «*Growth of $LiYF_4$ by the Seeded Vertical Gradient Freezing Technique*», J. Cryst. Gr. 172, 200-208, (1997).

[Ron95] C. R. Ronda, *Phosphors for lamps and displays: An applicational view*, Journal of Alloys and Compounds 225, 534-538 (1995).

[Ron97] C. R. Ronda, *Recent achievements in research on phosphors for lamps and displays*, Journal of Luminescence 72-74, 49 (1997).

[Ron98] C.R. Ronda , T. Jüstel, H. Nikol, *Rare earth phosphors: fundamentals and applications*, Journal of Alloys and Compounds 275–277, 669 (1998).

[Ron02] C. R. Ronda, *Luminescent materials with quantum efficiency larger than 1, status and prospects*, Journal of Luminescence 100, 301(2002).

[Run97] M. Runne, *Dynamik angeregter Edelgasatome auf der Oberfläche Edelgasdotierter Edelgasfestkörper*, Dissertation, Universität Hamburg, Hamburg, (1997). (Interner Bericht, DESY HASYLAB 97-04).

[Sen01] A. Sen, S. L. Chaplot, and R. Mittal, *Rigid ion model of lattice dynamics in the laser host fluoroscheelites $LiYF_4$ and $LiYbF_4$*, Phys. Rev. B 64, 024304 (2001).

[Sob79] I. I. Sobelman, *Atomic spectra and Radiative Transition,* Springer-Verlag, Berlin (1979).

[Son93] K. S. Song and R. T. Williams, *Self-Trapped Excitons*, Springer Series in Solid-State Science 105, Springer-Verlag Berlin Heidelberg New York, (1993).

[Ste66] R. M. Sternheimer, *Shielding and Antishielding Effects for Various Ions and Atomic Systems*, Phys. Rev. 146(1), 140-160 (1966).

[Ste00] B. Steeg, *Erzeugung sekundärer Exzitonen in festem Xenon untersucht mit Hilfe der Lumineszenzspektroskopie*, Dissertation, Universität Hamburg (2000).

[Sve93] O. Svelto, *Principles of Lasers*, Plenum Press, New York, 3rd edition (1993).

[Sze81] S. M. Sze, «*Physics of semiconductor device*», Bell Laboratories, Incorporated, A Wiley-Interscience Publication, John Wiley&Sons, (1981).

[Thi01] C. W. Thiel, H. Cruguel, H. Wu, Y. Sun, G. J. Lapeyre, and R. L. Cone, R. W. Equall, R. M. Macfarlane, *Systematics of 4f electron energies relative to host bands by resonant photoemission of rare-earth ions in aluminum garnets*, Phys. Rev. B 64, 085107 (2001).

[Tka85] A. M. Tkachuk, A.V. Poletimova, and M. V. Petrov, *Probabilities of intracenter spontaneous radiative and nonradiative intermultiplet transitions in Er^{3+} ion in the $LiYF_4$ crystal*, Opt. Spectrosc. (USSR) 59 (5), 680 (1985).

[Tka90] A. M. Tkachuk, *Self-quenching and up-conversion processes in $LiYF_4$:RE^{3+} crystals*, Opt. Spectrosc. (USSR) 68 (6), 775 (1990).

[Var61] F. Varsanyi and G. H. Dieke, *Ion-Pair Resonance Mechanism of Energy Transfer in Rare Earth Crystal Fluorescence*, Phys. Rev. Lett. 7, 442–443 (1961).

[Vie03] S. Vielhauer, *Innerschalenanregungen und sekundäre Exzitonen in Edelgasfestkörpern*, Dissertation, Hamburg University (2003).

[Wat72] R. K. Watts* and H. J. Richter, *Diffusion and Transfer of Optical Excitation in YF_3: Yb, Ho*, Phys. Rev. B 6, 1584–1589 (1972).

[Wat75] R. K. Watts, *In Optical Properties of Ions in Solids* (ed. B. Di Bartolo), p. 307, Plenum Press, Ney York (1975).

[Web73] M. J. Weber, *Multiphonon Relaxation of Rare-Earth Ions in Yttrium Orthoaluminate*, Phys. Rev. B,Vol. 8, 54 (1973).

[Weg98] R.T.Wegh, H.Donker and A.Meijerink, *Spin-allowed and spin-forbidden fd emission from Er^{3+} and $LiYF_4$*, Phys. Rev. B 57 R2025 (1998).

[Weg99] R. T. Wegh and A. Meijerink, *Spin-allowed and spin-forbidden $4f^n \rightarrow 4f^{n-1}5d$ transitions for heavy lanthanides in fluoride hosts*, Phys. Rev. B, 60, 10820 (1999).

[Wil83] H. Wilcke, W. Böhmer, R. Haensel, and S. Schwentner, *High Flux and High Resolution VUV Beamline for Luminescence Spectroscopy*, Nuclear Instruments and Methods in Physics Research, 208, 59 (1983).

[Yan76] K. H. Yang and J. A. DeLuca, *VUV fluorescence of Nd^{3+}, Er^{3+}-, and Tm^{3+} doped trifluorides and tunable coherent sources from 1650 to 2600 Å*, Appl. Phys. Lett. 29, 499-501, (1976).

[Yan78] K. H. Yang and J. A. DeLuca, *Vacuum-ultraviolet excitation studies of $5d^1 4f^{n-1}$ to $4f^n$ and $4f^n$ to $4f^n$ transitions of Nd^{3+}-, Er^{3+}-, and Tm^{3+}-doped trifluorides*, Phys. Rev. B 17, 4246, (1978).

[Yen03] M. W. Yen, D. Jia, L. Lu, R. S. Meltzer, *Two-step photoconductivity: determination of impurity levels of Er^{3+} relative to the host bands of Gd_2O_3*, Journal of Luminescence, in press (2003).

[Yok67] M. Yokota and O. Tanimoto, J. Phys. Soc. Japan 22,779 (1967).

Acknowledgements

I am very grateful to all who contribute in the success of this work. Especially, I am grateful to my supervisor, Prof. Dr. Georg Zimmerer for his kind guidance and support during my work. I really appreciate his help in understanding various phenomena of my topic and in correcting carefully all my mistakes. His extraordinary knowledge and authority are the most important impulse for me in performing all further investigations.

Special thanks to Dr. Marco Kirm who provide me with experimental assistance and help in operating SUPERLUMI experimental station. He helped me a lot to understand different physical process. I would like to thank him for the patience in answering to my questions.

Many thanks to the Dr. Sebastian Vielhauer who found always time to help me during my stay at HASYLAB. I am very grateful to him for the sharing his knowledge and experience with me.

I am extremely thankful to Dr. V. Makhov from Lebedev Physical Institute in Moscow for his continuous help in my work.

I would like to thank all members of the SUPERLUMI team for a pleasant and stimulating working atmosphere. Dr. Barbara Steeg, Dr. Elke Sombrowski, Dr. Vambola Kisand, Henning Lichtenberg, Edlira Suljoti and Marcus True are acknowledged.

I would like to thank the whole staff of HASYLAB for their assistance.

Finally I wish to give special thanks to my wife Natalia and our parents for heir continuous support and encouragement.

This work was supported by the Graduiertenkolleg „Spektroskopie an lokalisierten atomaren Systemen - Felder und lokalisierte Atome - Atome und lokalisierte Felder“ and Bundesministerium für Bildung und Forschung (BMBF Project 05 KS1GUD/1).